Kinetic analysis of the collisional layer

Mantas Abazorius
Merton College
University of Oxford

A thesis submitted for the degree of
Doctor of Philosophy in Physics

Trinity 2025

Kinetic analysis of the collisional layer

Mantas Abazorius

Merton College, University of Oxford

Submitted for the degree of Doctor of Philosophy in Physics

Trinity 2025

In magnetic confinement fusion devices, plasma-wall interaction sets the boundary conditions for the plasma. As charged particles follow the field lines, they come in contact with the wall and charge it. For many angles of interest, between the magnetic field and the wall, the wall charges negatively due to electrons being lighter than ions. An absorbing wall sets a boundary condition for the ion distribution function of no ions coming back from the wall. This has a strong effect on the plasma dynamics in the scrape-off layer. Here Braginskii fluid equations are often used to model the plasma. This assumes the distribution function to be approximately a Maxwellian, making it impossible to impose the wall boundary condition of no ions coming back. In this thesis we analyse the collisional layer. This is a layer that connects the Maxwellian plasma far away from the wall to the magnetic presheath – a layer that develops near the wall due to the finite size of ion gyro orbits. To analyse the ion dynamics in the collisional layer, we solve the steady state electrostatic ion drift kinetic equation in one spatial dimension using the full Fokker-Planck collision operator, together with quasineutrality and adiabatic electrons. Absorbing wall boundary condition is used at one end of the spatial domain and, to match with Braginskii's equations, the distribution function for incoming velocities far away from the wall is a Maxwellian. We prove that the kinetic Chodura condition is satisfied at the entrance of the magnetic presheath and that the potential scales as a square root of the distance from the wall near the presheath entrance. We also show that, at the entrance of the collisional layer, the flow of ions has to be supersonic. We have written a semi-Lagrangian finite element code to solve our system of equations numerically. We are able to provide the distribution function at the magnetic presheath entrance and the potential drop across the collisional layer. This can be used to find the distribution function at the wall, which is needed to calculate sputtering yields.

Acknowledgements

This DPhil journey has been a long but exciting one. I met so many great people along the way and I am glad I have an opportunity to thank them here.

First of all, I would like to say thank you to my supervisor Felix Parra. In addition to teaching me all the plasma physics I needed to write this thesis, he provided me with an incredible amount of guidance and encouragement throughout my DPhil, and this is truly appreciated. I would also like to thank my co-supervisor at UKAEA, Fulvio Militello, for his insightful questions and support.

Special thanks to Alex Schekochihin, who was there to teach and inspire from my very first days in Oxford. Thank you to Michael Barnes for providing invaluable feedback at every stage of my DPhil journey.

Thank you to my examiners Michael Barnes and Paolo Ricci for their suggestions, which greatly improved the quality of the thesis.

Throughout my time in the Oxford Plasma Theory group, I met so many friendly and inspiring people. A special thanks to Ollie, Michael H, Nick, and Alessandro, who were there from my first days of DPhil, for their help with physics, great chat and friendliness. Thank you to Juan for all the great coffee and biscuit breaks, a highlight of every afternoon. Also a big thanks to the 2023 EFTC group, who provided more encouragement than I could have imagined during the final stretch of the thesis writing, especially Will, who sacrificed sleep and put up with my unreasonable work hours during this time.

A huge thank you to my physics undergraduate friends Adam, Chris, David, Glenn, Isabelle and Thomas, who showed me how great Oxford can be when you surround yourself with the friendliest and coolest people. I am looking forward to the next *Swan Ball*. Also a big thank you to all the friends I made

in MCBC, for being great company, diversifying my social life and giving me an opportunity to take a break from work.

Thank you to my friends from my school days Arnas, Audrius, Lukas, Mantas, Mantas, Povilas and Vladas. I feel very lucky to have been able to maintain these friendships for such a long time. Thanks also to Johann and Diego for the great lunches and coffee breaks during the last couple years, they really brightened up my days.

I would also like to thank my parents, sister, and grandparents for their love and encouragement throughout my time in Oxford, and for making home such a great place to come back to. Special thanks to Aivaras and Feja for always being there to make me smile (and now Rapolas as well!).

Finally, thank you to Charlotte, who knows just how much effort it took me to get here, and whom I can always rely on for unwavering love and support.

This work has been carried out within the framework of the EUROfusion Consortium, funded by the European Union via the Euratom Research and Training Programme (Grant Agreement No 101052200 — EUROfusion). Views and opinions expressed are however those of the author(s) only and do not necessarily reflect those of the European Union or the European Commission. Neither the European Union nor the European Commission can be held responsible for them.

Contents

List of Figures

Chapter 1

Introduction

Fusion is achieved by colliding fast-moving ions of light elements together in such a way that they fuse into heavier elements, releasing energy in the process. To ensure a high energy yield from fusion collisions, the ions in the plasma have to be hot (high ion temperature T_i), the ion density has to be high (large n_i), and they have to be contained within the system for a long time (large confinement time τ). The product of these three parameters is called the triple product and is a parameter that describes the effectiveness of the fusion process [2, 3]. One of the leading methods of plasma confinement in modern experiments is confinement via magnetic fields. Charged particles follow magnetic field lines. Therefore, externally imposed fields can be used to guide the plasma.

The most common concepts used for magnetic confinement fusion are tokamaks [4], stellarators [5], reversed field pinch devices [6] and magnetic mirrors [7]. Tokamaks, stellarators and reversed field pinches rely on having magnetic field lines inside the machines close in on themselves, ensuring that the plasma stays inside the confined region. However, this perfect confinement breaks down due to collisions, non-uniform geometry of the magnetic field and turbulence. As a result, the particles can move perpendicular to the magnetic field and eventually collide with the container wall in which the plasma is enclosed. Such losses of particles (and the energy they carry) can make the fusion process unsustainable unless reduced to manageable levels. Choosing appropriate magnetic field geometry and plasma parameters can greatly reduce these losses [8].

However, these losses cannot be eliminated completely because we need to extract the energy and the by-products of the fusion reactions. To protect the walls from the flux of hot plasma from the fusion core, we choose to either add protrusions from the wall (limiters) that intersect the field lines, or shape the field lines to intersect the wall in

specific regions (divertors) far from the main plasma. In addition, these regions assist with impurity and Helium ash removal from the device [9]. The locations where the magnetic field intersects the wall experience very high fluxes of heat and particles (up to 20MW/m^2 for ITER [10]). This itself results in the creation of impurities via sputtering [11], which erodes the material as well as contaminates the plasma.

Understanding plasma behaviour in the region near the wall is essential to predict the heat fluxes on the plasma facing components of the device (such as the divertor) and the sputtering yield. In fusion devices we want to minimise the heat flux onto the divertor in order to increase the longevity of the components.

The region between the core, where the field lines are closed, and the wall, called the scrape-off layer (SOL), consists of open magnetic field lines that intersect the wall (Figure 1.1). The plasma density in the SOL ($\sim 10^{19}\text{m}^{-3}$) is ~ 10 times lower than in the core, while the SOL temperature ($\sim 10 - 200\text{eV}$) is more than ~ 100 times smaller [12]. The collisional mean free path in the SOL is often orders of magnitude shorter than the characteristic length scale of the system, making a fluid approximation viable in many machines of interest.

To understand plasma behaviour in the SOL, we need to know the boundary conditions for the plasma and the electromagnetic fields at the wall. These are determined by the magnetised plasma-wall interaction, which is what we study in this work. In the next sections of this chapter, we describe the most common models used to model the SOL plasma, and the boundary layers that develop when the plasma comes into contact with the wall. We focus on the collisional layer and the equations that govern the plasma behaviour in this region.

1.1 Edge modelling

The plasma in the SOL is quasineutral and magnetised. Drift kinetic [13] or gyrokinetic [14–16] approximations can be used to describe the system – this approach is used for numerical simulations by a variety of codes [17–21]. However, drift kinetic or gyrokinetic simulations can be costly as they require resolving dynamics in a five dimensional phase space (three position coordinates and two velocity coordinates, since the drift kinetic and gyrokinetic equations are gyroaveraged). One way to reduce the computational cost is

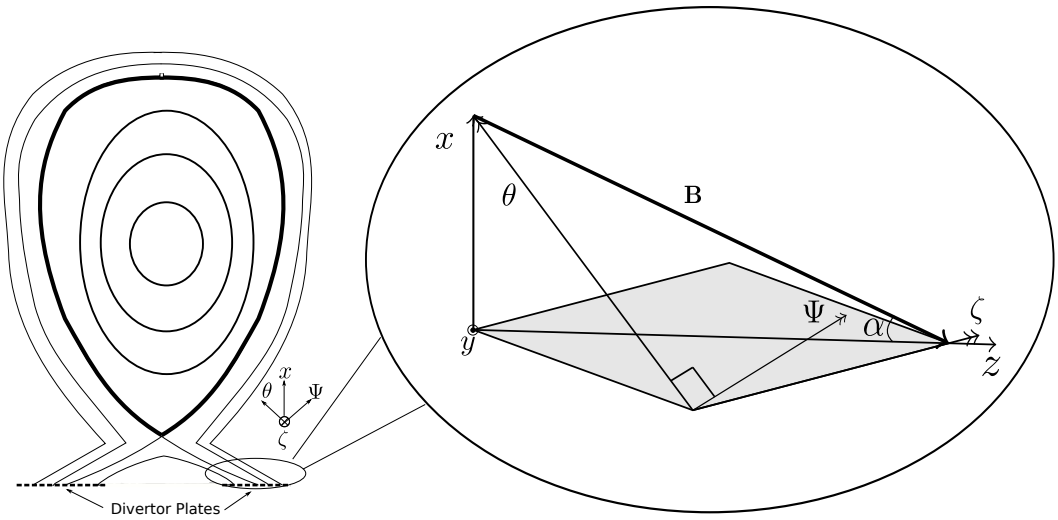

Figure 1.1: The poloidal plane of a fusion device, with black lines representing the flux surfaces. The SOL is the layer of plasma outside the last closed flux surface (represented by the thick line). Zoomed in, we show a simplified geometry of the the plasma-divertor boundary as seen from the side. In the sketches, θ is the poloidal direction, ζ is the toroidal direction and Ψ is the radial direction. Very close to the wall, the magnetic field $\boldsymbol{B}$ is approximately uniform and mostly toroidal. In our analysis we will use x, which is the direction normal to the divertor plate (divertor plate is in grey in the right figure). The magnetic field can be decomposed into x and horizontal direction z. It makes a small angle α with the divertor. The y axis is perpendicular to x and z.

to use the fact that the SOL is relatively cold and dense, and hence use a Braginskii fluid model [22] to describe the plasma behaviour. Codes based on Braginskii's fluid equations (or extensions of them) are used extensively in edge modelling [23–26] and predate the gyrokinetic codes. For the fluid approximation to be valid, the plasma must satisfy $\lambda_{MFP} \ll L_\parallel$, where $L_\parallel \sim 50$m [27] is the connection length, an average distance between a point in the SOL and the wall along the field line, and $\lambda_{MFP} \sim 5$m [12] is the ion-ion collisional mean free path. Note that the Braginskii model assumes that Coulomb ion-ion collisions dominate over the ion-neutral collisions, even though these two types of collisions are equally frequent in the edge [28]. We ignore this limitation in this thesis for simplicity.

SOL fluid codes use drift-reduced Braginskii fluid equations [29] to simulate the plasma. In these codes the perpendicular length scales are typically assumed to be much shorter than the parallel length scales, but still larger than the ion Larmor radius $1/\rho_i \gg |\nabla_\perp| \gg |\nabla_\parallel|$, where $\nabla_\parallel \equiv \hat{\mathbf{b}} \cdot \nabla$ and $\nabla_\perp \equiv \nabla - \hat{\mathbf{b}}\nabla_\parallel$. The ion Larmor radius is $\rho_i = m_i v_{ti}/(ZeB)$, where B is the magnetic field strength, m_i is the ion mass,

Ze is the ion charge, e is the proton charge and the ion thermal speed is $v_{ti} = \sqrt{2T_i/m_i}$. Here T_i is the ion temperature. The system of equations the fluid codes solve are evolution equations for the ion density n (equal to electron density due to quasineutrality), vorticity $\boldsymbol{\omega}$, ion and electron mean flows along the magnetic field lines $u_{i\parallel}$ and $u_{e\parallel}$, and ion and electron temperatures T_i and T_e. An example of such equations (the ones used in GBS [30]), which are representative of equations used by most of the SOL fluid codes, are given in Appendix A. The equations require boundary conditions for the plasma parameters across and along the field boundaries. This will be discussed in more detail in Section 1.4.

The fluid assumption breaks down near the core, as the plasma in the core is hot and collisionless, and near the wall, where a boundary layer of width proportional to λ_{MFP} is established. The plasma-wall interaction determines the boundary conditions for the fluid equations and thus affects their solutions. When compared against the experimental data from the TCV tokamak [31], it was found that fluid codes with different numerical implementations and different sets of boundary conditions [23, 24, 26] tend to match the results far away from the target, but worse agreement was found near the divertor plates, which could be a result of not setting the correct boundary conditions at the plasma-wall boundary. This shows that the boundary condition problem is not solved and is worth investigating.

In addition to setting boundary conditions, the boundary layers near the wall determine the ion distribution function at the wall, which is needed for sputtering and other materials calculations. We describe these boundary layers in the next section.

1.2 Boundary layers

In order to minimise the flux onto the wall, the magnetic field lines intersect the wall at a small angle α with the surface of the device. This increases the divertor area over which the power is distributed. In most cases of interest, the electrons reach the wall faster than the ions, charging the wall negatively. The negatively charged wall assumption is valid as long as α is not too small. Electrons travel along the magnetic field lines much faster than the ions since $v_{te}/v_{ti} \sim \sqrt{T_e m_i/T_i m_e} \gg 1$, where $v_{tr} = \sqrt{2T_r/m_r}$ is the thermal speed of species $r = i, e$. For $T_i \sim T_e$ the ion Larmor radius is much larger than the

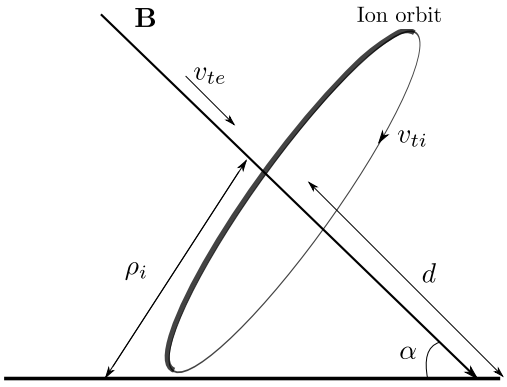

Figure 1.2: In order for the wall to be negatively charged, the time taken for electrons to reach the wall has to be much shorter than the time taken for ions, that is, $d/v_{te} \ll \rho_i \cos\alpha / v_{ti}$. Here d is the distance along the magnetic field line that the electron travels to move a distance of order $\rho_i \cos\alpha$ in the x direction, $\tan\alpha \sim \rho_i/d$. The inequality $d/v_{te} \ll \rho_i/v_{ti}$ implies that $\sin\alpha \gg \sqrt{m_e/m_i}$.

electron Larmor radius ρ_e, $\rho_i/\rho_e = \sqrt{T_i m_i / T_e m_e} \gg 1$. If the angle α is sufficiently small, the ions may reach the wall faster than the electrons because they can collide with the wall while their orbit centre is at a distance $\sim \rho_i \cos\alpha$ from the wall. To have an electron repelling wall, we require that the electrons hit the wall before the ions do. This implies that the time for an ion at a distance ρ_i from the wall to reach the wall should be shorter than the ion gyrofrequency, giving $\sin\alpha \gg \sqrt{m_e/m_i}$ (Figure 1.2). The critical angle at which the wall becomes positively charged is an area of active research. References [32] and [1] showed that the condition for a negatively charged wall could be even weaker than $\sin\alpha \gtrsim \sqrt{m_e/m_i}$, as the wall is negatively charged for angles as low as $\sin\alpha \sim m_e/m_i$ for $\rho_e/\lambda_D \ll 1$. Here $\lambda_D = \sqrt{\epsilon_0 T_e / e^2 n_e}$ is the Debye length, n_e is the electron number density, e is the proton charge, and ϵ_0 is the permittivity of free space. For $\rho_e/\lambda_D \sim 1$, the wall can only charge positively for $\sin\alpha \lesssim \sqrt{m_e \rho_e / m_i \lambda_D}$ [1]. In this thesis we assume that the angle α is large enough that the wall is negatively charged.

As a result of the wall charge, boundary layers develop near the wall. Each layer is associated with approximations, which are valid in most of the SOL, breaking down. These are the assumptions of high collisionality, circular gyro-orbits and quasineutrality. These assumptions fail due to characteristic length scales changing as the wall is approached. We proceed to describe each of these layers in more detail.

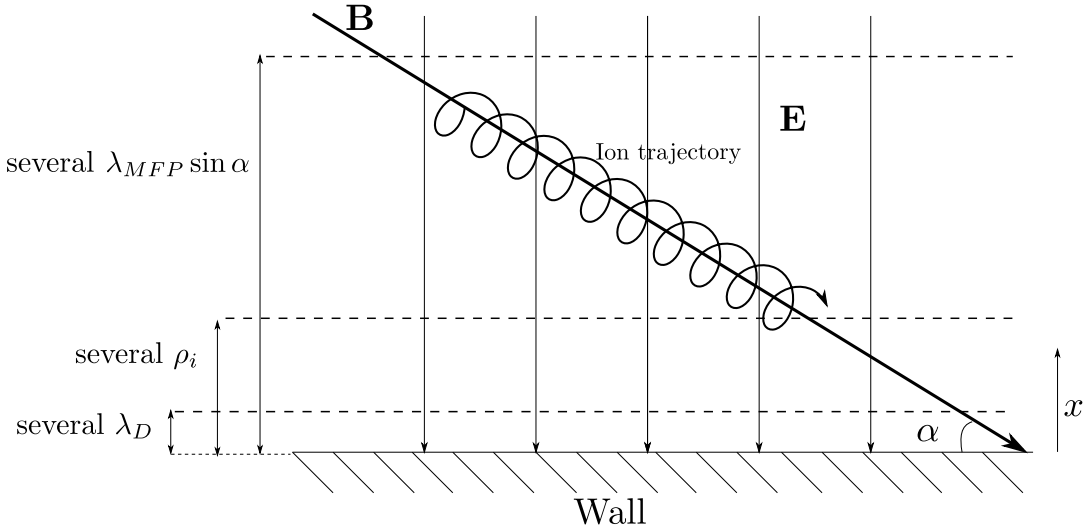

Figure 1.3: The boundary layers of a collisional magnetised plasma near a solid wall (the divertor) in the limit when all the layers can be clearly distinguished. The magnetic field **B** makes an angle α with the wall. The electric field **E** points in the x direction. The spiral indicates the ion trajectory in the collisional layer. As ions enter the magnetic presheath, the electric field becomes large enough to strongly distort their circular orbits.

At the plasma-wall boundary, in the direction perpendicular to the wall (x direction from here on), there are five length scales of interest (Figure 1.3). These are the Debye length $\lambda_D \sim 0.02$mm, the electron gyroradius $\rho_e \sim 0.02$mm, the ion gyroradius $\rho_i \sim 0.7$mm, the ion-ion collisional mean free path projection in the direction normal to the wall $\lambda_{MFP} \sin\alpha \simeq \alpha\lambda_{MFP} \sim 0.5$m (where $\alpha \sim 0.1$), and the device size in the poloidal direction $L \sim 5$m. The estimates of these length scales in a fusion device given above are obtained from [12]. In this work, we do not consider any neutral effects for simplicity, even though in fusion devices the mean free path for charge exchange collisions can often be smaller than the λ_{MFP}. We leave the inclusion of neutrals for future work. Assuming that the plasma near the divertor satisfies the scale separation $\rho_e \sim \lambda_D \ll \rho_i \ll \sin\alpha\lambda_{MFP} \ll L$ (this is a good approximation near many divertor targets [33, 34]), we can split the plasma-wall boundary into three separate layers.

Firstly, as a result of the negatively charged wall, a small positively charged plasma layer called the Debye sheath, with a thickness of a few λ_D, develops near the wall [35, 36]. The electric field in this layer is strong enough to partially shield the rest of the plasma from the negatively charged wall. Due to the scale separation, the ion trajectories in the Debye sheath are not affected by the magnetic field or collisions, and they are accelerated to the wall by the strong electric field. Electron dynamics depend on the size of ρ_e/λ_D.

When $\rho_e/\lambda_D \sim 1$ the electron gyro-orbit must be taken into account. Importantly, the ions arriving into the sheath from the plasma bulk (or other layers that cover the Debye sheath) must satisfy a collective condition for the sheath to exist: the Bohm condition [36] requires that at the Debye sheath entrance (DSE) there be no ions moving away from the wall ($f_{i,DSE}(v_x \geq 0) = 0$), and that the distribution function of incoming ions satisfy

$$\int_{v_x<0} d^3\mathbf{v} \frac{f_{i,DSE}}{v_x^2} \leq \frac{m_i}{Z^2 T_e} n_{e,DSE}, \tag{1.1}$$

where v_x is the velocity perpendicular to the wall (see Figure 1.1), with $v_x < 0$ corresponding to particles moving towards the wall. At the entrance of the Debye sheath, there cannot be many ions with slow velocities ($|v_x| \ll \sqrt{ZT_e/m_i}$) towards the wall to ensure that the integral in (1.1) is finite. The equation can be derived by considering plasma dynamics in the sheath, specifically, by requiring the potential to be monotonic in the sheath and the plasma to be quasineutral at the Debye sheath entrance. Another intuitive way of arriving to the kinetic Bohm is to consider conservation of momentum in the Debye sheath. The total electron and ion momentum flux towards the wall must increase as the plasma approaches the wall since the wall is negatively charged and the Debye sheath has a positive charge. As electrons approach the wall, their density and, due to adiabatic response, their momentum flux towards the wall decrease. Therefore, the ion momentum flux towards the wall must increase faster than the electron momentum flux decreases, requiring very few slow ions to exist. In Appendix B we show that this leads to the Bohm condition (1.1).

Before reaching the Debye sheath, the ions go through a magnetic presheath with a width of a few ρ_i. This layer develops whenever the angle $\alpha \neq 90°$. Here the plasma is quasineutral and collisionless since $\lambda_D \ll \rho_i \ll \lambda_{MFP} \sin\alpha$. The electric field in the magnetic presheath is strong enough to distort the usually circular ion gyro-orbits, which no longer follow the magnetic field lines. At the magnetic presheath entrance (MPE), the ions have to satisfy the kinetic Chodura condition [33, 37–39], that is, no ions move away from the wall and the distribution of ions moving towards the wall must satisfy the integral condition

$$\int_{v_\parallel>0} d^3\mathbf{v} \frac{f_{i,MPE}}{v_\parallel^2} \leq \frac{m_i}{Z^2 T_e} n_{e,MPE}, \tag{1.2}$$

where $v_\parallel$ is the component of velocity parallel to the magnetic field and we assume without loss of generality that $\mathbf{B}$ points towards the wall. The Chodura condition differs from the Bohm condition (1.1) by requiring that there be no ions moving away from the wall in the direction parallel to the field, and that there be very few slow ions moving towards the wall in the direction parallel to the field. The electric field in the magnetic presheath accelerates ions towards the wall so that by the time they reach the Debye sheath the Bohm condition (1.1) is satisfied. The kinetic Chodura condition can be derived by considering plasma in the magnetic presheath and requiring the quasineutrality to be satisfied, and for the potential to be monotonic. This is done in [33] for small α and assuming no gradients parallel to the wall. It is shown in full generality in [37]. An argument similar to the one proposed for the Bohm condition in Appendix B should be possible to derive the kinetic Chodura condition using the formalism introduced in [33]. However, we have not yet been able to prove it.

Fluid codes often assume that the fluid approximations break down at the MPE and this is where the boundary conditions for the fluid equations need to be set. However, one of the boundary conditions imposed by the magnetic presheath, the kinetic Chodura condition (1.2), cannot be satisfied by a Maxwellian distribution function, which will always have a finite value of $f_i(v_\parallel = 0)$. We argue that another layer, a collisional layer of characteristic size $\lambda_{MFP} \sin\alpha$, connects the magnetic presheath and the rest of the SOL, and should be included in the analysis. The collisional layer, which is the focus of this thesis, and the equations valid in this region are described in the following section. We will return to the discussion of its effect on the fluid codes in Section 1.4.

1.3 The collisional layer

The magnetic presheath and the Debye sheath have been analysed and the plasma dynamics in these regions are well understood [27, 33, 38, 40]. In this work, we focus on the collisional layer. Collisional presheaths based on charge exchange collisions with cold neutrals [41] or ionisation [42], loosely related to the collisional layer, have been studied analytically. In the collisional presheaths, a source of ions produces an ion flow towards the wall. The Braginskii fluid equations are derived in the limit where ion-ion collisions dominate over the neutral collisions and thus we need to focus on this regime to determine

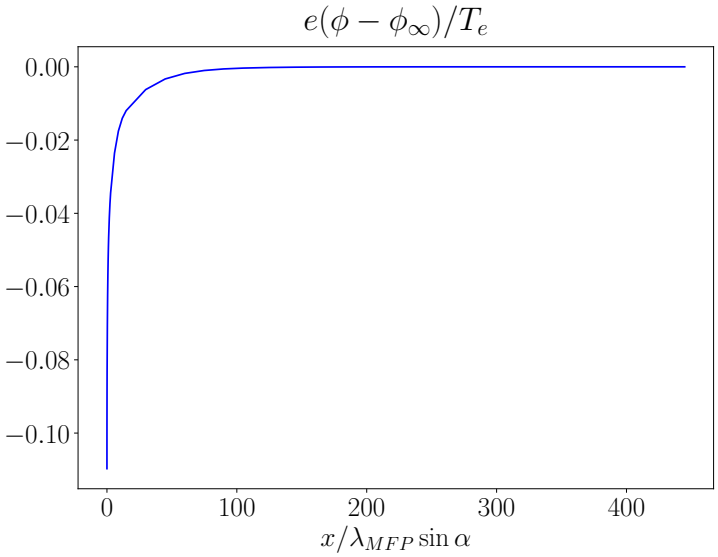

Figure 1.4: Shape of the electric potential ϕ in the collisional layer as a function of $x/\lambda_{MFP}\sin\alpha$ for $ZT_e/T_{i\infty} = 1.0$ and $u_{i\parallel\infty}/v_{ti\infty} = 1.49$, where ϕ_∞ is the electrostatic potential at the boundary $x/\lambda_{MFP}\sin\alpha \to \infty$, and $T_{i\infty}$, $v_{ti\infty}$ and $u_{i\parallel\infty}$ are the ion temperature, thermal speed and mean flow at the entrance to the collisional layer, respectively.

how the Braginskii fluid equations and the magnetic presheath connect. In this work we obtain the ion flux towards the wall from a boundary condition at one of the ends of our domain, representing a source of incoming plasma, and no source of ions within the region itself and no neutral collisions. The collisionality cannot be assumed to be large (which it is further away from the wall) or small (which it is in the magnetic presheath). As a result, a full Fokker-Planck collision operator for ion-ion collisions must be included in the analysis. To the best of our knowledge this problem has not been investigated before.

The collisional layer thickness is of order $\lambda_{MFP}\sin\alpha$. Since $\lambda_D \ll \rho_i \ll \lambda_{MFP}\sin\alpha \ll L$, we use the separation of scales to set the entrance to the magnetic presheath at $x/\lambda_{MFP}\sin\alpha \simeq 0$ and the entrance to the collisional layer at $x/\lambda_{MFP}\sin\alpha \to \infty$. The potential is determined by quasineutrality, which holds because $\lambda_D \ll \lambda_{MFP}\sin\alpha$. The quasineutrality equation is

$$n_e = Zn_i = Z\int d^3\mathbf{v} f_i, \tag{1.3}$$

where n_e and n_i are the electron and ion densities, respectively, f_i is the ion distribution function. The electric field is electrostatic, $\mathbf{E} = -\nabla\phi$, with ϕ the electrostatic potential. We assume ϕ varies in the x direction mostly (Figure 1.4). This assumption will be discussed in Section 1.3.1.

As discussed in the introduction, in this work we analyse the case of an electron repelling wall. For a negatively charged wall, the electrons are repelled by the wall and therefore most of them are not absorbed. In this work, we neglect any absorbed electrons and assume that they follow a Boltzmann response, namely

$$n_e(x) = n_{e\infty} \exp\left(\frac{e(\phi(x) - \phi_\infty)}{T_e}\right), \tag{1.4}$$

where ϕ_∞ and $n_{e\infty}$ are the electrostatic potential and electron density far away from the wall (at the boundary $x \to \infty$). In a more realistic model, the most energetic electrons would make it through the potential barrier and be absorbed by the wall, breaking the adiabatic electron assumption. Taking this into account would require a kinetic treatment of electrons in addition to solving the magnetic presheath and the Debye sheath dynamics simultaneously [1].

1.3.1 Ion drift kinetic equation

We can use the drift kinetic approximation [13] to describe the ion motion. Using the drift kinetic approximation is justified because the collisional layer length scale is much larger than the ion gyroradius ($\rho_i \ll \lambda_{MFP} \sin\alpha$). This implies that $v_{ti}/\Omega_i \ll v_{ti}/\nu_i \sin\alpha$, and thus $\nu_i \ll \Omega_i \sin\alpha \lesssim \Omega_i$, where ν_i is the ion-ion collision frequency and Ω_i is the ion gyrofrequency. We order the characteristic frequency of the system as $d/dt \sim \nu_i \ll \Omega_i$. We let the electrostatic potential be of order $\phi \sim T_e/e$. We do not need to consider the gyrokinetic approximation because we do not expect any plasma dynamics to evolve on a length scale ρ_i.

In the drift kinetic approximation, to lowest order in $\rho_i/\lambda_{MFP} \sin\alpha \ll 1$, the distribution function does not depend on the direction of the particle velocity perpendicular to the magnetic field, characterised by an angle φ called the gyrophase. In magnetic field aligned coordinates, the velocity vector is

$$\mathbf{v} = v_\parallel \hat{\mathbf{b}} + v_\perp \hat{\mathbf{v}}_\perp, \tag{1.5}$$

where $\hat{\mathbf{v}}_\perp = \cos\varphi\ \hat{\mathbf{e}}_1 + \sin\varphi\ \hat{\mathbf{e}}_2$. Here $\hat{\mathbf{b}}$ is the unit vector in the magnetic field direction. In our Cartesian space coordinates (Figure 1.3), it is $\hat{\mathbf{b}} = \cos\alpha\hat{\mathbf{z}} - \sin\alpha\hat{\mathbf{x}}$. The magnitude of velocity perpendicular to the field line is $v_\perp = \sqrt{\mathbf{v}\cdot\mathbf{v} - v_\parallel^2}$. The unit vectors $\hat{\mathbf{e}}_1$ and $\hat{\mathbf{e}}_2$ span the plane in velocity space perpendicular to $\hat{\mathbf{b}}$, such that $\hat{\mathbf{e}}_1 \times \hat{\mathbf{e}}_2 = \hat{\mathbf{b}}$ and $\hat{\mathbf{e}}_1 \cdot \hat{\mathbf{e}}_2 = 0$.

In our model, the only collisions that affect the ion distribution function f_i are ion-ion collisions, as the ion-electron collisions are of higher order in mass ratio than other terms in the equation. We also do not take any neutral dynamics into account in this thesis, even though, as mentioned earlier, we know that they can be important in this region. This is done to match to the Braginskii equations, which do not treat neutrals, at $x \to \infty$. The drift kinetic equation for the ion distribution function $f_i(\mathbf{r}, v_\parallel, v_\perp)$ with a Fokker-Planck collision operator $C_{ii}[f_i, f_i]$ for the ion-ion collisions is

$$\frac{\partial f_i}{\partial t} + (v_\parallel \hat{\mathbf{b}} + \mathbf{v}_E) \cdot \nabla f_i - \frac{Ze}{m_i} \nabla\phi \cdot \hat{\mathbf{b}} \frac{\partial f_i}{\partial v_\parallel} = C_{ii}[f_i, f_i], \tag{1.6}$$

where $\mathbf{v}_E = \mathbf{E} \times \mathbf{B}/B^2$ is the $\mathbf{E} \times \mathbf{B}$ drift and $\mathbf{r}$ is the position vector.

The length scales in the collisional layer determine the size of the derivatives in this region, that is, $\nabla_j \sim 1/L_j$ with $j = x, y, z$. In the collisional layer the length scales are

$$L_x \sim \lambda_{MFP} \sin\alpha, \quad L_y \sim L_\perp \tag{1.7}$$

where L_x and L_y indicate the length scales in the x and y directions (shown in Figure 1.1), respectively. Here $L_\perp$ is the length scale perpendicular to the magnetic field line in the SOL, outside the collisional layer. The $L_\perp$ length scale can be associated with the SOL width λ_{SOL}, which is of size $\lambda_{SOL} \sim 1$cm [27, 43].

To find the length scale L_z associated with the z direction, we consider a field line that intersects the wall at an angle α as shown in Figure 1.1. Then, the perpendicular and parallel derivatives are

$$\nabla_\parallel \equiv \hat{\mathbf{b}} \cdot \nabla = -\sin\alpha \frac{\partial}{\partial x} + \cos\alpha \frac{\partial}{\partial z}, \tag{1.8}$$

$$\nabla_\perp = (\hat{\mathbf{x}} \cos\alpha + \hat{\mathbf{z}} \sin\alpha)(\cos\alpha \frac{\partial}{\partial x} + \sin\alpha \frac{\partial}{\partial z}) + \hat{\mathbf{y}} \frac{\partial}{\partial y}. \tag{1.9}$$

We can also express the gradient along z as

$$\frac{\partial}{\partial z} = \sin\alpha(\hat{\mathbf{x}} \cos\alpha + \hat{\mathbf{z}} \sin\alpha) \cdot \nabla_\perp + \cos\alpha \nabla_\parallel. \tag{1.10}$$

Thus the length scale L_z depends on the size of the angle α.

$$L_z \sim L_\perp / \sin\alpha \quad \text{if} \quad \tan\alpha \gg L_\perp / L_\parallel, \tag{1.11}$$

$$L_z \sim L_\parallel / \cos\alpha \quad \text{if} \quad \tan\alpha \ll L_\perp / L_\parallel. \tag{1.12}$$

Here $L_\parallel$ is the length scale along the magnetic field line in the SOL, given by connection length and is of size $L_\parallel \sim 50$m [27].

The electric field term in the drift kinetic equation (1.6) can be expanded as

$$\nabla\phi \cdot \hat{\mathbf{b}} \frac{\partial f_i}{\partial v_\parallel} = -\frac{\partial \phi}{\partial x} \sin\alpha \frac{\partial f_i}{\partial v_\parallel} + \frac{\partial \phi}{\partial z} \cos\alpha \frac{\partial f_i}{\partial v_\parallel}. \tag{1.13}$$

The gradients perpendicular to the wall dominate as long as $L_x \ll L_z \tan\alpha$. Using (1.7) and (1.11), we find that the condition $L_x \ll L_z \tan\alpha$ requires gives $\sin\alpha\cos\alpha \ll L_\perp/\lambda_{MFP}$ for $\tan\alpha \gg L_\perp/L_\parallel$. This condition is not always satisfied in fusion devices, but it is the simplest case one can consider for large angle $\tan\alpha \gg L_\perp/L_\parallel$. For $\tan\alpha \ll L_\perp/L_\parallel$, we use scalings (1.7) and (1.12) to find $\lambda_{MFP}/L_\parallel \ll 1/\cos\alpha$. This condition must always be satisfied for the fluid description to hold outside the collisional layer. From here on, we neglect the derivative with respect to x in equation (1.13).

The drift term $\mathbf{v}_E$ in the x direction can be neglected as long as

$$v_\parallel \sin\alpha \gg \frac{\phi}{L_y B}\cos\alpha \sim \frac{\rho_i}{L_\perp} v_\parallel \cos\alpha, \tag{1.14}$$

where for the second scaling we used (1.7) and $\phi \sim T_e/e$. This is true as long as $\rho_i/\lambda_{SOL} \ll \tan\alpha$, if we take $L_\perp \sim \lambda_{SOL}$. For the data discussed earlier ($\rho_i \sim 0.7$mm, $\alpha \sim 0.1$, $\lambda_{SOL} \sim 1$cm) this condition is not clearly satisfied, and the electric field parallel to the wall can have an effect on the ion motion in the layer. However, for the analysis done in this thesis, we assume that

$$\rho_i/\lambda_{SOL} \ll \tan\alpha \tag{1.15}$$

holds and the study of the regime $\tan\alpha \sim \rho_i/\lambda_{SOL}$ is left for future work. We thus find that

$$(v_\parallel \hat{\mathbf{b}} + \mathbf{v}_E) \cdot \hat{\mathbf{x}} \frac{\partial f_i}{\partial x} \sim \frac{v_\parallel}{\lambda_{MFP}} f_i, \tag{1.16}$$

$$(v_\parallel \hat{\mathbf{b}} + \mathbf{v}_E) \cdot \hat{\mathbf{y}} \frac{\partial f_i}{\partial y} \sim \frac{\rho_i}{\lambda_{SOL}\tan\alpha} \frac{v_\parallel}{\lambda_{MFP}} f_i \ll \frac{v_\parallel}{\lambda_{MFP}} f_i, \tag{1.17}$$

$$(v_\parallel \hat{\mathbf{b}} + \mathbf{v}_E) \cdot \hat{\mathbf{z}} \frac{\partial f_i}{\partial z} \sim \frac{v_\parallel}{L_\parallel} f_i \sim \frac{\lambda_{MFP}}{L_\parallel} \frac{v_\parallel}{\lambda_{MFP}} f_i \ll \frac{v_\parallel}{\lambda_{MFP}} f_i. \tag{1.18}$$

Keeping only the lowest order terms, the drift kinetic equation (1.6) simplifies to

$$\frac{\partial f_i}{\partial t} - v_\parallel \sin\alpha \frac{\partial f_i}{\partial x} + \frac{Ze}{m_i} \sin\alpha \frac{\partial \phi}{\partial x} \frac{\partial f_i}{\partial v_\parallel} = C_{ii}[f_i, f_i]. \tag{1.19}$$

The Fokker-Planck collision operator $C_{ii}[f_i, f_i]$ can be written in the form

$$C_{ii}[f_i, f_i] = \frac{\gamma_{ii}}{m_i^2} \nabla_v \cdot \mathbf{\Gamma}_{ii}, \tag{1.20}$$

where $\gamma_{ii} = 2\pi Z^4 e^4 \ln \Lambda_{ii}/(4\pi\epsilon_0)^2$, $\ln \Lambda_{ii}$ is the Coulomb logarithm, ϵ_0 is the vacuum permittivity and

$$\mathbf{\Gamma}_{ii} = \int d^3\mathbf{v}' f_i(\mathbf{v}) f_i(\mathbf{v}') \nabla_g \nabla_g g \cdot \left[\nabla_v \ln f_i(\mathbf{v}) - \nabla_{v'} \ln f_i(\mathbf{v}')\right]. \tag{1.21}$$

Here $\mathbf{g}$ is the velocity difference vector defined as $\mathbf{g} = \mathbf{v} - \mathbf{v}'$. In cylindrical coordinates, it can be written as $\mathbf{g} = \mathbf{v}_\perp - \mathbf{v}'_\perp + (v_\parallel - v'_\parallel)\hat{\mathbf{b}}$. The tensor $\nabla_g \nabla_g g$ is

$$\nabla_g \nabla_g g = \frac{\mathbf{I} g^2 - \mathbf{g}\mathbf{g}}{g^3}, \tag{1.22}$$

where $\mathbf{I}$ is the unit matrix. Since the ion distribution function f_i is gyrophase independent, the required derivatives are

$$\nabla_v \ln f_i(\mathbf{v}) = \frac{\partial \ln f_i}{\partial v_\parallel}\hat{\mathbf{b}} + \frac{\partial \ln f_i}{\partial v_\perp}\hat{\mathbf{v}}_\perp, \qquad \nabla_{v'} \ln f_i(\mathbf{v}') = \frac{\partial \ln f'_i}{\partial v'_\parallel}\hat{\mathbf{b}} + \frac{\partial \ln f'_i}{\partial v'_\perp}\hat{\mathbf{v}}'_\perp. \tag{1.23}$$

Above and in the rest of the chapter, we denote $f_i(\mathbf{v}')$ by f'_i.

In Appendix C we show that, for the gyrophase-independent ion distribution function,

$$\begin{aligned}
\mathbf{\Gamma}_{ii} = \int dv'_\perp dv'_\parallel v'_\perp f_i f'_i \frac{2}{((v_\parallel - v'_\parallel)^2 + (v_\perp + v'_\perp)^2)^{1/2}} \frac{1}{v_\perp v'_\perp} \\
\times \left\{ \left[X_{\parallel\parallel}\left(\frac{\partial \ln f_i}{\partial v_\parallel} - \frac{\partial \ln f'_i}{\partial v'_\parallel}\right) + X_{\parallel\perp}\frac{\partial \ln f_i}{\partial v_\perp} + X_{\parallel\perp'}\frac{\partial \ln f'_i}{\partial v'_\perp} \right] \hat{\mathbf{b}} \right. \\
\left. + \left[X_{\perp\parallel}\left(\frac{\partial \ln f_i}{\partial v_\parallel} - \frac{\partial \ln f'_i}{\partial v'_\parallel}\right) + X_{\perp\perp}\frac{\partial \ln f_i}{\partial v_\perp} + X_{\perp\perp'}\frac{\partial \ln f'_i}{\partial v'_\perp} \right] \hat{\mathbf{v}}_\perp \right\},
\end{aligned} \tag{1.24}$$

where the coefficients are

$$\begin{aligned}
X_{\parallel\parallel} &= 2v_\perp v'_\perp \left(\frac{-(v_\parallel - v'_\parallel)^2}{(v_\parallel - v'_\parallel)^2 + (v'_\perp - v_\perp)^2} E + K \right), \\
X_{\parallel\perp} &= X_{\perp\parallel} = v'_\perp (v_\parallel - v'_\parallel) \left(\frac{(v_\parallel - v'_\parallel)^2 - v_\perp^2 + v'^2_\perp}{(v_\parallel - v'_\parallel)^2 + (v'_\perp - v_\perp)^2} E - K \right), \\
X_{\parallel\perp'} &= v_\perp (v_\parallel - v'_\parallel) \left(\frac{(v_\parallel - v'_\parallel)^2 + v_\perp^2 - v'^2_\perp}{(v_\parallel - v'_\parallel)^2 + (v'_\perp - v_\perp)^2} E - K \right), \\
X_{\perp\perp} &= \frac{v'_\perp}{v_\perp}((v_\parallel - v'_\parallel)^2 + v_\perp^2 + v'^2_\perp)(K - E) + 2v'_\perp \left(v_\perp \frac{(v_\parallel - v'_\parallel)^2}{(v_\parallel - v'_\parallel)^2 + (v'_\perp - v_\perp)^2} - v'_\perp \right) E, \\
X_{\perp\perp'} &= \left(2v_\perp v'_\perp \frac{(v_\perp - v'_\perp)^2}{(v_\parallel - v'_\parallel)^2 + (v'_\perp - v_\perp)^2} + v_\perp^2 + v'^2_\perp \right) E - (v_\perp^2 + v'^2_\perp) K.
\end{aligned} \tag{1.25}$$

Here K and E are complete elliptic integrals of the first and second kind, defined as

$$K(m) = \int_0^{\pi/2} d\gamma \frac{1}{\sqrt{1 - m\sin^2\gamma}}, \qquad E(m) = \int_0^{\pi/2} d\gamma \sqrt{1 - m\sin^2\gamma}. \tag{1.26}$$

In equation (1.25), the arguments of the elliptic integrals are suppressed to make the equations easier to read. In full, they are

$$\begin{aligned} K &= K\left(\frac{4v_\perp v'_\perp}{(v_\parallel - v'_\parallel)^2 + (v_\perp + v'_\perp)^2}\right), \\ E &= E\left(\frac{4v_\perp v'_\perp}{(v_\parallel - v'_\parallel)^2 + (v_\perp + v'_\perp)^2}\right). \end{aligned} \tag{1.27}$$

We will use equations (1.3), (1.4) and (1.19), with boundary conditions explained below, to find steady state solutions for f_i and ϕ in the collisional layer. To simplify notation, in some places we will use the fact that the left hand side of the equation is a full time derivative of the distribution function

$$\frac{\mathrm{d}f_i}{\mathrm{d}t} = \frac{\partial f_i}{\partial t} - v_\parallel \sin\alpha \frac{\partial f_i}{\partial x} + \frac{Ze}{m_i}\sin\alpha \frac{\partial \phi}{\partial x}\frac{\partial f_i}{\partial v_\parallel}. \tag{1.28}$$

1.3.2 Boundary conditions for the collisional layer

The boundaries of our system are at the MPE, $x = 0$, and at the collisional layer entrance (CLE), $x \to \infty$. In the SOL, at distances much larger than $\lambda_{MFP}\sin\alpha$ away from the wall, the plasma is highly collisional, and so, as mentioned before, fluid models are used. The high collisionality assumption breaks down near the core-SOL boundary. In our model the collisional layer is far away from this region and its boundary is the part of the SOL where Braginskii fluid description is valid. In the fluid approximation, the distribution function is, to lowest order, a Maxwellian. At the MPE ions exit the collisional layer and enter the collisionless magnetic presheath, they can no longer escape from colliding with the wall, and so no ions return. To sum up, for our system we have

$$f_i(x \to \infty, v_\parallel > 0, v_\perp, t) \simeq n_{i\infty}\left(\frac{m_i}{2\pi T_{i\infty}}\right)^{3/2} \exp\left\{-\frac{m_i(v_\parallel - u_{i\parallel\infty})^2 + m_i v_\perp^2}{2T_{i\infty}}\right\}, \tag{1.29}$$

$$f_i(x = 0, v_\parallel \le 0, v_\perp, t) = 0, \tag{1.30}$$

where $u_{i\parallel\infty}$ and $T_{i\infty}$ are the ion parallel mean flow and the ion temperature at $x \to \infty$. The parallel mean flow and the temperature at any point in space are given by $u_{i\parallel} = \int d^3\mathbf{v}\, v_\parallel f_i/n_i$ and $T_i = \int d^3\mathbf{v}\, m_i((v_\parallel - u_{i\parallel})^2 + v_\perp^2)f_i/3n_i$.

The boundary condition at $x = 0$ determines the parallel flow at the boundary $x \to \infty$. Indeed, in steady state, integrating equation (1.19) over velocity gives

$$\frac{\partial}{\partial x} \int d^3\mathbf{v}\, v_\parallel f_i = 0. \tag{1.31}$$

Thus $n_i u_{i\parallel}$ is constant along x. Since there is a net flux of ions hitting the wall, equation (1.31) above implies that whatever the distribution function at the CLE is, it must have a mean velocity along the magnetic field lines towards the wall, that is, $u_{i\parallel} = u_{i\parallel\infty} n_{i\infty}/n_i > 0$. It has to be noted that although many ions will reach the MPE and be absorbed by the wall, some of them will not travel that far and be reflected back due to collisions. This will affect the distribution function at the collisional layer entrance. Therefore, to determine the $v_\parallel < 0$ part of the ion distribution function at the CLE, we need to first understand the plasma behaviour in the layer.

One of the main results of this thesis (Chapter 2) is a proof that $u_{i\parallel\infty} > c_s$ at the entrance to the collisional layer, where the speed of sound in the plasma is given by

$$c_s = \sqrt{\frac{ZT_e + 5T_{i\infty}/3}{m_i}}. \tag{1.32}$$

This condition has to be satisfied by the incoming plasma, and it, or conditions similar to it, are already used in the fluid codes, where it is described as a Bohm or Chodura condition. Even though this condition might seem the same as previous versions of the Chodura or Bohm condition, the plasma behaviour in the collisional layer is very different from the plasma behaviour in the magnetic presheath or the Debye sheath. To the best of our knowledge, this is the first time the condition has been derived for the collisional layer boundary. Note that in our model, $x \to \infty$ and CLE are equivalent locations. We will use CLE for the rest of this chapter to make the separations of various regions clear, but will move to using subscript ∞ in all the other chapters, where we are only looking at the collisional layer.

The only physical boundary condition at the MPE is (1.30). That is, the kinetic Chodura condition (1.2) is not imposed, but must be a property of the solution in the collisional layer. Chapter 3 contains the other main result of the thesis: we show that the dynamics in the collisional layer, specifically the Fokker-Planck collisions, force the kinetic Chodura condition to be satisfied at $x = 0$ (at the MPE). However, this turns

out to be a challenging task numerically, requiring high resolutions in both position and velocity space (see Section 5.4).

This thesis develops a framework for determining the ion distribution function at the wall given an incoming Maxwellian distribution. We solve the collisional layer and find the ion distribution function at the MPE. This is then used as a boundary condition for a magnetic presheath solver `GYRAZE` [1], which can find the ion distribution at the wall (see Section 5.3). This would allow one to calculate quantities such as sputtering yields.

1.4 Boundary conditions for a fluid model

We now discuss the region of the SOL where fluid approximation is appropriate and how the collisional layer could be used to give boundary conditions for the fluid equations, which are often used to model the plasma edge.

In the continuity equation, there are terms like $\nabla_\parallel n$ and $\nabla_\parallel u_{e\parallel}$, which require one boundary condition along the magnetic field line, and terms like $\nabla_\perp^2 n$, the numerical diffusion term, which need two boundary conditions perpendicular to the field line. In principle, since the surfaces perpendicular to the magnetic field intersect the wall (see Figure 1.5), the boundary conditions for $\nabla_\perp^2 n$ need to be obtained from the boundary layers on the wall. To avoid this and to simplify the description of boundary conditions, we will use a trick developed in [17], which exploits the fact that $L_\perp \ll L_\parallel$ and allows us not to consider the wall boundary conditions for the $\nabla_\perp$ terms.

When magnetic field lines intersect the wall purely in the x direction, that is, intersect the wall at $\alpha = 90°$, the perpendicular derivative is given by $\nabla_\perp = \hat{\mathbf{y}}\partial/\partial y + \hat{\mathbf{z}}\partial/\partial z$, and a boundary condition in x (the wall) is not required to invert the $\nabla_\perp^2$ operator. This property can be extended to $\alpha \neq 90°$ as long as the angle α is not too small – this is the approach used in [17]. To see why it works, consider a two dimensional example in $x - z$ plane given in Figure 1.5. From (1.9) and (1.8), it follows that the magnitude of the perpendicular gradient is

$$\nabla_\perp = (\hat{\mathbf{x}}\cos\alpha + \hat{\mathbf{z}}\sin\alpha)(\frac{1}{\sin\alpha}\frac{\partial}{\partial z} - \frac{1}{\tan\alpha}\nabla_\parallel). \tag{1.33}$$

The length scale for the z direction is $L_z \sim \min(L_\parallel/\cos\alpha, L_\perp/\sin\alpha)$ (see Figure 1.5 or equation (1.10)). For large angles, such that the condition (1.11) is satisfied, the parallel

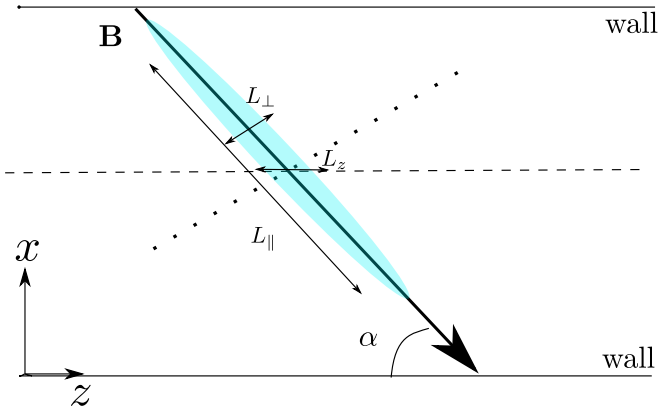

Figure 1.5: A sketch of the magnetic field line intersecting the wall at angle α. If the angle α is 90°, the perpendicular and horizontal planes overlap and the boundary conditions from the walls are not needed for differential operators perpendicular to the magnetic field. If the field line is not normal to the wall, the gradients in the perpendicular plane (dotted line) can be approximated as a gradient in the horizontal plane (dashed line) as long as $\tan\alpha \gg L_\perp/L_\parallel$. The blue structure gives the characteristic size of plasma quantities in the parallel and perpendicular directions. In the drift-reduced models $L_\perp \ll L_\parallel$. The characteristic length scale in z direction depends on $L_\perp$ at small angles but cannot exceed $L_\parallel/\cos\alpha$, that is, $L_z \sim \min(L_\parallel/\cos\alpha, L_\perp/\sin\alpha)$.

gradient can be neglected since $\partial/\partial z \gg \nabla_\parallel \cos\alpha$ giving

$$\nabla_\perp = (\hat{\mathbf{x}}\cos\alpha + \hat{\mathbf{z}}\sin\alpha)\frac{1}{\sin\alpha}\frac{\partial}{\partial z}. \tag{1.34}$$

Thus the boundary conditions at the wall are not required to invert $\nabla_\perp$. However, for $\tan\alpha \lesssim L_\perp/L_\parallel \ll 1$, both terms on the right side in (1.33) are of the same order and parallel derivatives, which require boundary condition at the wall, must be kept. In the following discussion, we assume that the angle is such that (1.11), and thus (1.34), hold. Therefore, in the fluid equations used for edge modelling , we only need to provide wall-boundary conditions for the terms that have the $\nabla_\parallel$ operator.

To obtain the wall-boundary condition, we have to solve the collisional layer. Since the wall is electron repelling, and the electron mean flow towards the wall is $u_{e\parallel} \sim u_{i\parallel} \sim c_s \ll v_{te}$, most of the electrons are confined in the SOL and only a small fraction of the most energetic electrons reach the wall. As a result adiabatic electron response is a valid approximation for the electron density. However, it misses the effect of the wall on electron flow. Fully solving the collisional layer with kinetic electrons in conjunction with the magnetic presheath and the sheath determines electron mean flow $u_{e\parallel CLE}$ at the CLE, given the following quantities: ion temperature $T_{i,CLE}$, electron temperature $T_{e,CLE}$, the

ion mean flow $u_{i\|CLE}$, and the potential drop between the CLE and the wall $\Delta\phi_{Tot}$. Here $\Delta\phi_{Tot}$ is the total potential drop across the collisional layer, magnetic presheath and the Debye sheath. In normalised variables, by solving the collisional layer, we would find a function F that gives

$$u_{e\|CLE}/c_s = F(e\Delta\phi_{Tot}/T_{e,CLE}, u_{i\|CLE}/c_s, T_{e,CLE}/T_{i,CLE}). \tag{1.35}$$

The collisional layer with kinetic electrons, coupled with the magnetic presheath and the Debye sheath solutions, would also allow us to find the exact electron distribution function at CLE, which could be used to find an exact value of electron heat flux without the use of transmission coefficients.

To see how the solution to collisional layer (1.35) could be used to close the system of equations we consider a simpler fluid model than the one used by most of the edge modelling codes (which are described by the drift-reduced Braginskii equations given in Appendix A). We obtain the simplified model by keeping only the lowest order terms in $\lambda_{MFP}/L_\| \sim \sqrt{m_e/m_i} \ll 1$ and $\rho_i/L_\perp \ll 1$. The fluid equations are then

$$\frac{\partial n}{\partial t} = -\frac{1}{B}[\phi, n] + \frac{2}{eB}\left[C(p_e) - enC(\phi)\right] - \nabla_\|(nu_{e\|}) + D_n\nabla_\perp^2 n + s_n, \tag{1.36}$$

$$\frac{\partial u_{i\|}}{\partial t} = -\frac{1}{B}[\phi, u_{i\|}] - u_{i\|}\nabla_\| u_{i\|} - \frac{1}{m_i n}\nabla_\|(p_e + p_i) + D_{u_{i\|}}\nabla_\perp^2 u_{i\|}, \tag{1.37}$$

$$\begin{aligned}\frac{\partial T_e}{\partial t} = &-\frac{1}{B}[\phi, T_e] - u_{e\|}\nabla_\| T_e + \frac{2}{3}T_e\left[\frac{0.71\nabla_\| j_\|}{en} - \nabla_\| u_{e\|}\right] \\ &+ \frac{4}{3}\frac{T_e}{eB}\left[\frac{7}{2}C(T_e) + \frac{T_e}{n}C(n) - eC(\phi)\right] + \nabla_\|(\chi_{\|e}\nabla_\| T_e) + D_{T_e}\nabla_\perp^2 T_e \\ &+ s_{T_e} - \frac{4}{3}\frac{m_e}{m_i}\frac{1}{\tau_e}(T_e - T_i),\end{aligned} \tag{1.38}$$

$$\begin{aligned}\frac{\partial T_i}{\partial t} = &-\frac{1}{B}[\phi, T_i] - u_{i\|}\nabla_\| T_i + \frac{4}{3}\frac{T_i}{eB}\left[C(T_e) + \frac{T_e}{n}C(n) - eC(\phi)\right] \\ &- \frac{10}{3}\frac{T_i}{eB}C(T_i) + \frac{2}{3}T_i\left[(u_{i\|} - u_{e\|})\frac{\nabla_\| n}{n} - \nabla_\| u_{e\|}\right] \\ &+ D_{T_i}\nabla_\perp^2 T_i + s_{T_i} + \frac{4}{3}\frac{m_e}{m_i}\frac{1}{\tau_e}(T_e - T_i).\end{aligned} \tag{1.39}$$

The vorticity equation simplifies to the lowest order current conservation equation

$$B\nabla_\|\left(\frac{en(u_{i\|} - u_{e\|})}{B}\right) + \nabla\cdot\left(\frac{\mathbf{B}\times\nabla(p_i + p_e)}{B^2}\right) = 0 \tag{1.40}$$

and the electron parallel momentum equation gives

$$0 = -\nabla_\| p_e + en\nabla_\|\phi - 0.71n\nabla_\| T_e. \tag{1.41}$$

Here $p_r = n_r T_r$ is pressure of species r, and $r = i, e$ stands for ions and electrons, $j_\parallel = en(u_{i\parallel} - u_{e\parallel})$ is the parallel current, $D_\Omega, D_{u_{i\parallel}}, D_{T_e}$ and D_{T_i} are numerical diffusion terms, s_n and s_T are source terms, τ_r are the collisional times and $\chi_{\parallel e}$ is the electron thermal conductivity. The Poisson bracket is defined as

$$[\phi, f] = \hat{\mathbf{b}} \cdot (\nabla\phi \times \nabla f), \tag{1.42}$$

and the curvature operator is

$$C(f) = \frac{B}{2}\left(\nabla \times \frac{\hat{\mathbf{b}}}{B}\right) \cdot \nabla f. \tag{1.43}$$

The collisional layer model provides boundary conditions for the $\nabla_\parallel u_{e\parallel}$, $\nabla_\parallel j_\parallel$, and $\nabla_\parallel(\chi_{\parallel e}\nabla_\parallel T_e)$ terms. We proceed to explain how equations (1.36)–(1.41) could be coupled to the collisional layer solver.

In a tokamak SOL, any given magnetic field line intersects the walls at two locations, A and B. The CLE is located at a distance of a few $\lambda_{MFP}\sin\alpha$ away from the wall – we label these points CLE_A and CLE_B. The potential difference between the walls $\Delta\phi_{AB}$ can be fixed to any value and provides a boundary condition for the system. Given the values of $n, u_{i\parallel}, u_{e\parallel}, T_i, T_e$ and ϕ at a previous time step, we use equations (1.36)–(1.39) to find the values of $n, u_{i\parallel}, T_i$ and T_e at the new time step. Since the outgoing flow $u_{i\parallel CLE} > c_s$ is supersonic, sound waves cannot travel from the CLE into the domain and we do not need n or T_i at the CLE. The parallel electron heat flux at the CLE is necessary for the electron energy equation (1.38), and this is one quantity that can be calculated with a kinetic electron treatment. This leaves $u_{e\parallel}$ and ϕ at the new time step as unknowns. Equation (1.40) can then be used to find the gradient of $u_{e\parallel}$ along the magnetic field line, and equation (1.41) to find the same gradient for ϕ. If we had the values of $u_{e\parallel}$ and ϕ at CLE_A, we could integrate along the field lines using the expressions of their gradients and thus find the values of $u_{e\parallel}$ and ϕ everywhere in the simulation region up to CLE_B. Thus we need two more equations to find the solution. This is found by using the relationship (1.35) at CLE_A and CLE_B to close the equations.

This work does not aim to give a solution to the problem of connecting the fluid layer with the magnetic presheath as it does not include essential kinetic electron physics. In addition, we neglect any gradients parallel to the wall (in z and y directions), as discussed in Section 1.3.1. As a result we cannot provide boundary conditions for parallel viscosity

G_i, the scalar vorticity Ω or vector vorticity $\boldsymbol{\omega}$, which are needed to solve the full fluid equations (such as those given in Appendix A). These boundary conditions require us to keep terms that are higher order in $\lambda_{MFP}/L_\parallel$ and $\rho_i/L_\perp$ and hence depend on gradients parallel to the wall. The thesis describes the solution of the simpler problem, and can be considered the first step towards the full solution.

1.5 Main results

In Chapter 2, we analyse the behaviour of the distribution function at the CLE, $x \to \infty$, and find one of the main results of this thesis, a constraint on the mean flow $u_{i\parallel CLE}$ of the Maxwellian at the CLE, $u_{i\parallel CLE}$ must be larger than the adiabatic sound speed in the plasma. In Chapter 3, we focus on the region near the MPE and show that for an ion-electron plasma with ion-ion Fokker-Planck collisions, the electric field diverges and the distribution function near the MPE is exponentially small at small velocities. As a result, we recover the kinetic Chodura condition, which we know must be satisfied for the magnetic presheath to exist [33]. We also show that the potential near the MPE scales as $\sim x^{1/2}$ in the collisional layer. Chapter 4 introduces the numerical scheme used to solve the system of equations that describes the plasma dynamics in the collisional layer. These are quasineutrality (1.3) with adiabatic electron response (1.4) and the steady state case of the drift kinetic equation (1.19). We use Galerkin's method with quadratic finite elements in velocity space, ensuring that the collision operator conserves particle number, momentum and energy. To model the steady state flow of the plasma across the layer, we use a semi-Lagrangian approach, following the characteristics of the particles. In Chapter 5, we present the numerical results of the simulations and find the potential drop across the layer. We also show the results of coupling our code to the magnetic presheath and Debye sheath solver [1] and provide the ion distribution function at the wall for different $T_{e,CLE}/T_{i,CLE}$ and $u_{i\parallel CLE}/c_s$. We also discuss the difficulties in capturing the Chodura condition numerically. In Chapter 6, we summarise the results of the thesis and consider how the model could be extended to include kinetic electron and neutral interactions.

Chapter 2

Distribution function far away from the wall

This chapter contains one of the main results of the thesis. We show that the mean flow of the ion distribution function far away from the wall has to be larger than the collisional adiabatic sound speed and directed towards the wall. In Section 2.1, we introduce the linearised system of equations, which are valid in the region far away from the wall. In Section 2.2, we perform a subsidiary expansion for solutions at large x with characteristic decay length scales much longer than $\lambda_{MFP} \sin\alpha$. Solutions with long decay lengths scales occur when the mean flow of the incoming Maxwellian, $u_{\parallel\infty}$, is approximately equal to c_s, the speed of sound in the plasma. We show that the mean flow has to be larger than the sound speed and find a relationship between the length scale, the mean flow and the electron-ion temperature ratio. In Section 2.3 we compare the derived scalings with simulation results. We demonstrate the constraint $u_{\parallel\infty} > c_s$ by showing that simulations with lower mean flows give results that depend on the size of the simulation box and have a large electric field far away from the wall. The analytically derived scaling of the length scale with $u_{\parallel\infty}$ is not satisfied and requires further work.

2.1 Perturbation far away from the wall

We want to solve equations (1.3), (1.4) and (1.19) in steady state for the ion distribution function f far away from the wall. The system of equations is

$$-v_\parallel \sin\alpha \frac{\partial f}{\partial x} + \frac{Ze}{m} \sin\alpha \frac{\partial \phi}{\partial x} \frac{\partial f}{\partial v_\parallel} = C[f, f], \tag{2.1}$$

$$n_{e\infty} \exp(e\phi/T_e) = Zn, \tag{2.2}$$

where we choose the potential at infinity to be zero. Above and from here on we drop the i subscript in f_i, m_i, n_i for convenience; that is, all the quantities without a subscript refer to the ions, while electron quantities will have a subscript e.

At $x \to \infty$ the distribution function is a Maxwellian with some mean flow towards the wall. Therefore, at large x, we can choose the distribution function and the potential to be

$$f = f_M(\mathbf{v}) + K(x, \mathbf{v}), \qquad \phi = \Theta(x), \tag{2.3}$$

where

$$f_M(v_\perp, v_\parallel) = \frac{n_\infty}{(\pi v_{t\infty}^2)^{3/2}} \exp\left(-\frac{(v_\parallel - u_{\parallel\infty})^2}{v_{t\infty}^2} - \frac{v_\perp^2}{v_{t\infty}^2} \right) \tag{2.4}$$

and $v_{t\infty} = \sqrt{2T_\infty/m}$, where T_∞ is the ion temperature at the boundary at $x \to \infty$. We have also introduced

$$K(x, \mathbf{v}) \ll f_M(\mathbf{v}) \quad \text{and} \quad \Theta(x) \ll T_e/e, \tag{2.5}$$

small perturbations of the distribution function and the potential, respectively.

Substituting (2.3) into (2.1) and (2.2), we find

$$-v_\parallel \frac{\partial K}{\partial x} + \frac{Ze}{m} \sin\alpha \frac{\partial \Theta}{\partial x} \frac{\partial f_M}{\partial v_\parallel} = C^{(l)}[K], \tag{2.6}$$

$$n_\infty \frac{e\Theta}{T_e} = \int d^3\mathbf{v} K, \tag{2.7}$$

where $C^{(l)}[K] = C[K, f_M] + C[f_M, K]$ is the linearised collision operator. We choose to look for a separable solution

$$K(x, \mathbf{v}) = S(x)H(\mathbf{v}), \qquad \Theta(x) = \Phi S(x). \tag{2.8}$$

Plugging this expression into (2.6) and using (2.7), we get

$$\frac{\partial S}{\partial x} \sin\alpha \left[-v_\parallel H + \frac{Ze}{m_i} \frac{\partial f_M}{\partial v_\parallel} \Phi \right] = C^{(l)}[H]S. \tag{2.9}$$

With this ansatz we get eigenvalue equations

$$\frac{\partial S}{\partial x} \sin\alpha = -\frac{1}{\lambda} S, \tag{2.10}$$

and the eigenvalue-like equations

$$\frac{v_\parallel}{\lambda}H - \frac{Ze}{m_i}\frac{\partial f_M}{\partial v_\parallel}\frac{\Phi}{\lambda} = C^{(l)}[H], \tag{2.11}$$

$$n_\infty \frac{e\Phi}{T_e} = \int d^3\mathbf{v}H, \tag{2.12}$$

where λ is a constant. From this we see that

$$S(x) = \exp\left(-\frac{x}{\lambda \sin\alpha}\right), \tag{2.13}$$

where we choose to set $S(0) = 1$ and any amplitude is absorbed into H.

The eigenvalue-like equations (2.11) and (2.12) are not standard as the linearised collision operator is singular. Therefore we cannot know if the simple ansatz (2.8), and thus the exponentially decaying solutions, are the only solutions for $x \to \infty$. We will be able to show that there is at least one solution of this type. We proceed to analyse the exponentially decaying solutions, with characteristic wavelength λ. The eigenvalue-like equations (2.11) and (2.12) could be solved numerically by expanding H in the Sonine-Legendre basis. Instead, we consider an analytic limit by performing an expansion of equations (2.11) and (2.12) that we explain in the next section. The expansion will allow us to obtain an approximate relationship between λ and $u_{\parallel\infty}$, which is valid when $u_{\parallel\infty}$ is close to the speed of sound.

2.2 Subsidiary expansion in ϵ and Δ_s

We look for perturbations with decay lengths $\lambda \gg \lambda_{MFP}\sin\alpha$, where $\lambda_{MFP} = v_{t\infty}/\nu_c$ is the mean free path of ions due to self collisions. The collision frequency ν_c is the one defined by Braginskii [22]. In terms of γ_{ii}, it is given by

$$\nu_c = \frac{2^{5/2}\gamma_{ii}n_\infty}{3\sqrt{\pi}m^2 v_{t\infty}^3}. \tag{2.14}$$

We perform a subsidiary expansion in $\epsilon = \lambda_{MFP}/\lambda \ll 1$. The expansion of the perturbations H and Φ in $\epsilon \ll 1$ is

$$H = H_0 + \epsilon H_1 + \epsilon^2 H_2 + ..., \tag{2.15}$$

$$\Phi = \Phi_0 + \epsilon\Phi_1 + \epsilon^2\Phi_2 + ... \tag{2.16}$$

Here $H_0 \sim H_1 \sim H_2$ and $\Phi_0 \sim \Phi_1 \sim \Phi_2$.

We will see that the expansion in $\epsilon \ll 1$ is only valid if $u_{\parallel\infty}$ is slightly supersonic. Therefore, we introduce another small parameter $\Delta_s = (u_{\parallel\infty} - c_s)/c_s \ll 1$, where $c_s = \sqrt{5T_\infty/3m + ZT_e/m}$ is the adiabatic speed of sound at infinity. We choose the small parameters to be of similar order, $\Delta_s \sim \epsilon$. Then, our Maxwellian, to first order in Δ_s, is $f_M = f_{Ms} + 2\Delta_s f_{Ms}(v_\parallel - c_s)c_s/v_{t\infty}^2$, where

$$f_{Ms} = \frac{n_\infty}{(\pi v_{t\infty}^2)^{3/2}} \exp\Big(- \frac{(v_\parallel - c_s)^2 + v_\perp^2}{v_{t\infty}^2}\Big). \tag{2.17}$$

To first order in Δ_s and ϵ, we get that the right hand side of equation (2.11) is

$$\begin{aligned} C^{(l)}[H] &\simeq C^{(l)}[H_0 + \epsilon H_1] \\ &\simeq C_s^{(l)}[H_0] + \epsilon C_s^{(l)}[H_1] + \Delta_s C\left[H_0, \frac{2w_\parallel c_s}{v_{t\infty}^2} f_{Ms}\right] + \Delta_s C\left[\frac{2w_\parallel c_s}{v_{t\infty}^2} f_{Ms}, H_0\right], \end{aligned} \tag{2.18}$$

where we have defined the parallel component $w_\parallel = \mathbf{w}\cdot\hat{\mathbf{b}}$ of the peculiar velocity $\mathbf{w} = \mathbf{v} - c_s\hat{\mathbf{b}}$ and $C_s^{(l)} = C[H, f_{Ms}] + C[f_{Ms}, H]$ is the collision operator linearised with respect to f_{Ms}. The left hand side of equation (2.11) is, to second order in Δ_s and ϵ,

$$\begin{aligned} \frac{v_\parallel}{\lambda} H - \frac{Ze}{m\lambda}\Phi\frac{\partial f_M}{\partial v_\parallel} \simeq& \epsilon\frac{w_\parallel}{\lambda_{MFP}} H_0 + \epsilon\frac{c_s}{\lambda_{MFP}} H_0 - \epsilon\frac{Ze}{m\lambda_{MFP}}\Phi_0\frac{\partial f_{Ms}}{\partial w_\parallel} \\ &+ \epsilon^2\frac{w_\parallel}{\lambda_{MFP}} H_1 + \epsilon^2\frac{c_s}{\lambda_{MFP}} H_1 \\ &- \epsilon^2\frac{Ze}{m\lambda_{MFP}}\Phi_1\frac{\partial f_{Ms}}{\partial w_\parallel} - \epsilon\Delta_s\frac{2c_s}{v_{t\infty}^2}\frac{Ze}{m\lambda_{MFP}}\Phi_0\frac{\partial(f_{Ms}w_\parallel)}{\partial w_\parallel}. \end{aligned} \tag{2.19}$$

We now proceed to solve these equations order by order.

2.2.1 Zeroth order

Using expansions (2.18) and (2.19), to lowest order, the equation (2.11) is

$$C_s^{(l)}[H_0] = 0. \tag{2.20}$$

The solution to this equation is a perturbation to the Maxwellian f_{Ms}

$$H_0 = \left[\frac{n_0}{n_\infty} + \frac{mw_\parallel}{T_\infty}u_0 + \frac{T_0}{T_\infty}\left(\frac{w_\parallel^2 + w_\perp^2}{v_{t\infty}^2} - \frac{3}{2}\right)\right] f_{Ms}, \tag{2.21}$$

where n_0, u_0 and T_0 are the lowest order perturbations in density, mean flow and temperature respectively. Quasineutrality equation (2.12) then gives

$$\Phi_0 = \frac{T_e}{e}\frac{n_0}{n_\infty}. \tag{2.22}$$

We can find a relationship between n_0, u_0 and T_0 by going to next order.

2.2.2 First order

To first order in Δ_s and ϵ, equation (2.11) is

$$C_s^{(l)}[H_1] + \frac{\Delta_s}{\epsilon} C\left[H_0, \frac{2w_\parallel c_s}{v_{t\infty}^2} f_{Ms}\right] + \frac{\Delta_s}{\epsilon} C\left[\frac{2w_\parallel c_s}{v_{t\infty}^2} f_{Ms}, H_0\right] = \frac{w_\parallel}{\lambda_{MFP}} H_0 + \frac{c_s}{\lambda_{MFP}} H_0 - \frac{Ze}{m\lambda_{MFP}} \Phi_0 \frac{\partial f_{Ms}}{\partial w_\parallel}. \quad (2.23)$$

We multiply this equation by $1, w_\parallel$ and w^2 and integrate over velocity to get a linear system of equations for n_0, u_0 and T_0,

$$\begin{pmatrix} 1 & 1 & 0 \\ \frac{1+ZT_e/T_\infty}{5/3+ZT_e/T_\infty} & 1 & \frac{1}{5/3+ZT_e/T_\infty} \\ 3/2 & 5/2 & 3/2 \end{pmatrix} \begin{pmatrix} n_0/n_\infty \\ u_0/c_s \\ T_0/T_\infty \end{pmatrix} = \begin{pmatrix} 0 \\ 0 \\ 0 \end{pmatrix}. \quad (2.24)$$

Here we used the fact that the $1, w_\parallel, w^2$ moments of the collision operators are zero. If the mean flow speed $u_{\parallel\infty}$ were not equal to $\pm c_s$ to lowest order, the matrix would not be singular and the only solution would be $H_0 = 0$. This is the reason why we had to choose $u_{\parallel\infty} \simeq \pm c_s$. We have chosen the positive sign, $u_{\parallel\infty} \simeq +c_s$, because, as argued earlier in Section 1.3.2, the fact that the flux of ions is positive at the wall means that $u_{\parallel\infty}$ is positive.

Matrix equation (2.24) gives us a relationship between the lowest order perturbations

$$\frac{n_0}{n_\infty} = -\frac{u_0}{c_s} = \frac{3T_0}{2T_\infty}. \quad (2.25)$$

Using this with equation (2.21) we get

$$H_0 = \left(\frac{w_\parallel^2 + w_\perp^2}{v_{t\infty}^2} - 3\frac{w_\parallel c_s}{v_{t\infty}^2}\right) \frac{T_0}{T_\infty} f_{Ms}. \quad (2.26)$$

We can now solve for H_1 using equation (2.23). Due to linearity of the linearised collision operator, we can define H_{1A} and H_{1B} such that

$$C_s^{(l)}[H_{1A}] = \frac{w_\parallel}{\lambda_{MFP}} H_0 + \frac{c_s}{\lambda_{MFP}} H_0 - \frac{Ze}{m\lambda_{MFP}} \Phi_0 \frac{\partial f_{Ms}}{\partial w_\parallel}, \quad (2.27)$$

$$C_s^{(l)}[H_{1B}] + \frac{\Delta_s}{\epsilon} C\left[H_0, \frac{2w_\parallel c_s}{v_{t\infty}^2} f_{Ms}\right] + \frac{\Delta_s}{\epsilon} C\left[\frac{2w_\parallel c_s}{v_{t\infty}^2} f_{Ms}, H_0\right] = 0. \quad (2.28)$$

Then $H_1 = H_{1A} + H_{1B}$. We choose H_{1A} to be such that its $1, w_\parallel, w^2$ moments are zero, so that all the first order perturbations in density, mean flow and temperature are in H_{1B}.

To solve for H_{1A} we use the technique pioneered by Braginskii [22]. We change variables from the regular cylindrical coordinates $(w_\perp, w_\parallel, \varphi)$ to (x, ξ, φ), where $x = w^2/v_{t\infty}^2$ and $\xi = w_\parallel/w$, and express H_{1A} in terms of Sonine-Legendre polynomials

$$H_{1A} = \sum_{k,q} a_{q,k} x^{k/2} L_q^{(k+1/2)}(x) P_k(\xi) f_{Ms}. \tag{2.29}$$

The sum runs from $k, q = 0$ to infinity for all integer values of k, q. To make the calculation useful, we will truncate this sum at some finite number.

The Sonine polynomials satisfy the orthogonality relation

$$\int_0^\infty dx x^{j+1/2} L_p^{(j+1/2)}(x) L_q^{(j+1/2)}(x) e^{-x} = \frac{\Gamma[p+j+3/2]}{p!}\delta_{pq}, \tag{2.30}$$

and the Legendre polynomials satisfy

$$\int_{-1}^{1} d\xi P_j(\xi) P_m(\xi) = \frac{2}{2m+1}\delta_{mj}. \tag{2.31}$$

The integral limits for x are always 0 to ∞, and for ξ they are -1 to 1. From now on we will stop writing out the limits explicitly to make the equations easier to read.

By construction, the perturbations to particle density, mean flow and temperature associated with H_{1A} are all zero. These constraints give

$$\int dx d\xi d\varphi\, x^{1/2} M(\mathbf{w}) H_{1A} = 0, \tag{2.32}$$

where we have changed variables of integration to ξ and x ($d^3\mathbf{w} = dx d\xi d\varphi\, x^{1/2} v_{t\infty}^3/2$), and $M(\mathbf{w}) = \{1, w_\parallel, w_\parallel^2 + w_\perp^2\}$. We express the components of $M(\mathbf{w})$ in terms of the Sonine-Legendre polynomials, that is,

$$1 = L_0^{(1/2)}(x) P_0(\xi) \tag{2.33}$$

$$w_\parallel = x^{1/2} L_0^{(3/2)}(x) P_1(\xi) \tag{2.34}$$

$$w_\parallel^2 + w_\perp^2 = \left(\frac{3}{2} L_0^{(1/2)} - L_1^{(1/2)}\right) P_0(\xi), \tag{2.35}$$

where we have used $P_0(\xi) = 1$, $P_1(\xi) = \xi$, $L_0^{(j)}(x) = 1$ and $L_1^{(1/2)}(x) = 3/2 - x$. Then, using identities (2.30) and (2.31), together with the expansion (2.29), equation (2.32) gives

$$a_{0,0} = a_{0,1} = a_{1,0} = 0. \tag{2.36}$$

We multiply both sides of equation (2.27) by $x^{j/2}L_p^{(j+1/2)}(x)P_j(\xi)$ and integrate over velocity space to get

$$\begin{aligned}
&\sum_{q,k} a_{q,k} \int d^3\mathbf{w} x^{j/2} L_p^{(j+1/2)}(x) P_j(\xi) C_s^{(l)}[x^{k/2} L_q^{(k+1/2)}(x) P_k(\xi) f_{Ms}] \\
&= \frac{n_\infty}{2\pi^{3/2}} \frac{c_s}{\lambda_{MFP}} \frac{T_0}{T_\infty} \int dx d\xi d\varphi \, x^{j/2+1/2} L_p^{(j+1/2)}(x) P_j(\xi) e^{-x} \\
&\times \left[\left(1 + \xi x^{1/2} \frac{v_{t\infty}}{c_s}\right) \left(x - 3\xi x^{1/2} \frac{c_s}{v_{t\infty}}\right) + \frac{3ZT_e}{2T_\infty} \xi x^{1/2} \frac{v_{t\infty}}{c_s} \right],
\end{aligned} \tag{2.37}$$

where on the right hand side, we used equations (2.17), (2.22) and (2.25). Due to rotational invariance, the linearised collision operator is diagonal in the basis of Legendre polynomials. Therefore, from (2.31), integration over ξ gives zero for all values of k in $P_k(\xi)$ except for $k = j$ and so the sum over k in (2.29) picks out $k = j$ elements only. In the end the equations simplify to

$$\begin{aligned}
\sum_q^\infty a_{q,j}(-n_\infty \nu_c) K_{p,q}^{(j)} &= \frac{n_\infty}{\pi^{1/2}} \frac{c_s}{\lambda_{MFP}} \frac{T_0}{T_\infty} \\
&\times \left[-2 \int dx d\xi \, x^{j/2+3/2} L_p^{(j+1/2)}(x) L_0^{(5/2)}(x) P_j(\xi) P_2(\xi) e^{-x} \right. \\
&\left. - \frac{v_{t\infty}}{c_s} \int dx d\xi d\varphi \, x^{j/2+1} L_p^{(j+1/2)}(x) L_1^{(3/2)}(x) P_j(\xi) P_1(\xi) e^{-x} \right],
\end{aligned} \tag{2.38}$$

where we have defined

$$K_{p,q}^{(j)} = -\frac{1}{n_\infty \nu_c} \int d^3\mathbf{w} x^{j/2} L_p^{(j+1/2)}(x) P_j(\xi) C_s^{(l)}[x^{j/2} L_q^{(j+1/2)}(x) P_j(\xi) f_{Ms}], \tag{2.39}$$

and we have used $P_2(\xi) = 3\xi^2/2 - 1/2$, $L_0^{(j)}(x) = 1$ and $L_1^{(3/2)}(x) = 5/2 - x$. These integrals can be found analytically. This is a tedious, but standard, calculation following that of Braginskii. Using the polynomial properties (2.31) and (2.30), we obtain

$$\sum_{q=0}^\infty a_{q,j} K_{p,q}^{(j)} = \frac{5T_0}{4T_\infty} \left[\frac{6}{5} \frac{c_s}{v_{t\infty}} \delta_{p0}\delta_{j2} + \delta_{j1}\delta_{p1} \right]. \tag{2.40}$$

To find the coefficients, we can solve the equation above by truncating the expansion (2.29) to $q = 4$. To this order, the matrices on the left hand side of (2.40) are

$$K^{(1)} = \begin{pmatrix} 0 & 0 & 0 & 0 \\ 0 & 1.000 & 0.7500 & 0.4687 \\ 0 & 0.7500 & 2.813 & 2.414 \\ 0 & 0.4687 & 2.414 & 5.524 \end{pmatrix}, \qquad K^{(2)} = \begin{pmatrix} 0.9000 & 0.6750 & 0.4218 & 0.2460 \\ 0.6750 & 3.843 & 3.438 & 2.522 \\ 0.4218 & 3.438 & 10.44 & 9.916 \\ 0.2460 & 2.522 & 9.916 & 22.34 \end{pmatrix} \tag{2.41}$$

For our purposes, the important coefficients turn out to be

$$a_{1,1} = 1.580\frac{T_0}{T_\infty}, \tag{2.42}$$

$$a_{0,2} = 1.931\frac{c_s}{v_{t\infty}}\frac{T_0}{T_\infty}. \tag{2.43}$$

We now find a solution for H_{1B} by solving equation (2.28). Note that the collision operator linearised with respect to f_M is

$$C^{(l)}[H] \simeq C_s^{(l)}[H] + \Delta_s C\left[H, \frac{2w_\parallel c_s}{v_{t\infty}^2} f_{Ms}\right] + \Delta_s C\left[\frac{2w_\parallel c_s}{v_{t\infty}^2} f_{Ms}, F\right]. \tag{2.44}$$

The subscript s appears only on the first collision operator on the right side, indicating that it is with respect to f_{Ms}. Result (2.44) implies that equation (2.28) is equivalent to solving

$$C^{(l)}[H_0 + \epsilon H_{1B}] = 0. \tag{2.45}$$

The solution to this equation is

$$H_0 + \epsilon H_{1B} = \left[\frac{\delta n}{n_\infty} + \frac{m(v_\parallel - u_{\parallel\infty})}{T_\infty}\delta u + \frac{\delta T}{T_\infty}\left(\frac{(v_\parallel - u_{\parallel\infty})^2 + v_\perp^2}{v_{t\infty}^2} - \frac{3}{2}\right)\right] f_M, \tag{2.46}$$

where $\delta n = n_0 + \epsilon n_1$, $\delta u = u_0 + \epsilon u_1$, $\delta T = T_0 + \epsilon T_1$ are density, mean flow, and temperature perturbations to first order in ϵ, respectively. We use this expansion and the expansion of f_M and $u_{\parallel\infty}$ in Δ_s, as well as equality (2.21), to get

$$\begin{aligned} H_{1B} =& \frac{2c_s}{v_{t\infty}}\frac{\Delta_s}{\epsilon}\left[\frac{3}{2}\frac{c_s}{v_{t\infty}} - \frac{w_\parallel}{v_{t\infty}} - \frac{3w_\parallel^2}{v_{t\infty}^2}\frac{c_s}{v_{t\infty}} + \frac{w_\parallel}{v_{t\infty}}\frac{w^2}{v_{t\infty}^2}\right]\frac{T_0}{T_\infty} f_{Ms} \\ &+ \left[\frac{n_1}{n_\infty} + \frac{2w_\parallel}{v_{t\infty}^2}u_1 + \frac{T_1}{T_\infty}\left(\frac{w^2}{v_{t\infty}^2} - \frac{3}{2}\right)\right] f_{Ms}. \end{aligned} \tag{2.47}$$

Quasineutrality then gives

$$\Phi_1 = \frac{T_e}{e}\frac{n_1}{n_\infty}. \tag{2.48}$$

We proceed to find the relationship between Δ_s and ϵ by taking the moments of the second order equation.

2.2.3 Second order

Keeping terms of second order in ϵ and Δ_s in equation (2.11), we get

$$\begin{aligned}\text{Collisional terms } =&\frac{\epsilon^2 c_s}{\lambda_{MFP}}\Bigg[H_{1A}+H_{1B}+\frac{w_\parallel}{c_s}H_{1A}+\frac{w_\parallel}{c_s}H_{1B}\\&-\frac{Ze\Phi_1}{mc_s}\frac{\partial f_{Ms}}{\partial w_\parallel}-\frac{\Delta_s}{\epsilon}\frac{Ze\Phi_0}{mc_s}\frac{2c_s}{v_{t\infty}^2}\frac{\partial(f_{Ms}w_\parallel)}{\partial w_\parallel}\Bigg].\end{aligned}\tag{2.49}$$

We multiply this equation by $1, w_\parallel$ and w^2, integrate over velocity, and use (2.29) and (2.47) to get a system of linear equations with a singular matrix,

$$\begin{pmatrix}1 & 1 & 0\\ \frac{1+ZT_e/T_\infty}{5/3+ZT_e/T_\infty} & 1 & \frac{1}{5/3+ZT_e/T_\infty}\\ 3/2 & 5/2 & 3/2\end{pmatrix}\begin{pmatrix}n_1/n_\infty\\ u_1/c_s\\ T_1/T_\infty\end{pmatrix}=\begin{pmatrix}-3T_0\Delta_s/2T_\infty\epsilon\\ 3T_0\Delta_s/2T_\infty\epsilon-v_{t\infty}^2a_{0,2}/2c_s^2\\ -\frac{15}{4}T_0\Delta_s/T_\infty\epsilon+\frac{5v_{t\infty}}{4c_s}a_{1,1}\end{pmatrix}.\tag{2.50}$$

The integrals required to arrive at this result are given in Appendix D. Since the matrix in (2.50) is singular (see Section 2.2.2), it has a zero eigenvalue. The left eigenvector corresponding to the zero eigenvalue is $(-ZT_e/T_\infty, 5/3+ZT_e/T_\infty, -2/3)$. Multiplying both sides of (2.50) by this vector allows us to find

$$\frac{T_0\Delta_s}{T_\infty\epsilon}=\frac{5v_{t\infty}a_{1,1}/6c_s+a_{0,2}}{5+3ZT_e/T_\infty}.\tag{2.51}$$

Using values for the coefficients $a_{1,1}$ and $a_{0,2}$, given in equation (2.42), we get

$$\frac{\Delta_s}{\epsilon}=\frac{1}{h\left(\frac{ZT_e}{2T_\infty}\right)},\tag{2.52}$$

where, for convenience later, we have defined a function

$$h(z)\equiv\frac{(2.75+3.30z)^{3/2}}{1.93z+2.93}.\tag{2.53}$$

Since ϵ must be positive for a solution that does not diverge exponentially far away from the wall, Δ_s must also be positive, giving $u_{\parallel\infty}>c_s$. This means that the flow along the field lines of the Maxwellian at our boundary far away from the wall has to be at least sonic. The decay length of the perturbation λ diverges as we approach sonic velocity, that is, as Δ_s goes to zero.

2.3 Numerical results

We solve the drift kinetic equation (1.19) with quasineutrality (1.3) and adiabatic electrons (1.4) using a code we developed, which is presented in Chapter 4. The code uses normalised variables

$$\begin{aligned} \bar{x} &\equiv \frac{3\sqrt{\pi}\nu_c}{2^{5/2}v_{t\infty}\sin\alpha}x, & \bar{v}_{\parallel,\perp} &\equiv \frac{v_{\parallel,\perp}}{v_{t\infty}}, & \bar{u}_{\parallel\infty} &\equiv \frac{u_{\parallel\infty}}{v_{t\infty}}, \\ \bar{f} &\equiv \frac{f v_{t\infty}^3}{n_\infty}, & \bar{\phi} &\equiv \frac{Ze\phi}{2T_\infty}, & \bar{T}_e &\equiv \frac{ZT_e}{2T_\infty}, \end{aligned} \tag{2.54}$$

where ν_c is the collision frequency, given in (2.14).

Integrating the distribution function, given by (2.3), and using quasineutrality (2.12) and the orderings (2.5), we find $n_\infty e\phi/T_e = N\exp(-x/\lambda\sin\alpha)$, where we have introduced $N \equiv \int d^3\mathbf{v}H$. In normalised variables, and using relationship (2.52) to substitute for λ, we find

$$\frac{\bar{\phi}}{\bar{T}_e} = \frac{N}{n_\infty}\exp\left(-\frac{2^{5/2}}{3\sqrt{\pi}}\Delta_s h(\bar{T}_e)\bar{x}\right) \tag{2.55}$$

In Figure 2.1 we plot $\bar{\phi}/\bar{T}_e$ against $\bar{x}$ for $\Delta_s = -0.05, 0.01, 0.1$ and $\bar{T}_e = 0.5$ for two different sizes of the $\bar{x}$ space domain. The domain size is defined by $\bar{x}_{N_x-1}$. Here N_x is the number of grid points in the system, $x_0 = 0$ corresponds to the MPE and x_{N_x-1} to the boundary at $x \to \infty$. As predicted by our analytical results, the simulation with a mean flow $\Delta_s < 0$, does not converge as we increase the distance from the wall, and we find a large electric field for large $\bar{x}$. For $\Delta_s > 0$ the simulations are better converged, but we note that a larger box is required for simulations with smaller Δ_s. This is because the perturbation length scale λ is longer for smaller Δ_s, which, qualitatively, agrees with equation (2.52).

To determine if relationship (2.52) holds quantitatively, we take the logarithm of (2.55) (keeping in mind that $N < 0$ and $\bar{\phi} < 0$) to get

$$\ln\left(-\frac{\bar{\phi}}{\bar{T}_e}\right) = -\frac{2^{5/2}}{3\sqrt{\pi}}\Delta_s h(\bar{T}_e)\bar{x} + \ln(-N/n_\infty). \tag{2.56}$$

At large $\bar{x}$ we expect a linear plot of the potential on a log-linear scale.

We plot $-\bar{\phi}/\bar{T}_e$ against $\bar{x}$ for runs with $\Delta_s = 0.01, 0.02, 0.05, 0.1, 0.25, 0.5, 0.7, 1.0$ and $\bar{T}_e = 0.5$ in the left plot in Figure 2.2. The linear fits (dashed lines in the plot) fit the results well for most of the runs, agreeing with our prediction of an exponential decay of

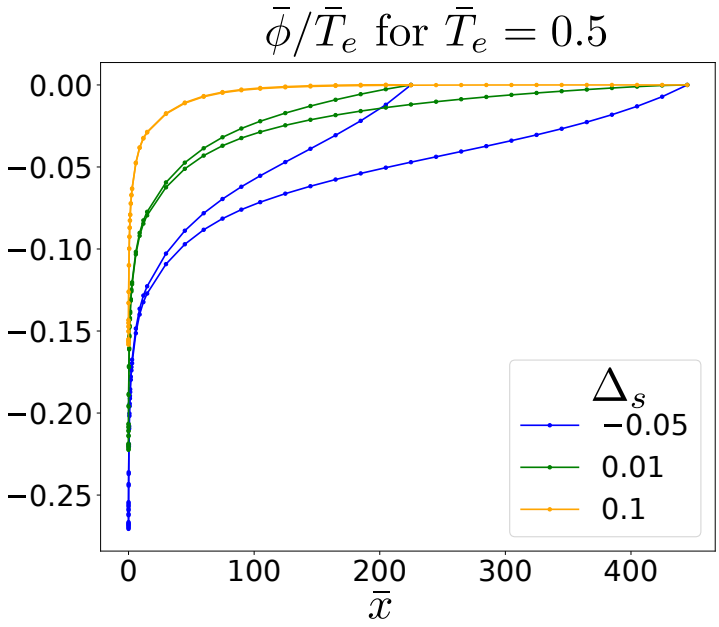

Figure 2.1: $\bar{\phi}/\bar{T}_e$ against $\bar{x}$ for $\Delta_s = -0.05, 0.01, 0.1$ and $\bar{T}_e = 0.5$ for two different box sizes, in normalised units $\bar{x}_{N_x-1} = 220$ and $\bar{x}_{N_x-1} = 440$. For $\Delta_s < 0$ we find a large electric field near the boundary at infinity and the solution depends strongly on box size. For $\Delta_s = 0.01$, the solutions have small electric field at large $\bar{x}$ and vary less with box size, but an even larger box size than $\bar{x} = 440$ is required to fully resolve the simulation. For $\Delta_s = 0.1$ the perturbation is already negligible near $\bar{x} = 220$ and the box size does not make a big difference.

the perturbation. Due to numerical errors, the potential can overshoot zero at large $\bar{x}$ and become slightly negative. We choose to cut off the plot at a chosen maximum value of $\bar{x}$. We choose that value to be two grid points before the potential reaches zero (or becomes negative), this way making the log-linear plots easier to read. For large Δ_s the potential decays to zero very quickly and the linear fit is performed over a few grid points only, which introduces an error.

For $\Delta_s \ll 1$ we expect the relationship (2.56) to be valid. Therefore, for a constant $\bar{T}_e$, the ratio of the absolute value of the slope to Δ_s (we will denote this ratio as r_T) is constant and equal to

$$r_T = h(\bar{T}_e)\frac{2^{5/2}}{3\sqrt{\pi}}. \tag{2.57}$$

For $\bar{T}_e = 0.5$, this gives $r_T \approx 2.52$. The values of r_T obtained using linear regression on the exponential part of the curve are shown in the right plot in Figure 2.2. The r_T values for all the simulations are far from the expected value of 2.52. The r_T value is relatively constant in the region $0.05 < \Delta_s < 0.7$ and is on average 0.24, which indicates that the

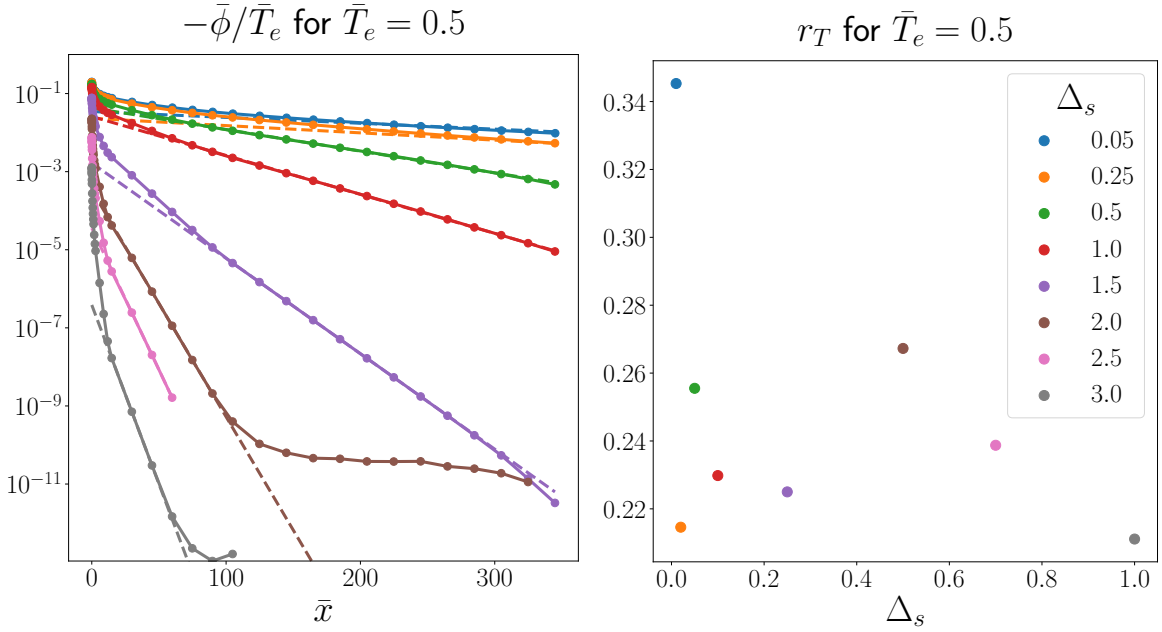

Figure 2.2: Simulation results for $\Delta_s = 0.01, 0.02, 0.05, 0.1, 0.25, 0.5, 0.7, 1.0$ and $\bar{T}_e = 0.5$. The legend is shown in the right plot. **Left:** $\bar{\phi}/\bar{T}_e$ against $\bar{x}$ on a log-linear scale. The dashed lines are the best linear fits of the curves. **Right:** The value of r_T for different values of Δ_s. The relationship (2.56) predicts $r_T \approx 2.52$ for all values of Δ_s. The value is approximately constant for $0.05 < \Delta_s < 0.7$, however, it is about ten times smaller than the expected result.

linear relationship (2.56) holds in this interval of Δ_s, although it is smaller than predicted by a factor of ~ 10.

Large deviation from the expected linear relationship (2.56) between Δ_s and ϵ (and thus a constant value of r_T) for the smallest value of Δ_s requires further investigation. Here we offer potential explanations for this discrepancy. Note that the explanations presented below can explain why r_T is different at small Δ_s, but they cannot explain why the measured value of r_T is 10 times smaller than the expected value.

As argued earlier, when Δ_s decreases, the perturbation length scale λ increases, and thus, the box size $\bar{x}_{N_x-1}$ has to be made larger (see Figure 2.1). Therefore, to get the correct potential profile, simulations with $\Delta_s = 0.01$ and $\Delta_s = 0.02$ were run with $\bar{x}_{N_x-1} = 3000$, whereas all the other simulations in Figure 2.2 had $\bar{x}_{N_x-1} = 440$. Using $\bar{x}_{N_x-1} = 440$ for $\Delta_s = 0.01$, gave $r_T = 0.7$, far larger than the values for all the other runs. This is because for the smaller $\bar{x}_{N_x-1}$ the gradients at large x were not resolved and were overestimated. Increasing the box size even more for $\Delta_s = 0.01$ should reduce the value of r_T and bring it closer to the values found from simulations with larger Δ_s, this is left for

future work. We note that increasing $\bar{x}_{N_x-1}$ for the runs with $\Delta_s \geq 0.05$ had a negligible effect on the potential profile and the value of r_T.

A more quantitative constraint could be estimated as follows. The model used assumes

$$\frac{1}{\epsilon} = \frac{\lambda}{\lambda_{MFP}} \ll \frac{x}{\lambda_{MFP} \sin\alpha} = \frac{2^{5/2}}{3\sqrt{\pi}}\bar{x}. \tag{2.58}$$

The value of $\bar{x}$ is limited by our simulation domain: the decay length scale λ has to fit in the domain, therefore ϵ, and thus Δ_s (see equation (2.52)), cannot be too small. Taking $\bar{x} = \bar{x}_{N_x-1}$, where $\bar{x}_{N_x-1}$ is the size of our simulation box, the condition becomes

$$\epsilon \gg \frac{1}{\bar{x}_{N_x-1}}, \tag{2.59}$$

where we took $3\sqrt{\pi}/2^{5/2} \approx 1$. For simulation domains, which used $\bar{x}_{N_x-1} \approx 400$, the constraint (2.59) gives $\Delta_s \sim \epsilon \gg 0.003$. The simulations shown above seem to be well above this lower limit, where the smallest value of Δ_s used is 0.01. However, it shows that we have to be careful with the box size at the smallest values of Δ_s. Running more simulations with larger $\bar{x}_{N_x-1}$ is an obvious next step in figuring out the discrepancies.

We now look at how well the dependence on $\bar{T}_e$ is captured by the relationship (2.52). In the left plot of Figure 2.3 we plot $-\bar{\phi}/\bar{T}_e$ against $\bar{x}$ for runs with $\Delta_s = 0.1$ and $\bar{T}_e = 0.05, 0.25, 0.5, 1.0, 1.5, 2.0, 2.5, 3.0$. We see that the linear fit works well for all values of $\bar{T}_e$. In the right plot of Figure 2.3 we plot r_Δ values for different $h(\bar{T}_e)$, where

$$r_\Delta \equiv \Delta_s 2^{5/2}/(3\sqrt{\pi}). \tag{2.60}$$

For $\Delta_s = 0.1$ we expect $r_\Delta \approx 0.10$ for all $\bar{T}_e$. The values obtained from these simulations are far from the expected value and seem to depend on $h(\bar{T}_e)$. There is a region $\bar{T}_e < 1.0$, where the value of $r_\Delta \approx 0.01$ is constant, however our analytical calculation does not assume any ordering of $\bar{T}_e$ and so the value of r_Δ should be constant everywhere, indicating that the function $h(\bar{T}_e)$ in equation (2.52) might not be correct.

Further work is needed to determine why the numerical solutions do not agree with the analytical predictions. The calculation should be checked again to make sure that all the normalisation factors have been used appropriately and that no arithmetic mistakes have been made, which could explain the factor of 10 discrepancy between the obtained and expected values of r_Δ. A mistake in the function $h(\bar{T}_e)$ could also explain the observed behaviour of r_T. Furthermore, the numerically implemented collision operator should be

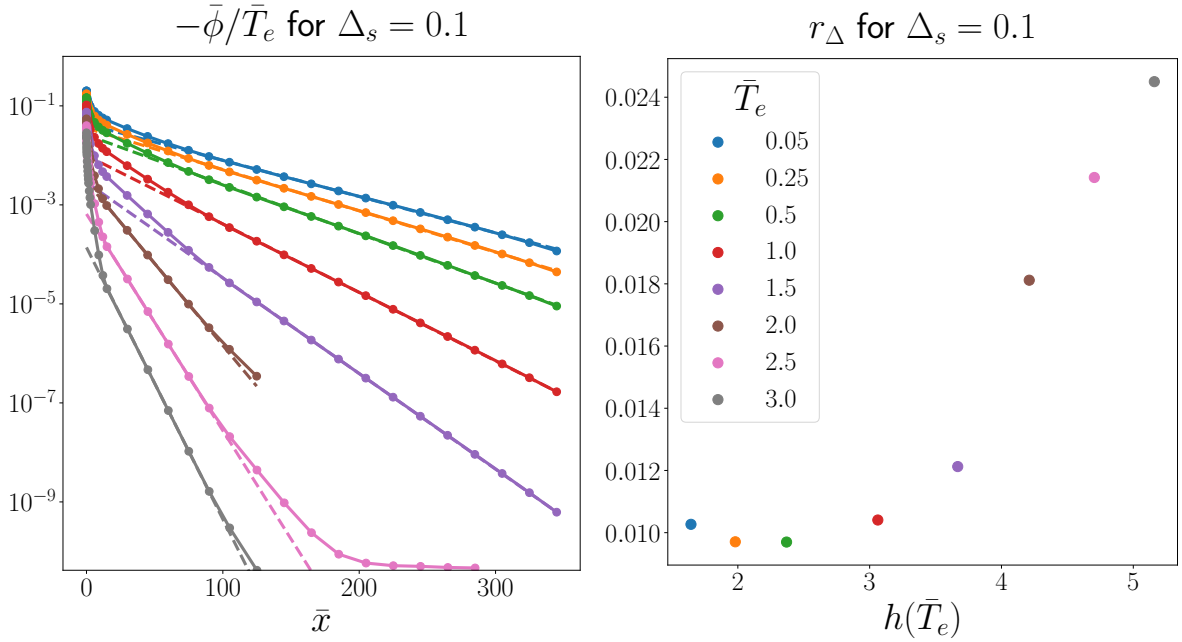

Figure 2.3: Simulation results for $\Delta_s = 0.1$ and $\bar{T}_e = 0.05, 0.25, 0.5, 1.0, 1.5, 2.0, 2.5, 3.0$. The legend is shown in the right plot. **Left:** $\bar{\phi}/\bar{T}_e$ against $\bar{x}$ on a log-linear scale. The dashed lines are the best linear fits of the curves. **Right:** The value of r_Δ for different values of $\bar{T}_e$. The relationship (2.56) predicts $r_\Delta \approx 0.10$ for all values of $\bar{T}_e$. The value is approximately constant for $\bar{T}_e < 1.0$, however, it is about ten times smaller than the expected result.

used to compute integrals (2.39) and the results compared to the analytic results (2.41), then the rest of the calculation could be followed step by step to find any errors. The preliminary computations performed seem to show that the collision operator does not recover the expected expressions (2.41), although the code for calculating these expressions with the numerical collision operator needs to be investigated more carefully. This is left for future work.

Chapter 3

Electric potential near $x = 0$

In this chapter we show that the electric field at $x = 0$ diverges and the potential scales as $\hat{\phi} \sim \sqrt{x}$, where $\hat{\phi} \equiv \phi(x) - \phi(x = 0)$. As a result, the distribution function at $x = 0$ is exponentially small at small parallel velocities and satisfies the kinetic Chodura condition

$$\frac{Z^2 T_e}{m} \int d^3\boldsymbol{v} \frac{f(x=0)}{{v_\parallel}^2} = n_e(x = 0). \tag{3.1}$$

By satisfying this condition, the distribution function at $x = 0$ can be used as the distribution function at the entrance of the magnetic presheath – see [33] for more details on why the distribution function needs to satisfy (3.1) at the entrance of the magnetic presheath.

In Section 3.1 we show that there does not exist a self consistent solution to our equations for potential that is of size $e\hat{\phi}/T_e \lesssim (x/\lambda_{MFP} \sin\alpha)^{2/3}$ for $x/\lambda_{MFP} \sin\alpha \ll 1$. In Section 3.2 we prove that the kinetic Chodura condition is satisfied and that for $x/\lambda_{MFP} \sin\alpha \ll 1$, $\hat{\phi}$ scales as $x^{1/2}$.

3.1 Finding a lower bound for the electric potential

We use variables defined in (2.54) to introduce the normalised collision operator

$$\bar{C}[\bar{f}, \bar{f}] \equiv \frac{m^2 v_{t\infty}^6}{\gamma_{ii} n_\infty^2} C[f, f] = \nabla_{\bar{v}} \cdot \int d^3\bar{\mathbf{v}} \nabla_{\bar{g}} \nabla_{\bar{g}} \bar{g} \cdot (\bar{f}(\bar{\mathbf{v}}')\nabla_{\bar{v}} \bar{f}(\bar{\mathbf{v}}) - \bar{f}(\bar{\mathbf{v}})\nabla_{\bar{v}'} \bar{f}(\bar{\mathbf{v}}')). \tag{3.2}$$

In these variables, quasineutrality (1.3) (with adiabatic electrons (1.4)) and the steady state drift kinetic equation (1.19) are

$$-\bar{v}_\parallel \frac{\partial \bar{f}}{\partial \bar{x}} + \frac{\partial \bar{\phi}}{\partial \bar{x}} \frac{\partial \bar{f}}{\partial \bar{v}_\parallel} = \bar{C}[\bar{f}, \bar{f}], \tag{3.3}$$

$$\bar{n} \equiv \int d^3\bar{\mathbf{v}} \bar{f} = \exp\left(\frac{\bar{\phi}}{\bar{T}_e}\right), \tag{3.4}$$

where $\bar{n} = n/n_\infty$ is the ion density normalised to density at the boundary at $x \to \infty$. The kinetic Chodura condition (3.1) becomes

$$\bar{T}_e \int d^3\bar{\boldsymbol{v}} \frac{\bar{f}(\bar{x}=0)}{\bar{v}_\parallel^2} = \bar{n}(\bar{x}=0), \tag{3.5}$$

From here on we will drop bars in the normalised variables. We will make it explicit when we go back to dimensional variables.

To study the distribution function near $x = 0$, it is convenient to use the potential relative to the wall $\hat{\phi} = \phi - \phi(x=0)$, and to change variables from $(x, v_\parallel)$ to (x, U, σ), where $U \equiv \sqrt{v_\parallel^2 + 2\hat{\phi}}$ and $\sigma \equiv v_\parallel/|v_\parallel| = \pm 1$. Then the left hand side of equation (3.3) simplifies to

$$-v_\parallel \left.\frac{\partial f}{\partial x}\right|_{v_\parallel, v_\perp} + \left.\frac{\partial \hat{\phi}}{\partial x}\frac{\partial f}{\partial v_\parallel}\right|_{x, v_\perp} = -\sigma\sqrt{U^2 - 2\hat{\phi}} \left.\frac{\partial f}{\partial x}\right|_{U, v_\perp}. \tag{3.6}$$

Here we show explicitly which variables we are keeping constant in the partial derivatives. Using variable U and expanding f around $x = 0$ and $U = v_\parallel > 0$ we find

$$\begin{aligned} f(x,U) - f(0,v_\parallel) = (U - v_\parallel) \left.\frac{\partial f}{\partial U}\right|_{x,v_\perp} (x=0, U=v_\parallel) \\ + x \left.\frac{\partial f}{\partial x}\right|_{U,v_\perp} (x=0, U=v_\parallel) + O((U-v_\parallel)^2, x^2). \end{aligned} \tag{3.7}$$

Here we explicitly show that the partial derivatives are evaluated at $U = v_\parallel$ and $x = 0$. Note that for $v_\parallel > 0$ we have $U(x=0, v_\parallel) = v_\parallel$, and thus $\partial f/\partial U$ at $x = 0$ and $U = v_\parallel$ is $\partial f/\partial v_\parallel$, which we will use from here on. The use of these variables permits a non linear dependence on x through the $U - v_\parallel$ term. For $v_\parallel^2 \gg 2\hat{\phi}$, we approximate $U - v_\parallel \simeq \hat{\phi}/v_\parallel + O(\hat{\phi}^2/v_\parallel^3)$. Then (3.7) can be written as

$$f(x,U) - f(0,v_\parallel) = \frac{\hat{\phi}}{v_\parallel}\frac{\partial f}{\partial v_\parallel} - \frac{x}{v_\parallel} C[f,f](x=0) + O(\hat{\phi}^2, x^2), \tag{3.8}$$

where we have used (3.3) and (3.6) to introduce $C[f, f]$ in the equation. We see that we have a divergence at $v_\parallel = 0$, which we need to resolve by analysing the behaviour of the function at the values of $v_\parallel$ where the corrections become as large as the function at $x = 0$.

Approximation (3.8) can fail for sufficiently small $v_\parallel$ due to $v_\parallel$ appearing in the denominator. To determine for which values of $v_\parallel$ this happens, we assume that the potential can be expanded in fractional powers of x, $\hat{\phi} \simeq Px^\beta$, where P and β are positive constants.

We also assume that $\partial^n f/\partial v_\parallel^n \sim f/v_\parallel^n$ for $v_\parallel \ll 1$. Then, we can approximate the collision operator by the diffusion term $C[f,f] \simeq D_0 \partial^2 f/\partial v_\parallel^2$, where D_0 is a function of $v_\perp$ but not of $v_\parallel$ – proof of this is given in Appendix E.1 (note that here we have removed the bars that we used to denote normalised quantities and D_0 is the normalised D_0, called $\bar{D}_0$ in Appendix E.1). With these approximations the terms on the right hand side of equation (3.8) scale as

$$\frac{1}{f}\frac{\hat{\phi}}{v_\parallel}\frac{\partial f}{\partial v_\parallel} \sim x^\beta v_\parallel^{-2}, \qquad \frac{1}{f}\frac{x}{v_\parallel}C[f,f](x=0) \simeq \frac{1}{f}\frac{x}{v_\parallel}D_0\frac{\partial^2 f}{\partial v_\parallel^2} \sim x v_\parallel^{-3}. \tag{3.9}$$

We look for a relation between x and $v_\parallel$ for which one or both of the terms above become $O(1)$ and hence expression (3.8) is not valid. The value of β will determine the dominant balance:

- For $\beta > 2/3$, the collisional term becomes $O(1)$ at $x \sim v_\parallel^3$. The potential term at this spatial scale is $O(v_\parallel^{3\beta-2}) \ll 1$.
- For $\beta = 2/3$, both terms are $O(1)$ at $x \sim v_\parallel^3$.
- For $\beta < 2/3$, the potential term becomes $O(1)$ at $x \sim v_\parallel^{2/\beta}$. The collisional term at this spatial scale is $O(v_\parallel^{2/\beta-3}) \ll 1$.

In the rest of this section, we prove that β must be smaller than $2/3$ for the solutions to be self consistent.

3.1.1 Looking for a self similar solution for $\beta > 2/3$

We first assume that $\beta > 2/3$, which we will show results in a contradiction. At the wall ($x = 0$), for $v_\parallel \sim 1$ the collision operator is finite because the distribution function is smooth in $v_\parallel$. As argued earlier, at $v_\parallel \ll 1$, $C[f,f] \simeq D_0 \partial^2 f/\partial v_\parallel^2$, where D_0 is a function of $v_\perp$ only. Then the drift kinetic equation (1.19) in this region simplifies to

$$-v_\parallel \frac{\partial f}{\partial x} + \frac{\partial \hat{\phi}}{\partial x}\frac{\partial f}{\partial v_\parallel} = D_0 \frac{\partial^2 f}{\partial v_\parallel^2}. \tag{3.10}$$

We are going to consider solutions $f(x=0)$ that, for $v_\parallel > 0$, tend to zero at $v_\parallel = 0$ algebraically, $f(x=0, v_\perp, v_\parallel \ll 1) = A(v_\perp) {v_\parallel}^{3\Omega}$, where $A(v_\perp)$ is a function of $v_\perp$ only. It will become obvious soon why using 3Ω as the exponent is convenient. These solutions cause the difference $f(x) - f(x=0)$ in equation (3.8) to diverge at $v_\parallel = 0$. We will show

that formula (3.8) is not valid for $v_\parallel \sim x^{1/3}$, and we will find a different form of $f(x, v_\perp, v_\parallel)$ near $x = 0$ and for $v_\parallel \sim x^{1/3}$. When we calculate $f(x, v_\perp, v_\parallel)$ for small $v_\parallel$, we will find out that Ω is not a free parameter, and it must be chosen to be $1/6$, that is, $f(x = 0)$ tends to zero as ${v_\parallel}^{1/2}$.

For $\beta > 2/3$ we can neglect the potential terms in (3.10). This is because from the expansion (3.8) and scalings (3.9), the second derivative of f with respect to $v_\parallel$ becomes large at $x^{1/3} \sim v_\parallel$, but the potential term at this scale is of size $x^{\beta-2/3} \ll 1$. The final equation is then

$$-v_\parallel \frac{\partial f}{\partial x} = D_0 \frac{\partial^2 f}{\partial v_\parallel^2} \tag{3.11}$$

We solve (3.11) for small $v_\parallel$ by noticing that the lack of characteristic spatial and velocity scales scales suggests the existence of a self similar solution. To find it we introduce a variable $\eta \equiv v_\parallel/(D_0 x)^{1/3}$, which is implicitly also a function of $v_\perp$ via the D_0 dependence. We choose the form $f(x, v_\perp, v_\parallel) = (D_0 x)^\Omega F(\eta)$ for the solution, where $\Omega > 0$ is an unknown constant. From the properties of f, we require F and its derivative to be continuous and $F > 0$ for all η. Positivity of Ω is required to make sure that the distribution function does not diverge at the wall. As we announced earlier, we will show later that equation (3.11) with the requirement of positivity can only be satisfied for $\Omega = 1/6$. We proceed to show that this implies that $f \sim v_\parallel^{1/2}$ at $x = 0$.

With the ansatz $f(x, v_\perp, v_\parallel) = (D_0 x)^\Omega F(\eta)$, equation (3.10) becomes an ordinary differential equation

$$F'' - \frac{\eta^2}{3} F' + \Omega \eta F = O(x^{\beta-2/3}), \tag{3.12}$$

where the primes indicate derivatives, $F' \equiv \frac{\mathrm{d}F}{\mathrm{d}\eta}$, and the right hand side is the error associated with the neglected potential terms. We will only keep the lowest order terms, so this term is ignored.

It is useful to find solutions to equation (3.12) in the limit of $|\eta| \gg 1$. The second order equation (3.12) must have two independent solutions. We find the first one by assuming the n^{th} derivative scales as $F^{(n)} \sim F/\eta^n$. Equation (3.12) then simplifies to

$$-\frac{\eta^2}{3} F' + \Omega \eta F = 0. \tag{3.13}$$

The solution to this equation is

$$F(\eta \to \pm\infty) \simeq A(v_\perp)\eta^{3\Omega}, \tag{3.14}$$

where the function $A(v_\perp)$ is an integration constant. We will stop writing the explicit dependence of A on $v_\perp$ from here on. Equation (3.14) implies that $(D_0 x)^\Omega F(\eta) \to A v_\parallel^{3\Omega}$ for $x \to 0$. To find the second solution for large η, we balance the first two terms of equation (3.12) and assume that $F \ll F' \ll F''$. This gives

$$F'' - \frac{\eta^2}{3}F' = 0. \tag{3.15}$$

The solution to this equation is $F' = N(v_\perp)\exp(\eta^3/9)$, where the function $N(v_\perp)$ is an integration constant, and the dependence of N on $v_\perp$ will not be explicitly shown again in the rest of the chapter. We can find the behaviour of this solution at $|\eta| \gg 1$ by integrating equation (3.15) from η_0 to η, where $\eta_0 < \eta$,

$$\begin{aligned} F(\eta) - F(\eta_0) &= N\int_{\eta_0}^{\eta} d\eta' \exp\big(\eta'^3/9\big) \\ &= 3N\frac{\exp(\eta^3/9)}{\eta^2} - 3N\frac{\exp(\eta_0^3/9)}{\eta_0^2} + 6N\int_{\eta_0}^{\eta} d\eta' \frac{\exp(\eta'^3/9)}{\eta'^3}. \end{aligned} \tag{3.16}$$

Here, to get the second equality, we integrated by parts. Since $\eta_0 < \eta$ the first term on the right hand side dominates over the second one. The last term is much smaller than the left hand side since everywhere in the integration region $\eta'^3 \gg 1$ and so

$$\int_{\eta_0}^{\eta} d\eta' \frac{\exp(\eta'^3)}{\eta'^3} \ll \int_{\eta_0}^{\eta} d\eta' \exp\Big(\eta'^3/9\Big). \tag{3.17}$$

Therefore, our second solution in the $|\eta| \gg 1$ limit is

$$F(\eta \to \pm\infty) \simeq 3N\frac{\exp(\eta^3/9)}{\eta^2}. \tag{3.18}$$

We look for solutions that decay to zero as $\eta \to -\infty$ and do not grow exponentially as $\eta \to \infty$. The first constraint comes from the boundary condition $f(v_\parallel \to -\infty) = 0$. The second one comes from our assumption $f(x=0) = A{v_\parallel}^{3\Omega}$. In the next few paragraphs we will show that only $\Omega = 1/6$ satisfies the conditions and gives $F > 0$. We will eventually show (see Section 3.2.1) that $\beta < 2/3$ and that $f(x=0)$ goes to zero exponentially fast when $v_\parallel$ goes to zero. The keen reader will then think whether we could have assumed $f(x=0)$ to have this exponential dependence on velocity in this section about potentials

with $\beta > 2/3$. This is indeed the case, but one needs to realize that $f(x = 0)$ is not a choice, but a result of our calculation. We could in principle tailor $f(x = 0)$ by choosing the right boundary conditions, but in this problem the boundary conditions are set. We believe that most boundary conditions will lead to solutions $f(x = 0) \simeq A{v_\parallel}^{1/2}$. Technically, what we have just shown is that, with potentials with $\beta > 2/3$, $f(x = 0)$ can tend to zero slowly as $v_\parallel$ decreases ($f(x = 0) \sim {v_\parallel}^{1/2}$); that is, there can be a non-negligible number of particles with slow parallel velocities at $x = 0$. In comparison, in Section 3.2 we will show that this is impossible for $\beta < 2/3$ due to the acceleration by the electric field — particles get to the wall after having been accelerated significantly, and hence there is a negligible number of particles with small $v_\parallel$. We have been unable to prove that our boundary conditions will lead to $f(x = 0) \sim {v_\parallel}^{1/2}$ for $\beta > 2/3$, but physically, for $\beta > 2/3$ one can neglect the electrostatic potential, so we cannot see any reason why particles with small $v_\parallel$ would have not reached the wall. We proceed to show that if particles with small $v_\parallel$ reach the wall, the distribution function needs to satisfy $f(x = 0) \simeq A{v_\parallel}^{1/2}$ for $v_\parallel \to 0$. We also show that $\beta > 2/3$ is incompatible with quasineutrality and a function $f(x = 0)$ that goes to zero like ${v_\parallel}^{1/2}$ for small $v_\parallel$.

The boundary conditions at $\eta \to \pm\infty$ determine which asymptotic solution, (3.14) or (3.18), is correct at $\eta \to +\infty$ and $\eta \to -\infty$,

$$F^{+\infty} \equiv F(\eta \to \infty) = A\eta^{3\Omega} \quad \text{and} \quad F(\eta \to -\infty) = 3N\frac{\exp(\eta^3/9)}{\eta^2}, \tag{3.19}$$

and the distribution function is then

$$f^{+\infty} \equiv f(\eta \to \infty) = Av_\parallel^{3\Omega} \quad \text{and} \quad f(\eta \to -\infty) = 3N\frac{(D_0 x)^{\Omega+2/3}}{v_\parallel^2}\exp\left(\frac{v_\parallel^3}{9x}\right), \tag{3.20}$$

where we have introduced $F^{+\infty}$ and $f^{+\infty}$ to simplify notation, as these functions will be used later.

Equation (3.12) can be solved analytically in terms of Kummer confluent hypergeometric functions $M(a; b; \eta)$, and can be shown to give $\Omega = 1/6$ if we want F (and hence f) to be positive. This is done in Appendix E.2, where we find the full solution to equation (3.12) to be

$$F(\eta) = \bar{R}\Big(- \frac{12^{1/3}\sqrt{\pi}}{\Gamma[-1/6]}\eta M(1/6; 4/3; \eta^3/9) + M(-1/6; 2/3; \eta^3/9)\Big). \tag{3.21}$$

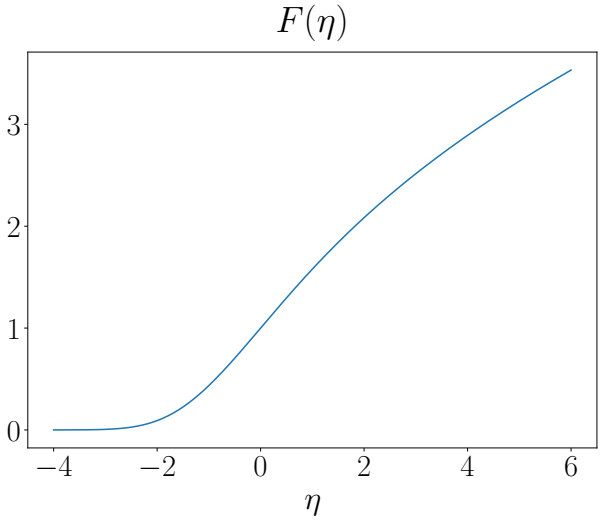

Figure 3.1: The blue line is function $F(\eta)$ for $\bar{R} = 1$. The continuity of F and its first derivative are imposed at $\eta = 0$. Plotted is the only function that solves the differential equation (3.12), satisfies the boundary conditions and has $F > 0$ everywhere. We know that $\bar{R} > 0$, but to determine the actual value of $\bar{R}$, we would need a boundary condition associated with the distribution function at large $v_\parallel$ and x, where our approximations used to derive (3.12) break down.

Here, to ensure $F > 0$, $\bar{R}$ is a positive constant, and $\Gamma[x]$ is the Gamma function. The function for $\bar{R} = 1$ is given in Figure 3.1. To determine the value of $\bar{R}$, we would need to solve the drift kinetic equation at large $v_\parallel$ and x, where the approximations used to derive (3.12) break down. We do not do this in this thesis. In the next section we show that solution (3.21) is inconsistent with the quasineutrality equation.

3.1.2 Proving $\beta \leq 2/3$

We expand the quasineutrality equation with adiabatic electrons (3.4) to first order in $\hat{\phi}$, using $\hat{\phi} \sim x^\beta \ll 1$. The density is $n \simeq n(x=0)(1 + \hat{\phi}/T_e + O(\hat{\phi}^2))$, where $n(x=0) = \int d^3\mathbf{v} f(x=0)$. This gives

$$\frac{\hat{\phi}}{T_e} n(x=0) = \int_{v_\parallel<0} f d^3\mathbf{v} + \int_{0<v_\parallel\leq K(D_0x)^{1/3}} f d^3\mathbf{v} + \int_{v_\parallel>K(D_0x)^{1/3}} f d^3\mathbf{v} - \int_{v_\parallel>0} f(x=0) d^3\mathbf{v}. \tag{3.22}$$

The integral is split into regions where different approximations are valid. The constant K is chosen such that $1 \ll K \ll x^{-1/3}$ so that eventually we can take the limits $K \to \infty$ and $K(D_0x)^{1/3} \to 0$. For $v_\parallel > K(D_0x)^{1/3}$ our solution (3.21) is not valid, but at large $v_\parallel \gtrsim 1$, we can use expansion (3.8) to approximate the function. In the region $v_\parallel < K(D_0x)^{1/3}$,

our solution (3.21) is valid, as here collisions are well approximated by diffusion in velocity space. The final integral in (3.22), representing the ion density at the wall, is performed only over positive $v_\parallel$ because at the wall the distribution function is zero for negative velocities due to the wall boundary condition. Since $\eta \to \infty$ at $x = 0$, the asymptotic solution (3.19) is exact here; that is, $f(x = 0, v_\perp, v_\parallel \ll 1) = f^{+\infty}$, where the latter was defined in (3.20). The integral can be rewritten in terms of $F(\eta)$ as

$$\begin{aligned}\frac{\hat{\phi}}{T_e}n(x=0) =& x^{1/2}2\pi \int dv_\perp D_0(v_\perp)^{1/2} v_\perp \int_{-\infty}^{0} F d\eta + x^{1/2}2\pi \int dv_\perp D_0(v_\perp)^{1/2} v_\perp \int_0^K F d\eta \\ &+ \int_{v_\parallel > K(D_0x)^{1/3}} \left[\frac{\hat{\phi}}{v_\parallel} \frac{\partial f(x=0)}{\partial v_\parallel} - x \frac{C[f,f](x=0)}{v_\parallel} \right] d^3\mathbf{v} \\ &- \int_{0 \le v_\parallel \le K(D_0x)^{1/3}} f^{+\infty} d^3\mathbf{v}, \end{aligned} \tag{3.23}$$

where we made D_0 dependence on $v_\perp$ explicit for this one equation.

We want to find how these integrals scale with x when we take the limits $K \to \infty$ and $K(D_0x)^{1/3} \to 0$. However, the integral of F diverges as $K \to \infty$ because $F \simeq F^{+\infty} = A\eta^{1/2}$ for large η. Similarly, the integral of $(\partial f(x=0)/\partial v_\parallel)/v_\parallel$ diverges as $K(D_0x)^{1/3} \to 0$ because as $v_\parallel \to K(D_0x)^{1/3}$, the integrand approaches $(\partial f^{+\infty}/\partial v_\parallel)/v_\parallel \sim v_\parallel^{-3/2}$. Near $v_\parallel = (D_0x)^{1/3}$ the collision operator is approximately $D_0 \partial^2 f/\partial v_\parallel^2$ and thus the integral of $C[f,f](x=0)/v_\parallel$ also has a divergence. To avoid the divergence in $\int F d\eta$, we add and subtract the asymptotic behaviour of the solutions for large η to get

$$\begin{aligned}\frac{\hat{\phi}}{T_e}n(x=0) =& x^{1/2}2\pi \int dv_\perp D_0^{1/2} v_\perp \int_{-\infty}^{0} F d\eta + x^{1/2}2\pi \int dv_\perp D_0^{1/2} v_\perp \int_0^K (F - F^{+\infty}) d\eta \\ &+ \hat{\phi} \int_{v_\parallel > K(D_0x)^{1/3}} \frac{1}{v_\parallel} \frac{\partial f(x=0)}{\partial v_\parallel} d^3\mathbf{v} - \int_{v_\parallel > K(D_0x)^{1/3}} x \frac{C[f,f](x=0)}{v_\parallel} d^3\mathbf{v}. \end{aligned} \tag{3.24}$$

We can now take $K \to \infty$. As $\eta \to \infty$ the difference $F - F^{+\infty} \simeq 0.36\bar{R}\eta^{-5/2}$ and thus the second integral on the right hand side of (3.24) converges. In addition, this integral is always positive – this result is derived in Appendix E (equation (E.21)). We do not know the exact value of the derivative $\partial f(x=0)/\partial v_\parallel$ at $v_\parallel \ge 1$, but we expect it to converge at $v_\parallel \to \infty$ and diverge for small $v_\parallel$. The integral of $(1/v_\parallel)(\partial f(x=0)/\partial v_\parallel)$ between $K(D_0x)^{1/3}$ and $+\infty$ will diverge as $\sim 1/\sqrt{K(D_0x)^{1/3}}$ for small x because $f(x = 0) \simeq f_0^{+\infty} \propto v_\parallel^{3/2}$ at small $v_\parallel$. Similarly, the integral of $C[f,f](x=0)/v_\parallel$ diverges as $1/[K(D_0x)^{1/3}]^{3/2}$.

With these estimates, we notice that in equation (3.24),

$$\text{LHS} \sim x^{\beta}, \qquad RHS \sim x^{1/2}, x^{\beta}, \frac{x^{\beta-1/6}}{\sqrt{K}}, \frac{x^{1/2}}{K^{3/2}}. \tag{3.25}$$

The terms $\phi \int (\partial f/\partial v_{\|}) dv_{\|}/v_{\|}$ and $x \int C[f,f](x=0) dv_{\|}/v_{\|}$ in (3.24) are the ones that scale as $x^{\beta-1/6}/\sqrt{K}$ and $x^{1/2}/K^{3/2}$. If one keeps $O(\hat{\phi})$ corrections to our solution for $0 < v_{\|} < K(D_0 x)^{1/3}$, the term proportional to ϕ can be combined with others to obtain a term that is independent of K but still scales as $\hat{\phi}/x^{1/6} \sim x^{\beta-1/6}$. The term that contains the collision operator can be shown to cancel with other terms. For our purposes, the scaling of the terms is sufficient: they are smaller than $x^{1/2}$. As $x \to 0$, the terms with smaller exponents are the largest and the potential on the left side of equation (3.24) cannot balance the terms on the right side unless the terms scaling with $x^{1/2}$ are zero. However the terms $\int_{-\infty}^{0} F d\eta$ and $\int_0^{\infty} (F - F^{+\infty}) d\eta = \int_0^{\infty} 0.36 \bar{R} \eta^{-5/2} d\eta$ are always positive.

Therefore $\beta > 2/3$ is an inconsistent solution to our equations.

3.1.3 Proving $\beta \neq 2/3$

Finally, we consider the case where $\beta = 2/3$. In this case, equation (3.12) no longer holds as the potential term is of the same order as the streaming and diffusion terms. Using $\hat{\phi} = P x^{\beta}$ in equation (3.10) and ansatz $f(x, v_{\perp}, v_{\|}) = (D_0(v_{\perp})x)^{\bar{\Omega}(v_{\perp})} G(\eta)$ (the function $G(\eta)$ is equal to the function $F(\eta)$ given in (3.21) when $P = 0$) gives

$$G'' - \left(\frac{\eta^2}{3} + \frac{2\bar{P}}{3} \right) G' + \bar{\Omega} \eta G = 0, \tag{3.26}$$

where $\bar{P}(v_{\perp}) \equiv P/D_0(v_{\perp})^{2/3}$ is a function of $v_{\perp}$. As explained next $\bar{\Omega}$ must be a function of $v_{\perp}$ as well.

Given $\bar{P}$, a solution to this equation that leads to zero for $\eta \to -\infty$ and diverges algebraically, not exponentially, for $\eta \to \infty$ can be found numerically by choosing an appropriate $\bar{\Omega}$. Note that this dependence of $\bar{\Omega}$ on $\bar{P}$ makes $\bar{\Omega}$ a function of $v_{\perp}$. The pairs of values of $\bar{\Omega}$ and $\bar{P}$ that ensure good behaviour for G do not necessarily satisfy quasineutrality. We already used quasineutrality in Section 3.1.2 to show inconsistencies for different values of $\beta < 2/3$, and we will use it again to show an inconsistency with $\beta = 2/3$. Unlike in the case of Section 3.1.2, where $\bar{P}$ could be neglected, and we were able to find an analytic solution and the exact value of $\Omega = 1/6$, here we need a numerical solution to the equation for any value of $\bar{P} > 0$.

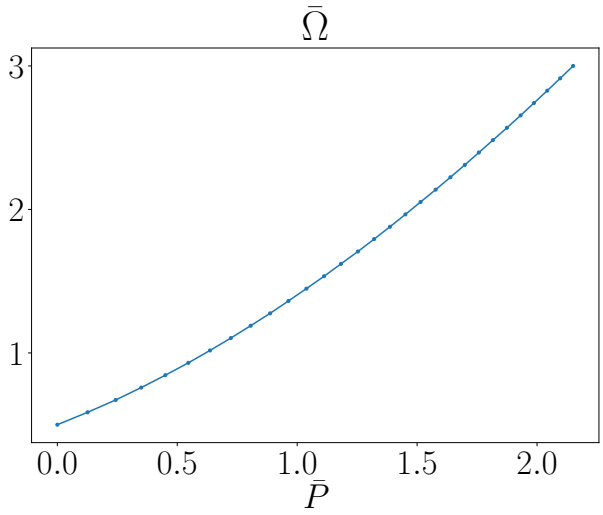

Figure 3.2: Values of $\bar{\Omega}$ that solve equation (3.26) for a given $\bar{P} > 0$.

Given a numerical domain $\eta_{min} < \eta < \eta_{max}$, we solve equation (3.26) numerically by solving it in the regions $\eta_{min} \leq \eta < 0$ and $0 < \eta \leq \eta_{max}$ separately, and looking for solutions where the function and its derivative are continuous at $\eta = 0$. We choose one of the boundary conditions at $\eta = 0$ to be that $dG/d\eta$ is 1, ensuring the derivative's continuity. We then seek for a value of $\bar{\Omega}$ that makes G continuous at $\eta = 0$. This determines G up to a constant. To get the actual value of the derivative at $\eta = 0$, we would need to solve the full drift kinetic equation with full collision operator and the boundary conditions at $x = 0$ and $x \to \infty$. The boundary conditions at η_{max} and η_{min} are that the derivatives $dG/d\eta$ are equal to their asymptotic values (see below for the discussion of the asymptotic limits). We find that for any value $\bar{P} > 0$, $\bar{\Omega} > 1/6$, and $\bar{\Omega}$ grows with increasing $\bar{P}$. Since we expect a monotonically increasing potential, we consider $\bar{P} > 0$ and hence $\bar{\Omega} > 1/6$. Figure 3.2 shows the values of $\bar{\Omega}$ that solve equation (3.26) for a given $\bar{P} > 0$.

Analytically we can find the asymptotic behaviour of the solutions at $\eta \to \infty$ by introducing an expansion $G^{+\infty} = G_0^{+\infty} + G_1^{+\infty} + G_2^{+\infty}...$ where $G_1^{+\infty}/G_0^{+\infty} \sim 1/\eta^2 \ll 1$ and $G_2^{+\infty}/G_0^{+\infty} \sim 1/\eta^3 \ll 1$. To lowest order, we recover equation (3.13), except that here we have $\bar{\Omega}$ instead of Ω. Then, $G_0^{+\infty} = A\eta^{3\bar{\Omega}}$, $g_0^{+\infty} = (D_0 x)^{\bar{\Omega}} G_0^{+\infty} = A v_\parallel^{3\bar{\Omega}}$. We have introduced g for the asymptotic behaviour of f to avoid confusion with the asymptotic results in the previous section. To next order, equation (3.26) is

$$-\frac{\eta^2}{3}(G_1^{+\infty})' - \frac{2\bar{P}}{3}(G_0^{+\infty})' + \bar{\Omega}\eta G_1^{+\infty} = 0. \tag{3.27}$$

Solving this equation gives

$$G_1^{+\infty} = 3\bar{\Omega}A\bar{P}\eta^{3\bar{\Omega}-2}, \qquad g_1^{+\infty} = 3\bar{\Omega}A\hat{\phi}v_\parallel^{3\bar{\Omega}-2} \tag{3.28}$$

and so

$$g_1^{+\infty} = \frac{\hat{\phi}}{v_\parallel}\frac{\partial g_0^{+\infty}}{\partial v_\parallel}. \tag{3.29}$$

Going to second order, (3.26) equation gives

$$(G_0^{+\infty})'' - \frac{\eta^2}{3}(G_2^{+\infty})' + \bar{\Omega}\eta G_2^{+\infty} = 0. \tag{3.30}$$

This gives a solution

$$G_2^{+\infty} = -3\bar{\Omega}(3\bar{\Omega}-1)A\eta^{3\bar{\Omega}-3}, \qquad g_2^{+\infty} = -3\bar{\Omega}(3\bar{\Omega}-1)AD_0xv_\parallel^{3\bar{\Omega}-3} \tag{3.31}$$

and so

$$g_2^{+\infty} = -\frac{x}{v_\parallel}D_0\frac{\partial^2 g_0^{+\infty}}{\partial v_\parallel^2}. \tag{3.32}$$

At $\eta \to -\infty$, the solution is exponentially small and equal to the asymptotic solution $\sim \exp(\eta^3/9)/\eta^3$ (given in (3.19)). For $\eta \to -\infty$, $\bar{P} \neq 0$ is not important.

We will demonstrate that the values of $\bar{P}$ and $\bar{\Omega}$ that solve the kinetic equation for $\hat{\phi} = Px^{2/3}$ are incompatible with quasineutrality, using similar methods to those used in the previous section. Starting with (3.22), using definitions of G above and expansion (3.8) (the collision term is proportional to $x \ll \hat{\phi}$ and is neglected to this order) we get

$$\begin{aligned}\frac{\hat{\phi}}{T_e}n(x=0) =& 2\pi\int_0^\infty dv_\perp v_\perp (D_0x)^{\bar{\Omega}+1/3}\left[\int_{-\infty}^0 G d\eta + \int_0^K (G - G_0^{+\infty})d\eta\right] \\ &+ \int_{v_\parallel > K(D_0x)^{1/3}} \frac{\hat{\phi}}{v_\parallel}\frac{\partial f(x=0)}{\partial v_\parallel}d^3\mathbf{v}.\end{aligned} \tag{3.33}$$

We will now consider different ranges of the minimum value of $\bar{\Omega}(v_\perp)$, $\bar{\Omega}_m \equiv \min_{v_\perp}\bar{\Omega}$, separately.

- $1/6 \leq \bar{\Omega}_m < 1/3$. We follow a procedure similar to the one that led to equation (3.24). In this case $g_1^{+\infty}(\hat{\phi}/v_\parallel)\partial f(x=0)/\partial v_\parallel$ diverges sufficiently fast for small $v_\parallel$, that it is not integrable. To avoid this divergence, we add and subtract integrals of $g_1^{+\infty}$ to equation (3.33). The final result is

$$\begin{aligned}\frac{\hat{\phi}}{T_e}n(x=0) = 2\pi\int_0^\infty dv_\perp v_\perp (D_0x)^{\bar{\Omega}+1/3}&\left[\int_{-\infty}^0 G d\eta + \int_0^K (G - G_0^{+\infty})d\eta\right. \\ &\left. + \int_K^\infty G_1^{+\infty}d\eta\right] + \int_{v_\parallel > K(D_0x)^{1/3}} \frac{\hat{\phi}}{v_\parallel}\left(\frac{\partial f(x=0)}{\partial v_\parallel} - \frac{\partial g_0^{+\infty}}{\partial v_\parallel}\right)d^3\mathbf{v}.\end{aligned} \tag{3.34}$$

In this equation we can take the limits $K \to \infty$ and $K(D_0 x)^{1/3} \to 0$.

To find how the term in the square brackets in equation (3.40) scales with x we need to approximate the integral in $v_\perp$. To do this we rewrite $(D_0 x)^{\bar{\Omega}} = \exp\big(-\bar{\Omega}|\ln(D_0 x)|\big)$, where we made the negative value of $\ln(D_0 x)$ explicit. We then use the fact that $|\ln(D_0 x)| \gg 1$, which allows us to use the Laplace method, because the integral is dominated by the region in $v_\perp$ space where $\bar{\Omega}$ is minimum. This occurs at some $v_\perp = v_{\perp m}$ and we label this minimum value $\bar{\Omega}_m \equiv \bar{\Omega}(v_\perp = v_{\perp m})$.

In our simulations the minimum $\bar{\Omega}_m$ is always a local minimum, that is, $\partial\bar{\Omega}/\partial v_\perp$ vanishes at $v_{\perp m}$. This can be confirmed by using (E.5), applying the relation $\bar{\Omega} \propto 1/D_0$, and evaluating D_0 numerically at $x = 0$ and $v_\parallel = 0$. Numerical calculations are shown in Figure 3.3, where $D_{0m} \equiv \max_{v_\perp} \bar{D}_0$ is always a local maximum. Expanding $\bar{\Omega}$ around its minimum it to second order in $v_\perp - v_{\perp m}$, we get

$$\bar{\Omega}(v_\perp) = \bar{\Omega}_m + \frac{1}{2}(v_\perp - v_{\perp m})^2 \bar{\Omega}''_m + O((v_\perp - v_{\perp m})^3), \tag{3.35}$$

where we use notation $\bar{\Omega}''_m \equiv \partial^2\bar{\Omega}/\partial v_\perp^2(v_\perp = v_{\perp m})$.

Therefore the integral in $v_\perp$ for any function $L(v_\perp)$, which varies slowly near $v_{\perp m}$, such as in equation (3.40), simplifies to

$$\begin{aligned}
&\int_0^\infty dv_\perp v_\perp (D_{0m}x)^{\bar{\Omega}+1/3} L(v_\perp) \\
&\qquad \simeq (D_{0m}x)^{\bar{\Omega}_m+1/3} v_{\perp m} L(v_{\perp m}) \int_0^\infty dv_\perp \exp\left(-\frac{1}{2}(v_\perp - v_{\perp m})^2 \bar{\Omega}''_m |\ln(D_{0m}x)|\right) \\
&\qquad \simeq L(v_{\perp m}) v_{\perp m} \sqrt{\frac{2\pi}{\bar{\Omega}''_m}} \frac{(D_{0m}x)^{\bar{\Omega}_m+1/3}}{\sqrt{|\ln(D_{0m}x)|}},
\end{aligned} \tag{3.36}$$

where in the last equality we used $\left|\sqrt{\ln(D_{0m}x)}\right| \bar{\Omega}''_m v_{\perp m}^2 \gg 1$. If $\bar{\Omega}_m$ were located at $v_\perp = 0$, then $\partial\bar{\Omega}/\partial v_\perp$ would not need to be zero at the location of the minimum, and the final term in (3.36) would scale as $1/\ln(D_{0m}x)$. The overall argument given in the rest of the section holds independent of the nature of the minimum.

For any value of $\bar{\Omega}_m < 1/3$, in the limit $x \to 0$, the terms in the square brackets of (3.34) dominate the equation and cannot be balanced by the $\hat{\phi} \sim x^{2/3}$ terms, unless the term in the brackets vanishes. The only term in the brackets that may be negative is $\int_0^K d\eta(G - G_0^{+\infty})$. We plot this term for different values of $\bar{\Omega}_m$ in Figure

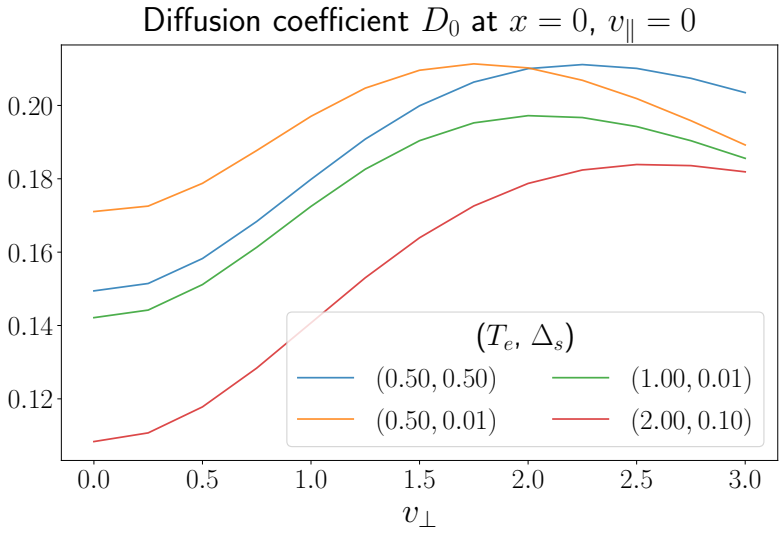

Figure 3.3: The value of $D_0(x = 0, v_\parallel = 0)$ for a sample of simulations.

3.4 to show that it is always positive. These results show that $1/6 \leq \bar{\Omega}_m < 1/3$ is not a valid solution.

- $\bar{\Omega}_m = 1/3$. In this case, the integral of $G_1^{+\infty}$ diverges logarithmically at large η. To show the scaling of all the terms explicitly we split the integral of $(1/v_\parallel)\partial f/\partial v_\parallel$ in (3.33) into two intervals by introducing an intermediate point $b \sim 1$. We then subtract and add the diverging integral in the region $K(D_0 x)^{1/3} \leq v_\parallel \leq b$ explicitly. This gives

$$\frac{\hat{\phi}}{T_e} n(x=0) = v_{\perp m} \sqrt{\frac{2\pi}{\bar{\Omega}_m''}} \frac{(D_{0m}x)^{2/3}}{\sqrt{|\ln(D_{0m}x)|}} \left[\int_{-\infty}^{0} G d\eta + \int_0^K (G - G_0^{+\infty}) d\eta \right]$$
$$+ \int_{K(D_0x)^{1/3} \leq v_\parallel \leq b} \frac{\hat{\phi}}{v_\parallel} \left(\frac{\partial f(x=0)}{\partial v_\parallel} - \frac{\partial g_0^{+\infty}}{\partial v_\parallel} \right) d^3\mathbf{v} + \int_{v_\parallel \geq b} \frac{\hat{\phi}}{v_\parallel} \frac{\partial f(x=0)}{\partial v_\parallel} d^3\mathbf{v}$$
$$+ \int_{1 \leq v_\parallel \leq b} \frac{\hat{\phi}}{v_\parallel} \frac{\partial g_0^{+\infty}}{\partial v_\parallel} d^3\mathbf{v} + \int_{K(D_0x)^{1/3} \leq v_\parallel \leq 1} \frac{\hat{\phi}}{v_\parallel} \frac{\partial g_0^{+\infty}}{\partial v_\parallel} d^3\mathbf{v}, \tag{3.37}$$

where we used Laplace's method to evaluate the $v_\perp$ integral in the first term (the functions in the square brackets are evaluated at $v_{\perp m}$). For the last integral in (3.37), with $g_0^{+\infty} = A(v_\perp) v_\parallel^{3\bar{\Omega}}$, we use the substitution $v_\parallel = e^{-s}$. This avoids the $1/(3\bar{\Omega} - 1)$ prefactor that arises from the $v_\parallel$ integration, which diverges as $\bar{\Omega} \to 1/3$,

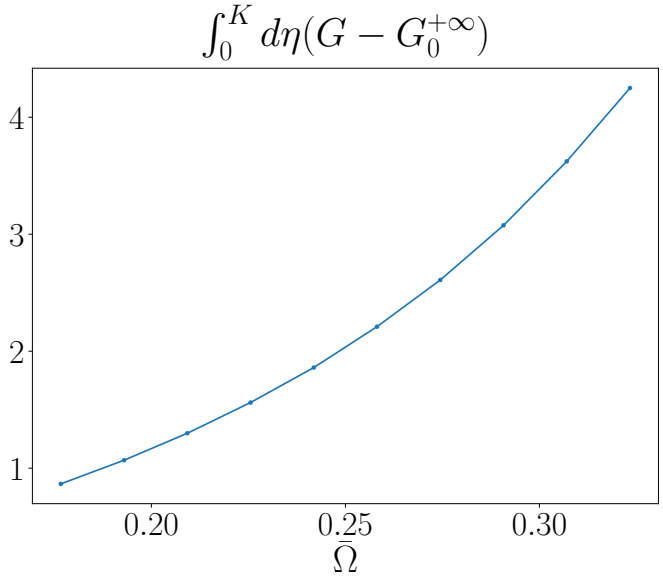

Figure 3.4: The value of $\int_0^K d\eta(G - G_0^{+\infty})$ for $1/6 < \bar{\Omega} < 1/3$, here we take $K = 100$.

and allows the direct application of Laplace's method.

$$\begin{aligned}\int_{K(D_0x)^{1/3}\le v_\parallel\le 1}\frac{\hat{\phi}}{v_\parallel}\frac{\partial g_0^{+\infty}}{\partial v_\parallel}d^3\mathbf{v} &= 6\pi\hat{\phi}\int_0^{\left|\ln\left(K(D_0x)^{1/3}\right)\right|}ds\int_0^\infty dv_\perp v_\perp A\bar{\Omega}e^{-s(3\bar{\Omega}-1)}\\ &\simeq 2\pi\hat{\phi}v_{\perp m}A_m\sqrt{\frac{2\pi}{3\bar{\Omega}_m''}}\int_0^{\left|\ln\left(K(D_0x)^{1/3}\right)\right|}ds\frac{1}{\sqrt{s}}\\ &= 4\pi\hat{\phi}\sqrt{\left|\ln(K(D_{0m}x)^{1/3})\right|}\sqrt{\frac{2\pi}{3\bar{\Omega}_m''}}v_{\perp m}A_m, \qquad (3.38)\end{aligned}$$

where $A_m \equiv A(v_{\perp m})$ and for the second equality we used Laplace's method to approximate the $v_\perp$ integral, it is valid because the integral in s is dominated by the region of $s \sim \left|\ln\left(K\left(D_0x\right)^{1/3}\right)\right| \gg 1$.

We can now take the limit $K(D_0x)^{1/3} \to 0$ in the integral from $K(D_0x)^{1/3}$ to b without encountering any divergences. The subtracted divergence is explicit in the last term. All the terms in (3.37) are too small to balance the dominant term $\hat{\phi}\sqrt{|\ln(K(D_{0m}x)^{1/3})|}$ in (3.37) for small x, making this solution invalid.

- $1/3 < \bar{\Omega}_m < 2/3$.

  In this case, the integral of $(\hat{\phi}/v_\parallel)(\partial f(x=0)/\partial v_\parallel)$ is integrable for small $v_\parallel$. However, integral of G now has divergence at large η, which needs to be eliminated by subtracting $G_1^{+\infty}(\eta)$ before taking $K \to \infty$. The function $G_1^{+\infty}(\eta)$ is added back as

$(\hat{\phi}/v_\parallel)(\partial f(x=0)/\partial v_\parallel)$. We rewrite quasineutrality as

$$\frac{\hat{\phi}}{T_e}n(x=0) = 2\pi\int_0^\infty dv_\perp v_\perp (D_0 x)^{\bar{\Omega}+1/3}\left[\int_{-\infty}^0 G d\eta + \int_0^K (G - G_0^{+\infty} - G_1^{+\infty})d\eta\right] + \int_{v_\parallel > K(D_0x)^{1/3}} \frac{\hat{\phi}}{v_\parallel}\frac{\partial f(x=0)}{\partial v_\parallel}d^3\mathbf{v} + \int_{0<v_\parallel\le K(D_0x)^{1/3}} \frac{\hat{\phi}}{v_\parallel}\frac{\partial g_0^{+\infty}}{\partial v_\parallel}d^3\mathbf{v}. \quad (3.39)$$

We integrate the first term in $v_\perp$ and use $f(x=0) \simeq g_0^{+\infty}$ to bring the last two integrals together and get

$$\frac{\hat{\phi}}{T_e}n(x=0) = v_{\perp m}\sqrt{\frac{2\pi}{\bar{\Omega}_m''}}\frac{(D_{0m}x)^{\bar{\Omega}_m+1/3}}{\sqrt{|\ln(D_{0m}x)|}}\left[\int_{-\infty}^0 G d\eta + \int_0^K (G - G_0^{+\infty} - G_1^{+\infty})d\eta\right] + \int \frac{\hat{\phi}}{v_\parallel}\frac{\partial f(x=0)}{\partial v_\parallel}d^3\mathbf{v}. \quad (3.40)$$

Since $\bar{\Omega}_m > 1/3$, the potential terms, which scale as $x^{2/3}$, dominate and the equation looks balanced, simplifying to

$$\frac{\hat{\phi}}{T_e}n(x=0) \simeq \int \frac{\hat{\phi}}{v_\parallel}\frac{\partial f(x=0)}{\partial v_\parallel}d^3\mathbf{v}. \quad (3.41)$$

This is exactly the kinetic Chodura condition (3.5), which has to be satisfied at the sheath boundary. To find if the $x^{2/3}$ scaling of the potential is consistent, we need to go to higher order in x and $\hat{\phi}$ in the quasineutrality equation (3.39).

The left hand side of quasineutrality (3.4) gives terms of order $\hat{\phi}^2$ from the density expansion

$$n(x) \simeq n(x=0)(1 + \hat{\phi}/T_e + \hat{\phi}^2/2T_e^2 + O(\hat{\phi}^3/T_e^3)). \quad (3.42)$$

On the right side, we keep the higher order terms of the expansion (3.8) to get an equation

$$\frac{n(x=0)}{2T_e^2}\hat{\phi}^2 = v_{\perp m}\sqrt{\frac{2\pi}{\bar{\Omega}_m''}}\frac{(D_{0m}x)^{\bar{\Omega}_m+1/3}}{\sqrt{|\ln(D_{0m}x)|}}\left[\int_{-\infty}^0 G d\eta + \int_0^K (G - G_0^{+\infty} - G_1^{+\infty})d\eta\right] - x\int_{v_\parallel > K(D_0x)^{1/3}} \frac{1}{v_\parallel}C[f,f](x=0)d^3\mathbf{v}. \quad (3.43)$$

At small $v_\parallel$, $C[f,f](x=0) = D_0\partial^2 f(x=0)/\partial v_\parallel^2$, it diverges because $\partial^2 g_0^{+\infty}/\partial v_\parallel^2 \sim v_\parallel^{3\bar{\Omega}-2}$. We subtract the divergence and add it to the terms in the brackets to get

$$\frac{n(x=0)}{2T_e^2}\hat{\phi}^2 = -x\int_{v_\parallel > K(D_0x)^{1/3}} \frac{1}{v_\parallel}\left(C[f,f](x=0) - D_0\frac{\partial^2 g_0^{+\infty}}{\partial v_\parallel^2}\right)d^3\mathbf{v} + v_{\perp m}\sqrt{\frac{2\pi}{\bar{\Omega}_m''}}\frac{(D_{0m}x)^{\bar{\Omega}_m+1/3}}{\sqrt{|\ln(D_{0m}x)|}}\left[\int_{-\infty}^0 G d\eta + \int_0^K (G - G_0^{+\infty} - G_1^{+\infty})d\eta + \int_K^\infty G_2^{+\infty}d\eta\right]. \quad (3.44)$$

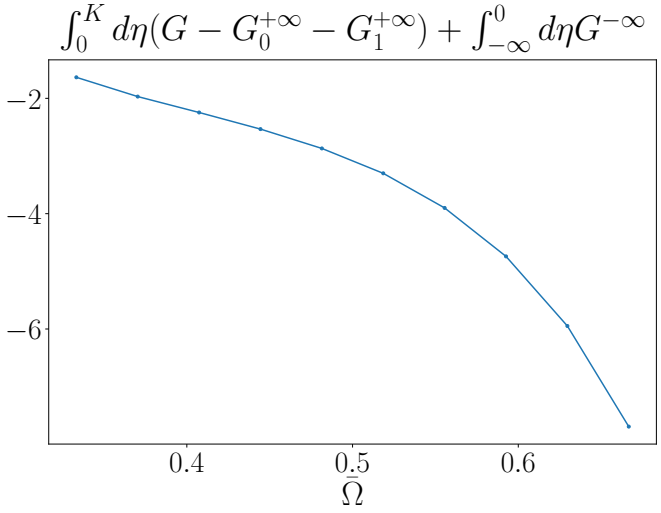

Figure 3.5: The value of $\int_0^K d\eta(G - G_0^{+\infty} - G_1^{+\infty}) + \int_{-\infty}^0 d\eta G^{-\infty}$ for $1/3 < \bar{\Omega} < 2/3$, here we take $K = 100$.

The limits $K \to \infty$ and $K(D_0 x)^{1/3} \to 0$ can now be taken. Comparing the scalings of the three terms we have $x^{4/3}$, x and $x^{\bar{\Omega}_m + 1/3}/\sqrt{|\ln(D_{0m}x)|}$. The latter two terms are dominant, and they cannot be balanced for all $D_{0m}x \ll 1$. Therefore no solutions exist if the term in square brackets is not zero. For $K \to \infty$ the term $\int_0^\infty d\eta(G - G_0^{+\infty} - G_1^{+\infty}) + \int_{-\infty}^0 d\eta G^{-\infty}$ is never zero in the range $1/3 < \bar{\Omega}_m < 2/3$ (see Figure 3.5), making $1/3 < \bar{\Omega}_m < 2/3$ an invalid solution.

- $\bar{\Omega}_m = 2/3$.

  In this case, the integral of $G_2^{+\infty}$ diverges logarithmically at large η, therefore to deal with the divergence of $C/v_\parallel$ term we have to introduce an intermediate point $b \sim 1$ and use the substitution $v_\parallel = e^{-s}$ like we did for the $\bar{\Omega} = 1/3$ case. Equation (3.43) then simplifies to

$$\begin{aligned}
&\frac{n(x=0)}{2T_e^2}\hat{\phi}^2 = -x\int_{K(D_0x)^{1/3}\le v_\parallel \le b} \frac{1}{v_\parallel}\left(C[f,f](x=0) - D_0\frac{\partial^2 g_0^{+\infty}}{\partial v_\parallel^2}\right)d^3\mathbf{v} \\
&- x\int_{v_\parallel \ge b}\frac{1}{v_\parallel}C[f,f](x=0)d^3\mathbf{v} - x\int_{1\le v_\parallel\le b}\frac{1}{v_\parallel}D_0\frac{\partial^2 g_0^{+\infty}}{\partial v_\parallel^2}d^3\mathbf{v} \\
&- 8\pi D_{0m}x\sqrt{|\ln(K(D_{0m}x)^{1/3})|}\sqrt{\frac{2\pi}{3\bar{\Omega}_m''}}v_{\perp m}A_m \\
&+ v_{\perp m}\sqrt{\frac{2\pi}{\bar{\Omega}_m''}}\frac{(D_{0m}x)}{\sqrt{|\ln(D_{0m}x)|}}\left[\int_{-\infty}^0 G d\eta + \int_0^K (G - G_0^{+\infty} - G_1^{+\infty})d\eta\right]. \qquad (3.45)
\end{aligned}$$

We can now take the limit $K(D_0x)^{1/3} \to 0$ in the integral of $C/v_\parallel$. The term $x\sqrt{|\ln(K(D_{0m}x)^{1/3})|}$ at small x dominates other terms, making this solution invalid.

- $\bar{\Omega}_m > 2/3$.

  To lowest order the potential terms balance in the quasineutrality equation to give (3.41) and we use (3.43). At large η there is a divergence in $G(\eta)$ for $\eta \to \infty$ since $G_2(\eta)$ diverges and it has to be subtracted. Equation (3.43) then gives

$$\begin{aligned}\frac{n(x=0)}{2T_e^2}\hat{\phi}^2 = &-x\int_{v_\parallel > K(D_0x)^{1/3}} \frac{1}{v_\parallel} C[f,f](x=0)d^3\mathbf{v} \\ &-x\int_{v_\parallel \leq K(D_0x)^{1/3}} \frac{1}{v_\parallel} D_0 \frac{\partial^2 g_0^{+\infty}}{\partial v_\parallel^2} d^3\mathbf{v} \\ &+v_{\perp m}\sqrt{\frac{2\pi}{\bar{\Omega}_m''}}\frac{(D_{0m}x)^{\bar{\Omega}_m+1/3}}{\sqrt{|\ln(D_{0m}x)|}}\left[\int_{-\infty}^{0} G d\eta + \int_0^K (G - G_0^{+\infty} - G_1^{+\infty} - G_2^{\infty})d\eta\right].\end{aligned} \tag{3.46}$$

  The first two terms on the right hand side add up to eliminate $K(D_0x)^{1/3}$ from the expansion. $K \to \infty$ can now be taken without divergences. In the limit $x \to 0$ the right hand side is dominated by $x\int C[f,f](x=0)/v_\parallel$. This term scales as $x \gg \hat{\phi}^2 \sim x^{4/3}$ and cannot be balanced by any other terms. Any values of $\bar{\Omega}_m$ larger than $2/3$ will result in terms smaller than x.

Thus there are no valid solutions for $\beta = 2/3$, combined with the previous proof that $\beta > 2/3$ is not allowed, we must have $\beta < 2/3$ for solutions to exist.

3.2 Deriving the $\hat{\phi} \sim x^{1/2}$ scaling

We have argued that the electric field diverges at $x = 0$ since $\beta < 2/3$ and $\partial\hat{\phi}\partial x \sim x^{\beta-1}$. In this section we show that the distribution function is exponentially small near the wall at small velocities. We use this result to get the scaling $\hat{\phi} \sim x^{1/2}$ and to prove that the kinetic Chodura condition is satisfied at $x = 0$. Throughout this section, we continue using normalised variables unless explicitly stated otherwise.

3.2.1 Exponentially small distribution function near the wall at small $v_\parallel$

The full drift kinetic equation is given in (3.3). At the MPE, at $v_\parallel \sim 1$ the function is smooth and the collision operator, which contains derivatives of f in $v_\parallel$ and no derivatives in x, is finite. However, as mentioned in the previous section, we expect solutions that have $\beta < 2/3$, which results in a diverging electric field as $x \to 0$. Therefore, to balance the diverging electric field at $x = 0$ in (3.3), the parallel streaming term $v_\parallel \partial f/\partial x$ must diverge as well. This balance must occur even for $v_\parallel \ll 1$ since, from scalings (3.9), near the MPE ($x \ll 1$) the collision term will be negligible compared to the electric field term for $v_\parallel \gg x^{1-\beta}$. We also see from (3.9) that for velocities $v_\parallel \sim \sqrt{\hat{\phi}} \sim x^{\beta/2}$ the potential term causes a large change in f. We are interested in the characteristics where this change is large, but collisions can be neglected, that is, $x^{\beta/2} \sim v_\parallel \gg x^{1-\beta}$. Notice that this inequality can only be satisfied for $x \ll 1$ if $\beta < 2/3$. We define the expansion parameter $\eta \sim x^{1-\beta}/v_\parallel \ll 1$ and write our distribution function near $x = 0$ and $v_\parallel = 0$ as

$$f = f_0 + \eta f_1 + \eta f_2 + ... \tag{3.47}$$

Then using the fact that $C[f_0, f_0] \sim \eta v_\parallel \partial f_0/\partial x \sim \eta(\partial\hat{\phi}/\partial x)(\partial f_0/\partial v_\parallel)$, to lowest order, we have

$$-v_\parallel \frac{\partial f_0}{\partial x} + \frac{\partial \hat{\phi}}{\partial x}\frac{\partial f_0}{\partial v_\parallel} = 0. \tag{3.48}$$

The solution to this equation is $f_0 = f_0(U)$. This says that the distribution function remains constant along the trajectories defined by constant energy. Since the wall is fully absorbing, we have the boundary condition $f(x = 0, v_\parallel < 0) = 0$. As a result, all the particle trajectories that come from the MPE have $f = 0$. In Figure 3.6 we show the trajectories of the particles calculated numerically using the numerical model described in Chapter 4.

Figure 3.6 shows that all particle trajectories at $x = 0$ and small enough $v_\parallel > 0$ come from the MPE. For these trajectories, the time between leaving the wall and reaching it again is short enough so that the collisions can be neglected to lowest order, as argued above, and as a result, $f_0(x = 0, v_\parallel) = 0$. Then f_0 and its derivatives are also zero at small $v_\parallel$ and so $C[f_0, f](x = 0, v_\parallel) = 0$. Note that by writing the collision operator

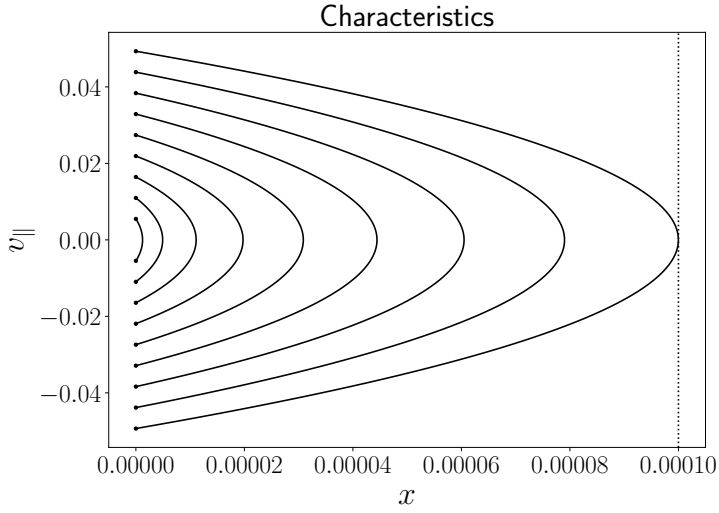

Figure 3.6: Particle trajectories near the MPE. The points at $x = 0$ and $v_\parallel > 0$ are the final locations of the trajectories. The code starts at these locations and traces the paths back in time to the next grid point in x. Trajectories shown above do not reach the next grid point in x (dotted vertical line), they originate from $x = 0$.

as $C[f_0, f]$ we are emphasising that it enters in the operator both differentiated (first argument of $C[f_0, f]$) and inside velocity space integrals (second argument of $C[f_0, f]$), and that we are using the approximation only for the terms that are not in the integrals, where approximation would not be valid as it requires the values of f at all $v_\parallel$. Going to next order in η, we have

$$-v_\parallel \frac{\partial f_1}{\partial x} + \frac{\partial \hat{\phi}}{\partial x}\frac{\partial f_1}{\partial v_\parallel} = C[f_0, f], \tag{3.49}$$

but, as argued above, at small $v_\parallel$, we have $f_0 = 0$ and hence $C[f_0, f] = 0$. Then the equation for f_1 looks the same as the equation for f_0. The solution is $f_1(x = 0, v_\parallel) = 0$. We can repeat this process to an arbitrary order in η and thus show $f_n(x = 0, v_\parallel) = 0$ for any n. This means that $f(x = 0, v_\parallel)$ is exponentially small in η, that is, $f(x = 0) \sim \exp(-A/\eta^p)$, where A and $p > 0$ are some constants that we have not determined. Note that our small expansion parameter η only gives a relation between $v_\parallel$ and x, and since $v_\parallel \sim x^{\beta/2}$, it can be written as various combinations of x and $v_\parallel$, and therefore this calculation does not tell us the precise dependence of f on x and $v_\parallel$ in this region.

3.2.2 Chodura Condition

We can now derive the kinetic Chodura condition. We start by differentiating the quasineutrality equation (3.4), which gives

$$\frac{\partial n}{\partial x} = \frac{n}{T_e}\frac{\partial \hat{\phi}}{\partial x}, \tag{3.50}$$

For the left hand side, we use $n = \int d^3\boldsymbol{v} f$ and rearrange the drift kinetic equation (3.3) to get

$$\frac{\partial f}{\partial x} = \frac{\partial \hat{\phi}}{\partial x}\frac{1}{v_\parallel}\frac{\partial f}{\partial v_\parallel} - \frac{C[f,f]}{v_\parallel}. \tag{3.51}$$

Substituting this result into (3.50) and rearranging gives us

$$\left\{ \fint d^3\boldsymbol{v}\frac{1}{v_\parallel}\frac{\partial f}{\partial v_\parallel} - \frac{n}{T_e}\right\}\frac{\partial \hat{\phi}}{\partial x} = \fint d^3\boldsymbol{v}\frac{C[f,f]}{v_\parallel}, \tag{3.52}$$

where $\fint$ indicates that these are principal value integrals. The principal value is needed to make sure that the two principal value integrals add appropriately and do not introduce any divergences that were not present in the original equation (3.51).

Since f is exponentially small for small $v_\parallel$ and small x, the right hand side of (3.52) s finite at $x = 0$, whereas we have showed that the electric field diverges at $x = 0$. Therefore, at $x = 0$, the term in the brackets in the left hand side of (3.52) must be zero. In addition, due to the function being exponentially small at small $v_\parallel$ at $x = 0$, we can remove the principal value from the integral as we know it does not diverge at $v_\parallel = 0$ and $x = 0$. This gives

$$\int d^3\boldsymbol{v}\frac{1}{v_\parallel}\frac{\partial f(x=0)}{\partial v_\parallel} = \frac{n(x=0)}{T_e}. \tag{3.53}$$

Integrating by parts and using $f = 0$ for $v_\parallel = 0$ and $x = 0$, and for $v_\parallel \to \infty$, we recover the kinetic Chodura condition (3.5).

The derivation relies on the electric field diverging at $x = 0$ and on the distribution function at $x = 0$ decaying to zero quickly enough at small $v_\parallel > 0$ for the integrals in (3.52) to be finite. The fact that the kinetic Chodura condition is satisfied at $x = 0$ allows us to label this point as the MPE, where we know from the magnetic presheath analysis [37] that the kinetic Chodura condition must be satisfied for the potential in the magnetic presheath to be monotonic. Note that the electric field diverges on the collisional layer scale but it is finite on the magnetic presheath scale since $\lambda_{MFP}\sin\alpha \gg \rho_i$.

3.2.3 Scaling of $\hat{\phi}$ with x

We can find how $\hat{\phi}$ depends on x by expanding equation (3.52) for $\hat{\phi} \ll 1$, which happens for small x. Due to exponential decay of $f(x=0)$ for small $v_\parallel$, expression (3.8) is valid for all $v_\parallel$, giving

$$f - f(x=0) = \frac{\hat{\phi}}{v_\parallel}\frac{\partial f(x=0)}{\partial v_\parallel} + O(\hat{\phi}^2, x). \tag{3.54}$$

where we have used that the terms of $O(x)$ are higher order since the potential scales as $\hat{\phi} \propto x^\beta$, with $\beta < 2/3$. Plugging equation (3.54) into equation (3.52), expanding $n(x) \simeq n(x=0)(1+\hat{\phi})$ (recall the electron adiabatic response), and using the kinetic Chodura condition (3.5) to cancel out the lowest order terms give

$$\left\{ \int d^3\boldsymbol{v}\, \frac{1}{v_\parallel}\frac{\partial}{\partial v_\parallel}\left(\frac{1}{v_\parallel}\frac{\partial f(x=0)}{\partial v_\parallel}\right) - n \right\} \hat{\phi}\frac{\partial \hat{\phi}}{\partial x} = \int d^3\boldsymbol{v}\, \frac{C[f,f](x=0)}{v_\parallel} + O(\hat{\phi}). \tag{3.55}$$

Then integrating by parts in $v_\parallel$,

$$\left\{ \int d^3\boldsymbol{v}\, \frac{3f(x=0)}{v_\parallel^4} - n \right\} \hat{\phi}\frac{\partial \hat{\phi}}{\partial x} = \int d^3\boldsymbol{v}\, \frac{C[f,f](x=0)}{v_\parallel} + O(\hat{\phi}). \tag{3.56}$$

Once again, the integrals do not diverge because $f(x=0)$ is exponentially small for small $v_\parallel$. The right hand side of (3.56) is a constant to lowest order. This gives us

$$\hat{\phi}\frac{\partial \hat{\phi}}{\partial x} = A, \tag{3.57}$$

where A is a constant. From (3.57) it follows that at $x=0$, the MPE, $\hat{\phi} \sim x^{1/2}$. This is consistent with $\beta < 2/3$. This means that we have found a self consistent solution. This solution relies on a diverging potential and the distribution function decaying to zero quickly enough as $v_\parallel \to 0$ so that all the integrals are well defined.

Reference [40] showed that the potential scales as $\hat{\phi} \sim x^{2/3}$ for a source of particles that has a finite non-zero value at $v_\parallel = 0$. There it was assumed that the source and the distribution function behave as a power of $v_\parallel$ for small $v_\parallel$ near $x=0$, whereas we have shown that both the distribution function and the source (in this case, the collision operator) are exponentially small. There exists no source of particles due to collisions at $v_\parallel = 0$ in our problem because the characteristics with small positive $v_\parallel$ near the MPE are connected to a negative $v_\parallel$ at the MPE, where the boundary condition imposes that $f = 0$. The collisions, which allow the particles to jump from one characteristic to another and in this way give $f(v_\parallel > 0) > 0$, are proportional to f itself, and as a result fill the small $v_\parallel > 0$ with an exponentially small distribution function.

Chapter 4

Numerical methods

In this chapter we describe the numerical method we use to solve the steady state drift kinetic equation together with quasineutrality assuming Boltzmann electrons. In normalised variables these are equations (3.3) and (3.4). We use a finite element basis to describe the distribution function in velocity space and Galerkin's method to get a system of equations for the weights of the basis functions, which can be solved numerically. We follow the characteristics determined by the left hand side of the equation using a first order Euler method and evaluate the collision operator implicitly. The nonlinear equations obtained through these discretisations are solved using Newton's method. Throughout this chapter, we use normalised variables, introduced in (2.54).

In Section 4.1 we describe the semi-Lagrangian implementation of the left hand side of the drift kinetic equation. In Section 4.2 we introduce Galerkin's method and convert the system of equations into a discrete set of nonlinear equations we can solve numerically, and we introduce the velocity space grids. In Section 4.3 we describe the form that the Fokker-Planck collision operator takes in the basis functions chosen, prove its conservation properties and discuss entropy production. In Section 4.4 we introduce Newton's method and its implementation, and we discuss the position space grid.

4.1 Time evolution

We are solving for the steady state of the system. The left hand side of equation (3.3) can be described as a derivative along characteristics. Using characteristics to discretise the equation ensures stability of the numerical method. The derivative is approximated

with the first order Euler method, and so the left hand side of (3.3) becomes

$$\frac{\mathrm{d}f}{\mathrm{d}t} \simeq \frac{1}{\Delta t(x(t), v_\parallel(t))}\Big[f(x(t), v_\parallel(t), v_\perp(t)) - f(x(t-\Delta t), v_\parallel(t-\Delta t), v_\perp(t-\Delta t))\Big]. \quad (4.1)$$

We divide the x-space into a grid, where each grid point is x_i, with $i = 0, ..., N_x - 1$. Here N_x is the number of grid points in the system, x_0 corresponds to the MPE and x_{N_x-1} to the boundary at $x \to \infty$. We choose the MPE to be the origin of the coordinate system, and $x_0 = 0$. The distance between two points in x is, in general, not uniform and labelled $\Delta x_i = x_{i+1} - x_i$. We interpolate the potential in x linearly in between the grid points, except in the region between x_0 (the MPE) and x_1, where we fix the potential to vary as $\sqrt{x}$. This is justified by the analysis done in Section 3.2.3, where we obtained equation (3.57). We have to force the potential to be $\sqrt{x}$ to correctly capture the behaviour of the distribution function in that region. We discuss this choice further in Section 5.4.

At each time step, we take $x(t) = x_i$. For velocity space, we choose $v_\parallel(t)$ to be the Gaussian quadrature points inside specific intervals because we will use Gaussian quadrature for our velocity space integration (the Gaussian quadrature integration method will be discussed in Section 4.2.1). We follow the characteristics of every x_i and $v_\parallel(t)$ back in time to $t - \Delta t$. The time interval Δt is the time it takes the particle to intersect a grid point in x once again, so $x(t - \Delta t) = x_k$, where k can be $i - 1, i$ or $i + 1$. The index k depends on $v_\parallel(t)$ and the electric field in the region. Note that the time step is different for every $x(t)$ and $v_\parallel(t)$. The collisionless trajectories of the particles are presented in Figure 4.1, where the dots represent the values of x and $v_\parallel$ at every Δt along the trajectory.

Given $x(t), v_\parallel(t)$ and $\phi(x)$, we can solve for $\Delta t, x(t-\Delta t)$ and $v(t-\Delta t)$. From equation (3.3) the equations for the characteristics are

$$\frac{\mathrm{d}x}{\mathrm{d}t} = -v_\parallel, \qquad \frac{\mathrm{d}v_\parallel}{\mathrm{d}t} = \frac{\partial \phi}{\partial x}, \qquad \frac{\mathrm{d}v_\perp}{\mathrm{d}t} = 0. \quad (4.2)$$

Thus, $v_\perp$ is constant along the characteristic, as it should be for a particle in a uniform magnetic field in the drift kinetic approximation.

To simplify notation, we introduce the functions

$$\zeta \equiv v_\parallel(t - \Delta t) \qquad \text{and} \qquad \xi \equiv x(t - \Delta t). \quad (4.3)$$

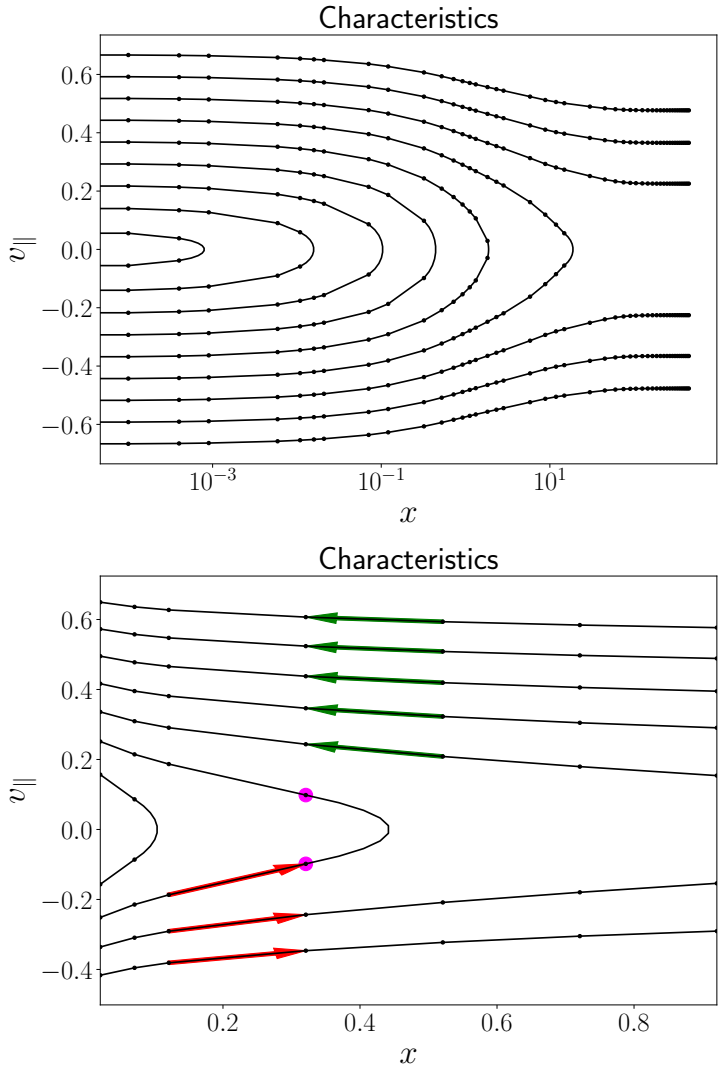

Figure 4.1: The particle trajectories (black dashed lines) in phase space for a negatively charged wall for a simulation with $\Delta_s = 0.1$ and $T_e = 0.5$. The spatial point $x = 0$ (the MPE), and $v_\parallel$ is the velocity along the magnetic field line (positive towards the wall). Only the lines for a small subset of $v_\parallel$ velocities used in the simulations are drawn. **Top:** Trajectories for the entire position space domain. Trajectories are followed back from the boundaries ($x = 0$, $v_\parallel > 0$, and $x = x_{N_x-1}$, $v_\parallel < 0$). The black dots are $x(t), v_\parallel(t)$ points that we evolve to find $x(t - \Delta t), v_\parallel(t - \Delta t)$. Here $x(t - \Delta t)$ is the first grid point the trajectory intersects when following it back in time. Only trajectories that escape from the MPE and reach the boundary x_{N_x-1} are the trajectories associated with the largest $|v_\parallel|$ ($v_\parallel < 0$). The rest of the trajectories from the MPE turn around and travel back to the MPE. **Bottom:** Zoomed in part of the position space domain. The red arrows represent the trajectories of particles moving away from the wall that have enough energy to overcome the electric field and reach the next grid point. The larger magenta dots represent a trajectory of a slower particle. This trajectory starts at the lower magenta point with $v_\parallel(t - \Delta t) < 0$. t his velocity is not large enough to overcome the potential barrier and reach the next grid point, and as a result the trajectory turns back and ends at the same location in space ($x(t) = x(t - \Delta t)$), and $v_\parallel(t) = -v_\parallel(t - \Delta t)$. The green arrows represent particles already moving towards the wall, being accelerated by the electric field. Note that Δt is different for each trajectory.

From conservation of energy, we have

$$\zeta^2 + 2\phi(\xi) = v_\parallel^2(t) + 2\phi(x_i), \tag{4.4}$$

where we are looking at a particle that is at an x grid point x_i at time t. Depending on the particle's kinetic energy and the velocity direction $\sigma \equiv sgn(v_\parallel(t))$, ξ is either x_{i-1}, x_i or x_{i+1},

$$\xi = \begin{cases} x_{i+\sigma} & \text{for} \quad v_\parallel^2(t)/2 > \phi(x_{i+\sigma}) - \phi(x_i), \\ x_i & \text{for} \quad v_\parallel^2(t)/2 < \phi(x_{i+\sigma}) - \phi(x_i). \end{cases} \tag{4.5}$$

Then, we use energy conservation (4.4) to find

$$\zeta = \begin{cases} \sigma\sqrt{v_\parallel(t)^2 + 2(\phi(x_i) - \phi(x_{i+\sigma}))} & \text{for} \quad v_\parallel^2(t)/2 > \phi(x_{i+\sigma}) - \phi(x_i), \\ -v_\parallel(t) & \text{for} \quad v_\parallel^2(t)/2 > \phi(x_{i+\sigma}) - \phi(x_i). \end{cases} \tag{4.6}$$

We also have the characteristic equation (4.2) for $v_\parallel$, from which we can find Δt,

$$\Delta t = \int_\zeta^{v_\parallel(t)} \frac{dv'_\parallel}{\partial\phi/\partial x}, \tag{4.7}$$

where we integrate along the particle's trajectory. Note that since $v_\parallel(t)$ are always chosen to be the Gaussian quadrature points (this will be discussed in Section 4.2.1), we will never have $v_\parallel(t) = 0$. We will approximate the potential to be linear in x in between adjacent grid points in x. An exception for the region near the MPE will be discussed later.

We introduce the electric field, which is constant between any two adjacent grid points,

$$\bar{E}_{i,\sigma} = \frac{\partial\phi}{\partial x} = \frac{\phi(x_i) - \phi(x_{i+\sigma})}{\Delta\xi_{i,\sigma}}. \tag{4.8}$$

Equation (4.7) then gives

$$\Delta t(x_i, v_\parallel(t)) = \frac{v_\parallel(t) - \zeta}{\bar{E}_{i,\sigma}}, \tag{4.9}$$

Here we have introduced a variable $\Delta\xi_{i,\sigma} \equiv x_i - x_{i+\sigma}$. The velocity point $v_\parallel(t)$ is chosen to be a point in velocity grid that corresponds to a Gaussian quadrature point. Then variables ξ and ζ are found from (4.5) and (4.6), respectively.

From the analysis in Section 3.2.3, we expect the potential near $x = 0$ to scale as $\hat{\phi} \sim x^{1/2}$, therefore in the region $0 < x < x_1$ we will force the potential to have a $x^{1/2}$ dependence. We will see later (see Section 5.1) that this choice does not affect the potential profile much, but is essential if we want to recover the kinetic Chodura condition

(see Section 4.4.1). A particle that came from the MPE ($x_i = x_1$, $v_\parallel < 0$) or ended up at the MPE ($x_i = x_0$, $v_\parallel > 0$) moves through the region between x_0 and x_1.To find Δt via (4.7), we assume the potential near the wall to be of the form

$$\phi(x) = \phi_0 + \bar{E}_{1,-1} x_1^{1-\beta} x^\beta, \tag{4.10}$$

where ϕ_0 is the potential at the wall and we used (4.8) to define the constant in front of the scaling. Keeping β general is useful to test the code, but in most of our simulations we will set $\beta = 1/2$. Equations (4.7) and (4.9) give

$$\Delta t(x_i, v_\parallel(t)) = \int_\zeta^{v_\parallel(t)} dv'_\parallel \frac{x^{1-\beta}}{\beta \bar{E}_{1,-1} x^{1-\beta}}. \tag{4.11}$$

Then we can use (4.10) and energy conservation $v_\parallel(t)^2 + 2\phi(x_i) = v'^2_\parallel + 2\phi(x)$ to find

$$\Delta t(x_i, v_\parallel(t)) = \frac{1}{2^{1/\beta-1}\beta \bar{E}_{1,-1}^{1/\beta} x_1^{1/\beta-1}} \int_\zeta^{v_\parallel(t)} dv'_\parallel (v_\parallel(t)^2 - v'^2_\parallel + 2(\phi(x_i) - \phi_0))^{1/\beta-1}, \tag{4.12}$$

where $i = 0$ means trajectories are reflected back to the wall before reaching x_1 and have $\zeta = -v_\parallel(t)$, and $i = 1$ refers to trajectories that reach x_1 and hence ζ is found via (4.6). For $\beta = 1/2$ the equation simplifies to

$$\Delta t(x_i, v_\parallel(t)) = \frac{1}{\bar{E}_{i,\sigma}^2 x_1} \left[\frac{2}{3} v_\parallel(t)^3 + \frac{1}{3}\zeta^3 - v_\parallel(t)^2 \zeta + 2(v_\parallel(t) - \zeta) \bar{E}_{1,-1} x_1 \delta_{i1} \right]. \tag{4.13}$$

When the electric field is very small, numerical precision becomes an issue in the evaluation of the above fractions. For values of $\bar{E}_{i,\sigma}$ such that

$$2\frac{\left|\bar{E}_{i,\sigma}\Delta\xi_{i,\sigma}\right|}{v_\parallel(t)^2} < 10^{-7} \tag{4.14}$$

we solve for trajectories by approximating $\bar{E}_{i,\sigma} = 0$. The value 10^{-7} was chosen by evaluating the expression (4.13) for a range of values of the fraction (4.14) and finding that machine precision introduces large errors at values lower than 10^{-7}. This error comes from the specific form of (4.13), throughout the simulations double precision is used. In this zero field case, the time of travel for any trajectory is

$$\Delta t(x_i, v_\parallel) = \frac{\Delta\xi_{i,\sigma}}{v_\parallel}. \tag{4.15}$$

Using the approximations described and equations (4.4), (4.5), (4.9), (4.13) and (4.15), we can determine ζ, ξ and Δt in terms of $x(t)$ and $v_\parallel(t)$ and express equation (4.1) in

terms of these variables. This allows us to evaluate df/dt at every position and velocity space point.

We evaluate the collision operator on the right hand side of (1.19) at the grid point $x(t) = x_i$, which is similar to using a fully implicit scheme in a time stepping algorithm. The full kinetic numerical equation we solve is

$$\frac{1}{\Delta t(x(t), v_\parallel(t))}\Big[f(x(t), v_\parallel(t), v_\perp(t)) - f(\xi, \zeta, v_\perp(t))\Big] = \nabla_v \cdot \mathbf{\Gamma}[f](x(t), v_\parallel(t), v_\perp(t)). \tag{4.16}$$

We use Galerkin's method with a finite element basis in velocity space to turn this into a set of nonlinear equations, and we iterate to a steady state solution using Newton's method.

At the boundaries $x = 0, x_{N_x-1}$, half of the domain in $v_\parallel$ is fixed by the boundary conditions (1.29) and (1.30). Therefore, at those locations only the unfixed half of the distribution function in $v_\parallel$ space ($v_\parallel > 0$ for $x = 0$ and $v_\parallel < 0$ for $x = x_{N_x-1}$) is evolved.

4.2 Galerkin's method

We solve equation (4.16) numerically using Galerkin's finite element method, which we describe here. We look for an approximate solution $\hat{g} = \sum_{i=1}^{N} a_i \psi_i(\boldsymbol{x})$ to the equation $\mathcal{L}[g(\boldsymbol{x})] = 0$, where $\mathcal{L}$ is an operator, $\mathbf{x}$ is an arbitrary variable and $\{\psi_i(\boldsymbol{x})\}_{i=1,..,N}$ are the basis functions spanning some functional vector space W. There are various ways to find the best $\hat{g}$. In Galerkin's method, the idea is to find a set of coefficients $\{a_i\}$ such that the residual of our equation $\mathcal{R} \equiv \mathcal{L}(\hat{g}(\boldsymbol{x}))$ is orthogonal to the space W. Explicitly, this says that for a function ω in W, we require $\int d^n\boldsymbol{x}\mathcal{R}(\boldsymbol{x})\omega(\boldsymbol{x}) = 0$. Since we can expand ω in the basis $\{\psi_i(\boldsymbol{x})\}_{i=1,..,N}$, the condition is equivalent to requiring

$$\int d^n\boldsymbol{x}\mathcal{R}(\boldsymbol{x})\psi_i(\boldsymbol{x}) = 0, \text{ for } i = 1, ..., N. \tag{4.17}$$

This gives us a system of N coupled equations for $\{a_i\}$ that we can solve. Equation (4.17) is a statement of weak equality; that is, $\mathcal{R}(\boldsymbol{x})$ does not have to be zero for all $\boldsymbol{x}$, it only has to be zero when projected onto the basis functions.

For our basis, we use a finite element discretisation. We first discretise $v_\perp$ and $v_\parallel$ into a grid and split the grid into elements, with every element boundary lying on a grid point. The grid points are called nodes. Each element starts at some node and ends at another

node (not necessarily an adjacent one), where the next element starts and so on. The number of nodes inside the element determines the order of the polynomial that we use to interpolate inside the element. In finite element methods, it is common to choose the basis functions to be Lagrange polynomials. If there are n nodes in the element, then the Lagrange polynomials are polynomials of order $n-1$ that are zero at all grid points except one, $\psi_k(x_m) = \delta_{km}$, where x_m is a grid point (a node) and $\psi_k(x)$ is the Lagrange polynomial. The basis function is zero outside the elements that contain node x_k. The location and number of node points can be chosen arbitrarily. The precision of the scheme will differ depending on the points chosen. The choice of Lagrange polynomials (rather than Chebyshev, Legendre, etc.) is motivated by the fact that Lagrange polynomials make it easy to set boundary conditions in a finite integration region. If the element boundary is at node B (at a grid point value x_B), changing the value of the function at x_B only affects the value of the weight a_B, which takes the new value, the other weights are unaffected because $\psi_k(x_B) = \delta_{kB}$. Since at the MPE, the distribution function is zero for negative $v_\parallel$ and finite for positive $v_\parallel$, the choice of Lagrange polynomials makes enforcing the boundary condition very simple. In addition, only the basis functions at the element edges overlap with basis functions in two elements, the other basis functions only overlap with the basis functions inside the same element. This makes it easier to compute the integrals (4.17) and assemble the matrix.

In this work, we use quadratic Lagrange polynomials as our basis functions since this is the lowest order polynomial required to exactly conserve energy (this will be discussed in Section 4.3.2). For quadratic basis functions, the element contains three nodes, two of them are the boundaries of the element and the third one is in the middle of the element. Quadratic basis functions are shown in Figure 4.2. Note that all the basis functions are continuous, but they have discontinuous derivatives at the boundary elements. When solving equation (4.17) and looking for solutions in space W, which is spanned by ψ_i, these discontinuities have to be treated carefully to avoid issues when $\mathcal{R}$ includes second order derivatives of $\hat{g}$.

To summarise, we look for a solution of the distribution function in the space of our

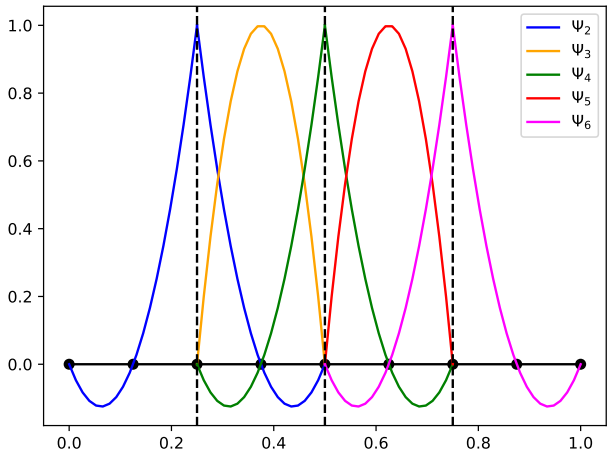

Figure 4.2: Quadratic finite element basis functions for a uniform 1D grid. Each grid point has an associated basis function ψ_k, where k indicates the grid point such that $\psi_k(x_i) = \delta_{ki}$. Dashed lines indicate the boundaries between adjacent elements. In the quadratic case each element has 3 basis functions.

basis functions,

$$\hat{f}(x, v_\perp, v_\parallel) = \sum_{k=1,l=1}^{K,L} a_{kl}(x)\psi_{kl}(v_\perp, v_\parallel). \tag{4.18}$$

From here on we drop the hat and call our numerical solution f. The variables a_{kl} are the weights of the basis functions ψ_{kl} and they depend on x. Indices k and l represent the perpendicular and parallel velocity discretisation, respectively. The numbers K and L are the number of points in our perpendicular and parallel velocity grids, respectively. In this work we choose to use a rectangular grid in the $(v_\perp, v_\parallel)$ space. The velocity grid discretisation will be discussed in Section 4.2.2. Our basis function $\psi_{kl}(v_\perp, v_\parallel)$ is the product of basis functions of one variable, that is, $\psi_{kl}(v_\perp, v_\parallel) = \psi_k(v_\perp)\psi_l(v_\parallel)$, and ψ_k is a quadratic finite element Lagrange polynomial. These are shown in Figure 4.2.

While solution (4.18) does not ensure positivity of the distribution function, this has not caused any issues in the code. To ensure positivity of the distribution function, we initially tried expanding $\ln f$ instead of f in terms of the basis functions, that is, $f = \exp(\sum a_{kl}\psi_{kl})$. This proved to capture the Maxwellian behaviour very well and prevented any numerical imprecisions from causing the function to be negative. However, due to the boundary condition at the wall, which requires the distribution function to be zero at $v_\parallel = 0$, we had to modify the expression for the distribution function there. We

could not find a satisfactory expansion near $v_\parallel = 0$ and $x = 0$. In addition, the exponential expansion made the problem nonlinear, which prevented us from precomputing a collision operator tensor (discussed below) in advance and therefore slowed down the computation by orders of magnitude.

We multiply both sides of equation (4.16) by a basis function $\psi_{kl}(v_\perp, v_\parallel)$ and integrate over the velocity space elements in which the basis function ψ_{kl} is not zero to get

$$\begin{aligned}&\int_{kl} dv_\parallel dv_\perp v_\perp \frac{1}{\Delta t(x, v_\parallel)} \Big[f(x, v_\perp, v_\parallel) - f(\xi(x, v_\parallel), \zeta(x, v_\parallel), v_\perp) \Big] \psi_{kl} \\ &= -\int_{kl} dv_\parallel dv_\perp v_\perp \psi_{kl} \nabla_v \cdot \mathbf{\Gamma}[f](x, v_\perp, v_\parallel). \end{aligned} \tag{4.19}$$

The integral subscript kl means that our integration limits are only over the region where $\psi_{kl} \neq 0$. The last term in equation (4.19) contains second derivatives of f since it is a divergence of $\mathbf{\Gamma}$, which itself has first order derivatives of f in it, as defined in (1.21). Second derivatives could be problematic due to the first derivative discontinuities in ψ_{kl} (see Figure 4.2). To avoid problems, we integrate the last term by parts, and then express f in terms of ψ_{kl} using (4.18). This gives

$$\begin{aligned}&\int_{kl} dv_\parallel dv_\perp v_\perp \frac{1}{\Delta t(x, v_\parallel)} \Big[f(x, v_\perp, v_\parallel) - f(\xi(x, v_\parallel), \zeta(x, v_\parallel), v_\perp) \Big] \psi_{kl} \\ &= -\int_{kl} dv_\parallel dv_\perp v_\perp \nabla_v \psi_{kl} \cdot \mathbf{\Gamma}[f](x, v_\perp, v_\parallel) + \int_{S_v} dS_v \psi_{kl} \mathbf{\Gamma}[f](x, v_\perp, v_\parallel) \cdot \hat{\boldsymbol{n}}, \end{aligned} \tag{4.20}$$

where S_v is the boundary surface of the computational domain in velocity space, dS_v is the infinitesimal surface element on S_v and $\hat{\boldsymbol{n}}$ is the unit vector normal to dS_v. The only terms we need to consider about are the basis functions that are non zero at the boundaries of the full velocity space. In the numerical implementation of the model, we use a velocity grid with boundaries at some finite values of $v_\parallel$, $v_\perp$, $v'_\perp$ and $v'_\parallel$. Since $\mathbf{\Gamma} = f(\boldsymbol{v})[...] + \boldsymbol{\nabla_v} f(\boldsymbol{v})[..]$ and our integration limits are at large $v_\perp, v_\parallel$, the boundary terms are close to zero as long as the distribution function f decays quickly enough at large v (which will be true for any physical system). Thus we set the surface term to zero at these points. This ensures that no particles, momentum or energy is lost or gained by the system through the boundary at large $v_\parallel$ or $v_\perp$. This argument does not hold at the parallel velocity space boundaries at $x = 0$ and $x = x_{N_x - 1}$. At these spatial locations,

one of the velocity space boundaries is at $v_\parallel = 0$. Here the boundary terms may not be zero because at $v_\parallel = 0$ we have, in general, that $\mathbf{\Gamma} \cdot \hat{\boldsymbol{n}} \neq 0$. However, the integrand of the boundary terms is multiplied by the basis function ψ_{kl}. The only basis function that is non-zero at $v_\parallel = 0$, which is the boundary, is ψ_{kJ}, where J is the grid point in parallel velocity space at which its value is zero, $v_{\parallel J} = 0$. The distribution function at $x = 0$ and $x = x_{N_x-1}$ is fixed at $v_\parallel = 0$ by the boundary conditions and so we do not solve equation (4.20) for the ψ_{kJ} terms at these spatial locations (we only solve for $l > J$ at $x = 0$ and for $l < J$ at $x = x_{N_x-1}$). As a result, the boundary term is zero everywhere and can be neglected.

4.2.1 Integration method: Gaussian quadrature

In our code, the integrals in each element are evaluated using the Gaussian quadrature method which approximates the integral of a function $\mathcal{F}(y)$ as

$$\int dy \mathcal{F}(y) \simeq \sum_{i=1}^{p} \varpi_i \mathcal{F}(y_i^G), \tag{4.21}$$

where ϖ_i are the weights associated with each point y_i^G, and p indicates the number of points used to calculate the integral. Note that the choice of integration points y_i^G is independent of the earlier discussed grid points y_i (for velocity space we had, $v_{\parallel i}, v_{\perp i}$). Grid points y_i label the nodes of the finite element basis functions $\psi_j(y)$, the basis function can be evaluated at any y point. We choose to use Gauss-Legendre weights ϖ_i and points y_i^G, for which the approximation is exact if $\mathcal{F}(y)$ is a polynomial of order $2p-1$ or lower. Gaussian quadrature is used for integration in every element in $v_\perp, v_\parallel, v'_\perp$ and $v'_\parallel$. Having a higher number of points (p) improves the accuracy of the integral, but it slows down the code and requires more memory. We choose to use $p = 4$ quadrature points as a larger number did not affect the results significantly. This means the scheme can compute polynomials up to order seven in every element in any velocity direction exactly.

To evaluate the errors, we consider the following problem, which will be of interest later: finding a function $f_{Num} = \sum_{kl} a_{kl} \psi_{kl}(v_\perp, v_\parallel)$ that best describes a Maxwellian function $f_M = \frac{1}{\pi^{3/2}} \exp\left(-v_\parallel^2 - v_\perp^2\right)$ in the space spanned by quadratic finite elements ψ_{ij}, that is, we want to find a_{kl} such that

$$\sum_{k,l} a_{kl} L_{klij} = R_{ij}, \tag{4.22}$$

where $L_{klij} \equiv \int d^3\boldsymbol{v}\psi_{kl}\psi_{ij}$ and $R_{ij} \equiv \int d^3\boldsymbol{v} f_M \psi_{ij}$. For this test we choose the grids to be from -3 to 3 in $v_\parallel$ and from 0 to 3 in $v_\perp$. We divide the grids into 10 elements in the parallel velocity grid and 6 elements in the perpendicular velocity grid, giving $N_\parallel = 13$ grid points in the parallel velocity, and $N_\perp = 21$ grid points in the perpendicular velocity. The distance between grid points is uniform in each direction. We remind the reader that the grid points here are defined as the nodes of the finite element basis functions, in each element the integrals are computed using (4.21) by evaluating the basis functions $\psi(v_\perp, v_\parallel)$ at the appropriate Gauss-Legendre points. The integrals in equation (4.22) can be done analytically to get a_{kl}^{exact}. We compare this analytical result to the integrals done using numerical Gaussian quadrature method for different number of Gaussian points. To find how good the numerical solution is, we compute the maximum difference $D \equiv \max|a_{kl}/a_{kl}^{exact} - 1|$ and plot D vs the number of Gaussian quadrature points p in Figure 4.3. We also plot the errors of the integrals on the left hand side and right hand sides of equation (4.22), labelling them $D_{LHS} \equiv \max\left|L_{klij}/L_{klij}^{exact} - 1\right|$ and $D_{RHS} = \max|R_{kl}/R_{kl}^{exact} - 1|$, respectively. The integrands in L_{klij} are fourth order in $v_\parallel$ and and fifth order in $v_\perp$, since the basis functions are quadratic and the integration Jacobian contains an extra $v_\perp$. Therefore, we expect the error to be zero for $p \geq 3$ due to the properties of the Gauss-Legendre points. The integrand in R_{ij} is a product of a Maxwellian and a quadratic element. Thus it cannot be represented via a finite number of polynomials and the quadrature method will always produce an error that will decrease in a non-linear [44] way with increasing p. These properties are confirmed by Figure 4.3.

4.2.2 Velocity space grids

We now explain the choice of the velocity space grids. In this work we choose to use a rectangular grid in the $(v_\perp, v_\parallel)$ space. The velocity grids in perpendicular and parallel directions are normalised in units of $v_{t\infty}$ (see equation (2.54)). The velocity grids are the same at every x location. In these units, the Maxwellian distribution function at $x \to \infty$ boundary is given by

$$f_M(x, v_\perp, v_\parallel) = \frac{1}{\pi^{3/2}} \exp\left(-(v_\parallel - u_{\parallel\infty})^2 - v_\perp^2\right). \tag{4.23}$$

To ensure that the boundary condition for the collisional flux $\boldsymbol{\Gamma}$ at velocity space boundaries, $\boldsymbol{\Gamma}$ =0, is valid (the collision operator will be discussed in more detail in Section

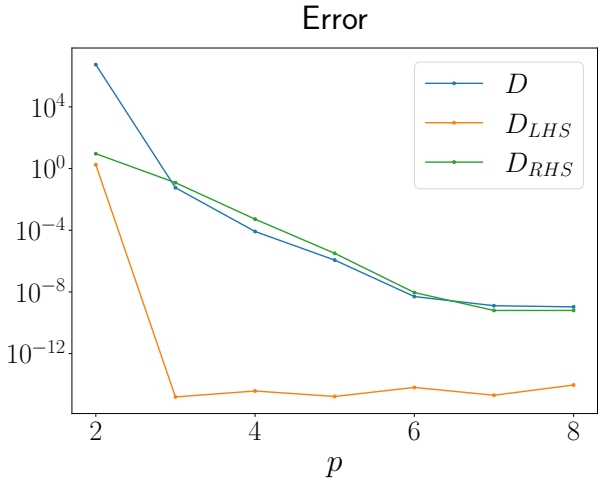

Figure 4.3: The size of the errors due to numerical integration of integrals in equation (4.22). The error in a_{kl} is D, and the errors of the integrals on the left and right sides of equation (4.22) are D_{LHS} and D_{RHS}, respectively (see text for definitions of D, D_{LHS} and D_{RHS}). The errors are given by the blue, orange and green curves respectively. Note that the error of the left hand side is zero to machine precision for $p \geq 3$ because the integrands are polynomials of order $v_\perp^5$, $v_\parallel^5$ or lower.

4.3.2), and to ensure accuracy of integrals over velocity space, we choose the maximum values of the velocity grid points to be 3 units away from the peak of the Maxwellian f_M at $x \to \infty$. That is, $u_{\parallel\infty} - 3 \leq v_\parallel \leq u_{\parallel\infty} + 3$ and $0 \leq v_\perp \leq 3$. At these velocity space boundary points the value of f_M is a factor of 10^-4 of its maximum value. The error in the Newton's method used to find the solution is of similar order, making the choice of grid sizes appropriate (our Newton's method is described in detail in Section 4.4). The spacing between two grid points in perpendicular velocity space is $\Delta v_{\perp k} = v_{\perp,k+1} - v_{\perp k}$, and in parallel velocity space it is $\Delta v_{\parallel l} = v_{\parallel,l+1} - v_{\parallel l}$. We label the index at which $v_\parallel = 0$ by J, that is, $v_{\parallel J} = 0$.

The trajectories discussed in Section 4.1 have a constant $v_\perp(t)$. In addition, the wall boundary condition does not explicitly affect the $v_\perp$ coordinate. The collision operator prevents sharp gradients from developing in $v_\perp$ and $v_\parallel$. As a result, the distribution function does not develop any fine structure in $v_\perp$ (see Figure 4.4) and we use uniform spacing in the $v_\perp$ coordinate. To reduce computational costs most of the simulations performed have 6 quadratic elements (13 grid points) in $v_\perp$ space. The code can also be run with a non-uniform grid.

The dynamics in the $v_\parallel$ coordinate are more interesting due to the left hand side of the kinetic equation containing explicit $v_\parallel$ terms and due to the wall boundary condition,

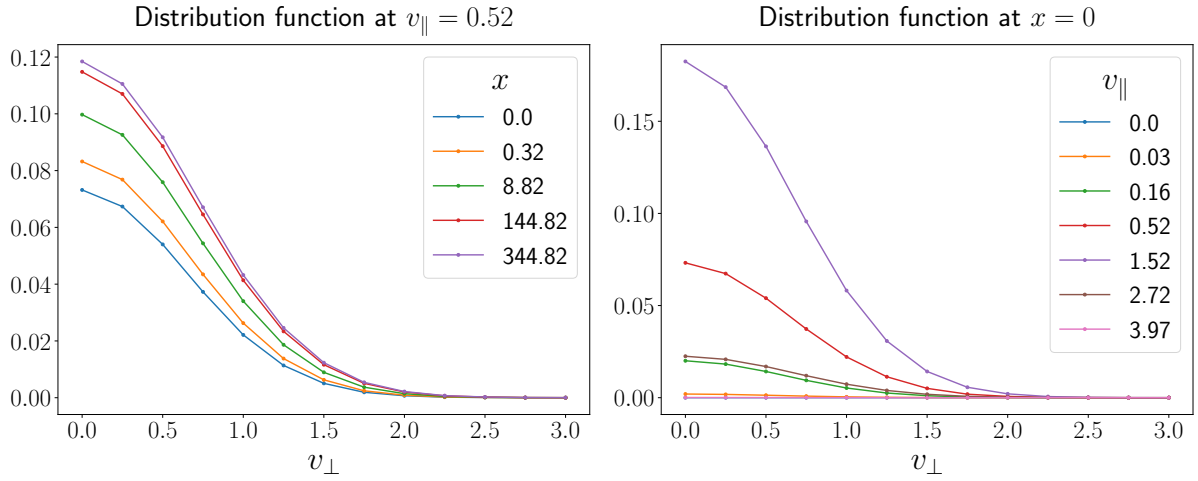

Figure 4.4: The ion distribution function as a function of $v_\perp$ for a range of x at a point $v_\parallel = 0.52$ (left) and for a range of $v_\parallel$ at $x = 0$ (right). The structure in $v_\perp$ does not require high resolution and, up to a scale factor, is similar across all x and $v_\parallel$. The boundary condition at $x \to \infty$ is a Maxwellian with $\Delta_s = 0.01$ and $T_e = 0.5$.

enforcing $f(x = 0, v_\parallel < 0) = 0$. Due to this boundary condition, we choose our finite element basis functions such that one of the boundaries between elements is at $v_\parallel = 0$. Having $v_\parallel = 0$ inside the element, instead of at its boundary, would require the basis polynomials to sum to zero on the $v_\parallel < 0$ part of the element domain while having a finite value in the rest of the domain. This is impossible to achieve exactly with a finite polynomial basis. The polynomial approximations can lead to Gibbs ringing and complicates the analysis.

Due to the wall boundary condition, large derivatives with respect to $v_\parallel$ of the integrand of the Chodura condition, $f/v_\parallel^2$, develop at $x = 0$ and $v_\parallel \ll 1$ requiring high resolution (see discussion of the kinetic Chodura condition in Section 5.4). In addition, to calculate the integral appearing in the kinetic Chodura condition (3.5), we need to capture the behaviour of f at very small $v_\parallel$ accurately. Therefore, we ensure that the parallel velocity resolution in this region is the highest. Satisfying the kinetic Chodura condition relies on resolving the trajectories that come from the MPE with $v_\parallel(t - \Delta t) < 0$ and turn back, intersecting the MPE at $v_\parallel(t) = -v_\parallel(t - \Delta t)$. Numerically this means that in the simulation we must have particles that do not have enough kinetic energy to reach the next grid point. That is, from (4.5), $v_\parallel^2/2 < \phi(x_1) - \phi(x = 0)$. We know that the potential scales as $\phi(x) - \phi(0) \sim x^{1/2}$. Hence, we want to make sure that there are many particles with $v_\parallel \lesssim x_1^{1/4}$, where x_1 is the second grid point in the position space (the first

one is the MPE at $x_0 = 0$). We choose the first element in $v_\parallel > 0$ space to have the highest resolution equal to $\Delta v_{\parallel J} = x_1^{1/4}/N_v$, where N_v is an integer, which for most simulations is set to $N_v = 50 - 200$ (the highest N_v that we have used was $N_v = 50000$ when trying to resolve $f/v_\parallel^2$ peaks for large Δ_s or low T_e, see Section 5.4). We then gradually increase the spacing as we move away from this element (both in negative and positive $v_\parallel$). The lowest resolution used in some of the runs is $\Delta v_{\parallel l} = 0.2$ for grid points with $v_\parallel \gtrsim u_{\parallel\infty}$ and $v_\parallel \lesssim -1$, since here the ion distribution function has lower gradients. Overall we have $\sim 70 - 100$ grid points in $v_\parallel$ corresponding to $\sim 35 - 50$ elements. For values of x_1 used in the simulations ($x_1 = 10^{-7} - 10^{-2}$) the smallest velocity space resolution is $\sim 10^{-4} - 10^{-2}$.

4.3 Collision operator

In this Section we discuss the implementation of the collisional operator into our code using the finite element formalism. A similar discretisation has been used in [45] to solve a collisional relaxation problem $\partial f/\partial t = C[f, f]$.

Since we have argued that the boundary terms in equation (4.20) vanish, we focus on the integrals

$$C_{kl} = -\int d\varphi dv_\perp dv_\parallel \; v_\perp \nabla_v \psi_{kl} \cdot \mathbf{\Gamma}. \tag{4.24}$$

The gradients of the basis functions in velocity space are

$$\nabla_v \psi_{kl}(\mathbf{v}) = \frac{\partial \psi_{kl}}{\partial v_\parallel}\hat{\mathbf{b}} + \frac{\partial \psi_{kl}}{\partial v_\perp}\hat{\mathbf{v}}_\perp. \tag{4.25}$$

Therefore, using equation (1.24) the integral is

$$\begin{aligned} C_{kl} = -\int dv_\perp dv_\parallel dv'_\perp dv'_\parallel & \frac{4\pi}{((v_\parallel - v'_\parallel)^2 + (v_\perp + v'_\perp)^2)^{1/2}} \\ \times \Bigg\{ & \left[X_{\parallel\parallel}\left(f' \frac{\partial f}{\partial v_\parallel} - f \frac{\partial f'}{\partial v'_\parallel} \right) + X_{\parallel\perp} f' \frac{\partial f}{\partial v_\perp} + X_{\parallel\perp'} f \frac{\partial f'}{\partial v'_\perp} \right] \frac{\partial \psi_{kl}}{\partial v_\parallel} \\ + & \left[X_{\perp\parallel}\left(f' \frac{\partial f}{\partial v_\parallel} - f \frac{\partial f'}{\partial v'_\parallel} \right) + X_{\perp\perp} f' \frac{\partial f}{\partial v_\perp} + X_{\perp\perp'} f \frac{\partial f'}{\partial v'_\perp} \right] \frac{\partial \psi_{kl}}{\partial v_\perp} \Bigg\}, \end{aligned} \tag{4.26}$$

where the coefficients $X_{\parallel\parallel}, X_{\parallel\perp}, X_{\parallel\perp'}, X_{\perp\parallel}, X_{\perp\perp}$ and $X_{\perp\perp'}$ are defined in equation (1.25).

Due to the representation of f in our basis functions (given in equation (4.18)), we can precompute a tensor T_{klmnij}, which is defined as

$$\begin{aligned} T_{klmnij} = &- \int dv_\perp dv_\parallel dv'_\perp dv'_\parallel \frac{4\pi}{((v_\parallel - v'_\parallel)^2 + (v_\perp + v'_\perp)^2)^{1/2}} \\ &\times \left\{ \left[X_{\parallel\parallel} \left(\psi'_{ij} \frac{\partial \psi_{mn}}{\partial v_\parallel} - \psi_{mn} \frac{\partial \psi'_{ij}}{\partial v'_\parallel} \right) + X_{\parallel\perp} \psi'_{ij} \frac{\partial \psi_{mn}}{\partial v_\perp} + X_{\parallel\perp'} \psi_{mn} \frac{\partial \psi'_{ij}}{\partial v'_\perp} \right] \frac{\partial \psi_{kl}}{\partial v_\parallel} \right. \\ &+ \left. \left[X_{\perp\parallel} \left(\psi'_{ij} \frac{\partial \psi_{mn}}{\partial v_\parallel} - \psi_{mn} \frac{\partial \psi'_{ij}}{\partial v'_\parallel} \right) + X_{\perp\perp} \psi'_{ij} \frac{\partial \psi_{mn}}{\partial v_\perp} + X_{\perp\perp'} \psi_{mn} \frac{\partial \psi'_{ij}}{\partial v'_\perp} \right] \frac{\partial \psi_{kl}}{\partial v_\perp} \right\}. \end{aligned} \tag{4.27}$$

Computing the tensor T_{klmnij} uses most of the memory required to run the code as for each component we need to perform integrals in 4 velocity dimensions. However, it speeds up the calculations significantly as it can be computed once initially for a given velocity grid and then be used to find C_{kl} at every iteration,

$$C_{kl} = \sum_{\substack{m \in el(k) \\ n \in el(l)}} \sum_{i,j}^{N_\perp, N_\parallel} a_{ij} a_{mn} T_{klmnij}. \tag{4.28}$$

Some memory usage is saved by the fact that the k and m indices denote the basis function in $v_\perp$ space and therefore the integrand is non zero only if the basis functions overlap. The same applies to the l and n indices for $v_\parallel$. This is what the summations over m and n indicate. For a given k, $el(k)$ denotes a set of nodes inside the element(s) that contain k. Summation over other points will give zero. The derivative of C_{kl} with respect to the weights a_{mn}, which we will use in Section 4.4, is given by

$$\frac{\partial C_{kl}}{\partial a_{mn}} = \sum_{\substack{i \in el(k) \\ j \in el(l)}} a_{ij} T_{klijmn} + \sum_{i,j}^{N_\perp, N_\parallel} a_{ij} T_{klmnij}. \tag{4.29}$$

4.3.1 Approximating a Maxwellian

We need to ensure that the collision operator evaluates to zero if f is a Maxwellian distribution. High precision of this property is important when evaluating the Maxwellian distribution at the boundary x_{N_x-1} of our x space. A non-zero value of the collision operator incorrectly gives a non-zero gradient in particle density, and thus the potential, at infinity.

To see that $C[f_M] = 0$ analytically, we use the fact that for a Maxwellian distribution, given in (4.23), we have $\nabla_v \ln f_M(\boldsymbol{v}) - \nabla_{v'} \ln f_M(\boldsymbol{v}') = 2\frac{\boldsymbol{v}-\boldsymbol{v}'}{v_{ti}^2} = 2\frac{\boldsymbol{g}}{v_{ti}^2}$, we plug this into

equation (3.2) and use $\nabla_g \nabla_g g \cdot \boldsymbol{g} = 0$, which gives $\boldsymbol{\Gamma} = 0$ and hence $C[f_M] = 0$. Due to finite resolution of the numerical implementation, this property is not reproduced by the numerical operator. We want to find what numerical distribution function f_{Num} gives $C_{kl} \simeq 0$. This is the function that the collisions try to force the distribution function to relax to and is the function we put in at our x space boundary at $x = x_{N_x-1}$.

Our numerical distribution function must be in the space spanned by our basis functions ψ_{kl}, that is, $f_{Num} = \sum_{k,l} a_{kl}\psi_{kl}$. The basis functions are Lagrange polynomials and therefore f_{Num} will not be an exact Maxwellian. There are three options we could reasonably consider as our numerical Maxwellians.

I. The first option is to take $a_{kl}^{(\mathrm{I})} = f_M(v_{\perp k}, v_{\parallel l})$ to ensure that the numerical distribution function is exactly equal to the Maxwellian at the velocity grid points.

II. The second option is to require that the numerical and analytic Maxwellian functions satisfy weak equality, in the same way as we do in the example problem in Section 4.2.1 (equation (4.22)), that is, for all i, j, we require

$$\sum_{k,l} a_{kl}^{(\mathrm{II})} \int d^3\boldsymbol{v}\psi_{kl}\psi_{ij} = \int d^3\boldsymbol{v} f_M \psi_{ij}. \tag{4.30}$$

III. The final option is to numerically solve equation $C_{kl}[\{a_{ij}^{(\mathrm{III})}\}] = 0$, with the constraints that f_{Num} has the desired density, mean flow and temperature. The details of this calculation are given in Appendix F.

These should all converge as resolution in velocity space is increased. We use a Maxwellian $f_M = (1/\pi^{3/2}) \exp\big(-(v_\parallel - 1)^2 - v_\perp^2\big)$ to test the accuracy of these methods. The maximum difference between the distribution function weights $a_{kl}^{(\mathrm{II})} - a_{kl}^{(\mathrm{I})}$ and $a_{kl}^{(\mathrm{III})} - a_{kl}^{(\mathrm{I})}$ as a function of the number of elements in $v_\parallel$ is shown in Figure 4.5 on the left. On the right in Figure 4.5, we show the norm of $C_{kl}[a_{ij}^{(n)}]$, where n labels the three possible choices I, II and III, as a function of number of elements in $v_\parallel$. Different colours represent a different number of elements in $v_\perp$. As resolution increases, the collision operator approaches zero for all choices of the distribution function. However, a very high resolution is needed if we want to use choices I or II. The third choice has a distribution function that has collision operator zero to machine precision at low resolution and approaches a Maxwellian as resolution is increased. To avoid gradients in density developing

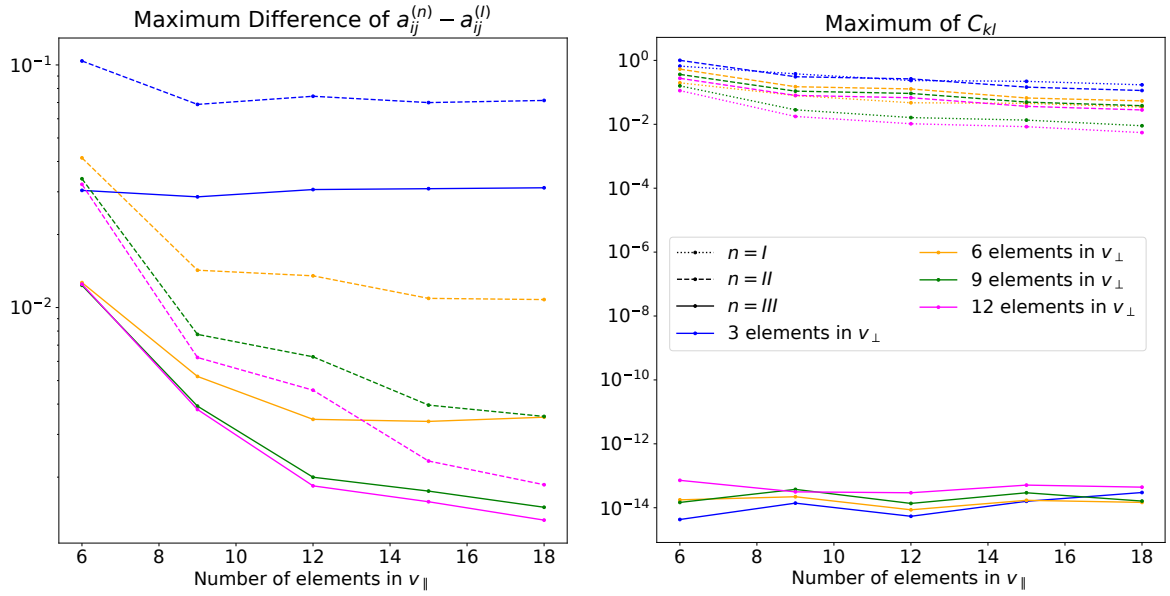

Figure 4.5: Differences between a_{ij} (left figure) and maximum value of $C_{kl}[\{a_{ij}\}]$ (right figure) for different methods used to approximate a Maxwellian as a function of the number of elements in $v_\parallel$ and $v_\perp$. Dotted lines represent $a_{ij}^{(\mathrm{I})}$, the values of the Maxwellian at the velocity grid points. Dashed lines represent $a_{ij}^{(\mathrm{II})}$, found using equation (4.30). Solid lines represent $a_{ij}^{(\mathrm{III})}$, which solves the numerical collision operator.

at the boundary far away from the wall, we choose to use the option III as the boundary condition at $x = x_{N_x-1}$.

Figure 4.6 shows density as a function of x for two simulations ($\Delta_s = 0.1$, $T_e = 1$) only differing by the choice of the distribution function at the boundary at x_{N_x-1}. To see the effect of choosing option I as a boundary condition, the domain of the plot shown is approximately $280 < x < 440$. The largest difference between the two distribution functions is $\sim 10^{-3}$. The maximum value of $C_{kl}[\{a_{ij}\}]$ is equal to $\sim 10^{-3}$, when a simple interpolation of a Maxwellian (option I) is used, and it is $\sim 10^{-15}$ for the distribution function that solves the collision operator (option III) computed using the method in Appendix F. These errors depend weakly on the parameters Δ_s and T_e. The error using option I is small, but it results in the electric field changing sign near the boundary $x \to \infty$. High precision of the potential profile at large x is needed when comparing the results to analytical predictions, such as those in Section 2.3. The accuracy is improved by using option III.

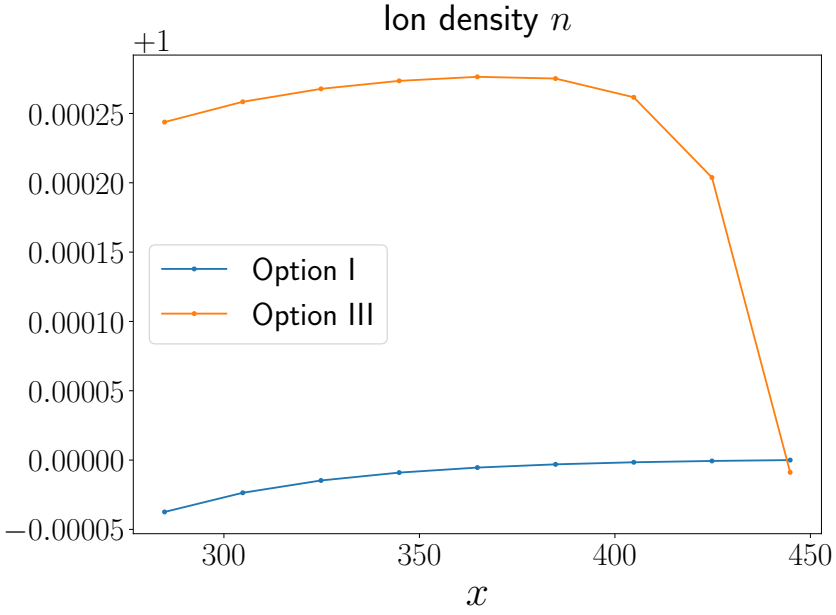

Figure 4.6: Particle density as a function of x for different implementations of the Maxwellian distribution at the boundary far away from the wall. The domain is restricted to approximately $280 < x < 440$. The blue line uses $a_{kl}^{(\mathrm{I})} = f_M(v_{\perp k}, v_{\parallel l})$ as a boundary condition at $x = 440$. The orange line uses $a_{kl}^{(\mathrm{III})}$, found by minimising $C_{kl}[\{a_{ij}\}]$ (see Appendix F), as the boundary condition

4.3.2 Conservation laws and entropy production

The form of C_{kl} given in (4.26) is useful because it ensures that our collision operator satisfies the correct conservation laws. To remind the reader of the conservation properties of the collision operator, we multiply it by $\chi(\mathbf{v})$, which represents one of the three moments $\chi(\mathbf{v}) = \{1, v_\parallel, v_\parallel^2 + v_\perp^2\}$, and integrate over velocity space. After integration by parts, we find

$$I_\chi = -\int d^3\mathbf{v} \int d^3\mathbf{v}' \nabla_v f f' \chi(\mathbf{v}) \cdot \nabla_g \nabla_g g \cdot \left[\nabla_v \ln f(\mathbf{v}) - \nabla_v' \ln f(\mathbf{v}')\right], \tag{4.31}$$

where I_χ represents particle number, momentum or energy production. We can obtain a new equation by swapping the integration variables $\mathbf{v}$ and $\mathbf{v}'$ in (4.31). We use the fact that $\nabla_g \nabla_g g$ is symmetric under this swap and add this new equation to (4.31) to get

$$2I_\chi = -\int d^3\mathbf{v} \int d^3\mathbf{v}' f f' \left[\nabla_v \chi(\mathbf{v}) - \nabla_{v'} \chi(\mathbf{v}')\right] \cdot \nabla_g \nabla_g g \cdot \left[\nabla_v \ln f(\mathbf{v}) - \nabla_{v'} \ln f(\mathbf{v}')\right] = 0. \tag{4.32}$$

For $\chi = \{1, v_\parallel\}$ the term $\nabla_v \chi(\mathbf{v}) - \nabla_{v'} \chi(\mathbf{v}') = 0$ identically. For $\chi = v^2$, this term is $2\mathbf{v} - 2\mathbf{v}' = 2\mathbf{g}$. Using (1.22), we see that $\mathbf{g} \cdot \nabla_g \nabla_g g = 0$. Therefore $I_\chi = 0$ for all the

three moments giving particle, parallel momentum and energy conservation equations,

$$\int d^3\mathbf{v}\, C[f,f] = 0, \tag{4.33}$$

$$\int d^3\mathbf{v}\, v_\parallel C[f,f] = 0, \tag{4.34}$$

$$\int d^3\mathbf{v}\, (v_\parallel^2 + v_\perp^2) C[f,f] = 0. \tag{4.35}$$

To show that these properties are satisfied by the discretisation, we note that

$$\sum_{k=1,l=1}^{K,L} \psi_{kl} = 1, \tag{4.36}$$

$$\sum_{k=1,l=1}^{K,L} v_{\parallel l}\psi_{kl} = v_\parallel, \tag{4.37}$$

$$\sum_{k=1,l=1}^{K,L} (v_{\parallel l}^2 + v_{\perp k}^2)\psi_{kl} = v_\parallel^2 + v_\perp^2. \tag{4.38}$$

The last equality only holds for quadratic (or higher order) basis functions. According to equations (4.36), (4.37) and (4.38), to check that the conservation laws hold in our numerical scheme, we need to show that

$$\sum_{k=1,l=1}^{K,L} C_{kl} = 0, \tag{4.39}$$

$$\sum_{k=1,l=1}^{K,L} v_{\parallel l} C_{kl} = 0, \tag{4.40}$$

$$\sum_{k=1,l=1}^{K,L} (v_{\parallel l}^2 + v_{\perp k}^2) C_{kl} = 0. \tag{4.41}$$

The quantities give zero if equation (4.26) is integrated analytically. Even if approximate integration (here we use Gaussian quadrature) is used to find integral (4.26), equations (4.39)–(4.41) still give zero. This is because the conservation laws only depend on how the integrand changes under the swapping of $(v_\perp, v_\parallel)$ with $(v'_\perp, v'_\parallel)$. This property is not affected by our integration scheme. Particle conservation equation (4.39) is satisfied trivially because equation (4.36) gives $\sum_{kl} \partial\psi_{kl}/\partial v_\parallel = 0$ and $\sum_{kl} \partial\psi_{kl}/\partial v_\perp = 0$. Momentum conservation (4.39) relies on the fact that the integrand of C_{kl} is anti-symmetric under the swapping of the primed and unprimed variables, which remains true in the Gaussian

quadrature scheme. Finally, for energy conservation the fact that the basis functions are quadratic, combined with (4.38) implies that

$$\sum_{k=1,l=1}^{K,L} (v_{\parallel l}^2 + v_{\perp k}^2)\frac{\partial \psi_{kl}}{\partial v_\parallel} = 2v_\parallel, \tag{4.42}$$

$$\sum_{k=1,l=1}^{K,L} (v_{\parallel l}^2 + v_{\perp k}^2)\frac{\partial \psi_{kl}}{\partial v_\perp} = 2v_\perp. \tag{4.43}$$

Therefore, when using Gaussian quadrature to evaluate the integral, the terms $\nabla_v \mathbf{v}^2 - \nabla_{v'}\mathbf{v}'^2 = 2\mathbf{g}$ exactly, which means $\mathbf{g}\cdot\nabla_g\nabla_g g = 0$ is exact at every quadrature point. Had we chosen linear basis functions, equation (4.42), and thus the identity $\mathbf{g}\cdot\nabla_g\nabla_g g = 0$, would not be exact and energy conservation would not be ensured. It is worth noting that it has been shown that it is possible to ensure energy conservation with linear elements only [46] by approximating the velocity variables in the integrand. Figure 4.7 shows the quantities given by the equations (4.39)–(4.41), for different points in our position space, as a function of the iteration number in the Newton's method – used to obtain the solutions for $\Delta_s = 0.01, 0.1, 1$ and $T_e = 0.5, 1, 2$. The quantities are zero up to numerical precision in our code.

To show that the model satisfies entropy production, we need to show that

$$-\int d^3\mathbf{v}\ln f C[f,f] = \int d^3\mathbf{v}\int d^3\mathbf{v}' f f' \frac{\nabla_v f}{f}\cdot\nabla_g\nabla_g g\cdot\left(\frac{\nabla_v f}{f} - \frac{\nabla_{v'} f'}{f'}\right) \geq 0 \tag{4.44}$$

is greater than zero. Obtaining a new equation by relabelling variables $\mathbf{v} \leftrightarrow \mathbf{v}'$ and then adding that equation to equation (4.44) gives an integrand of the form $ff'\mathbf{a}\cdot\nabla_g\nabla_g g\cdot\mathbf{a}$, where $\mathbf{a} \equiv \boldsymbol{\nabla}_\mathbf{v}\ln f - \boldsymbol{\nabla}_{\mathbf{v}'}\ln f'$ is the vector in the brackets in equation (4.44). This integrand is positive for all values of $v_\perp, v_\parallel, v'_\perp, v'_\parallel$. This is because the tensor in the collision operator has the property $\mathbf{a}\cdot\nabla_g\nabla_g g\cdot\mathbf{a} \geq 0$ for all $\mathbf{a}$ and $f > 0$ for all $\mathbf{v}$. The Gaussian quadrature method of integration has no effect on this property. However, we could have issues ensuring the positivity of the entropy production if the distribution function ever becomes negative. We only expect this to happen in small regions of velocity space and thus not change the sign of the total integral. In addition, the function that multiplies $C[f]$ in the integrand (in this case the function is $\ln f$) can only be used in our numerical method if it can be expanded in the basis functions ψ_{kl}. There is no easy formula for the expansion of the logarithm of a function $f = \sum a_{kl}\psi_{kl}$ that itself is an

expansion in these basis functions. We choose to use $\ln f = \sum b_{kl}\psi_{kl}$, where b_{kl} are found using $b_{kl} = \ln(|a_{kl}|)$. This means that the identity $\mathbf{a}\cdot\nabla_g\nabla_g g\cdot\mathbf{a} \geq 0$ can no longer be used as we are just approximating the function and so have an integral

$$\int d^3\mathbf{v}d^3\mathbf{v}' f f'\left(\frac{\nabla_v h}{h} - \frac{\nabla_{v'}h'}{h'}\right)\cdot\nabla_g\nabla_g g\cdot\left(\frac{\nabla_v f}{f} - \frac{\nabla_{v'}f'}{f'}\right), \tag{4.45}$$

where h and f are not exactly equal, as $\ln h = \sum_{kl} b_{kl}\phi_{kl} \neq \ln(\sum_{kl} a_{kl}\phi_{kl})$. However at high enough resolution the functions are approximately equal and so we should expect the inequality

$$\sum_{k,l} b_{kl}C_{kl} \geq 0 \tag{4.46}$$

to hold in most cases. This quantity for different points in position space, as a function of iteration number in the Newton's method – used to obtain the solutions for $\Delta_s = 0.01, 0.1, 1$ and $T_e = 0.5, 1, 2$ – is shown in Figure 4.7. Most of the values are positive as they should be. Although not visible in the graph, there are a few points where the value is negative $\sim -10^{-8}$. The plot shows a clear convergence of the solutions as the entropy production remains constant after a few iterations.

4.4 Newton's Method

To solve the nonlinear set of equations (4.20), we use Newton's method. We have chosen $\Delta t(x(t), v_\parallel(t))$ such that $x(t)$ and $x(t-\Delta t)$ in the equations (4.20) are grid points in our position space x. Therefore, we are solving the set of equations for every spatial grid point, that is, $x(t) = x_q$ for $q = 0, .., N_x - 1$. It is then useful to write the distribution functions for every q as

$$f(x_q, v_\perp, v_\parallel) = \sum_{m=1,n=1}^{N_\perp, N_\parallel} a_{qmn}\psi_{mn}(v_\perp, v_\parallel), \tag{4.47}$$

where now the weights a_{qmn} have an additional index q labelling the position in space. By moving all the collision terms of equation (4.20) to the left hand side, we get a set of equations for every $q = 0, ..., N_x - 1$, which can be written in the form

$$M_{qkl}(\{a_{pmn}\}) = 0, \quad p = 0, ..., N_x - 1, \quad k, m = 1, ..., N_\perp, \quad l, n = 1, .., N_\parallel, \tag{4.48}$$

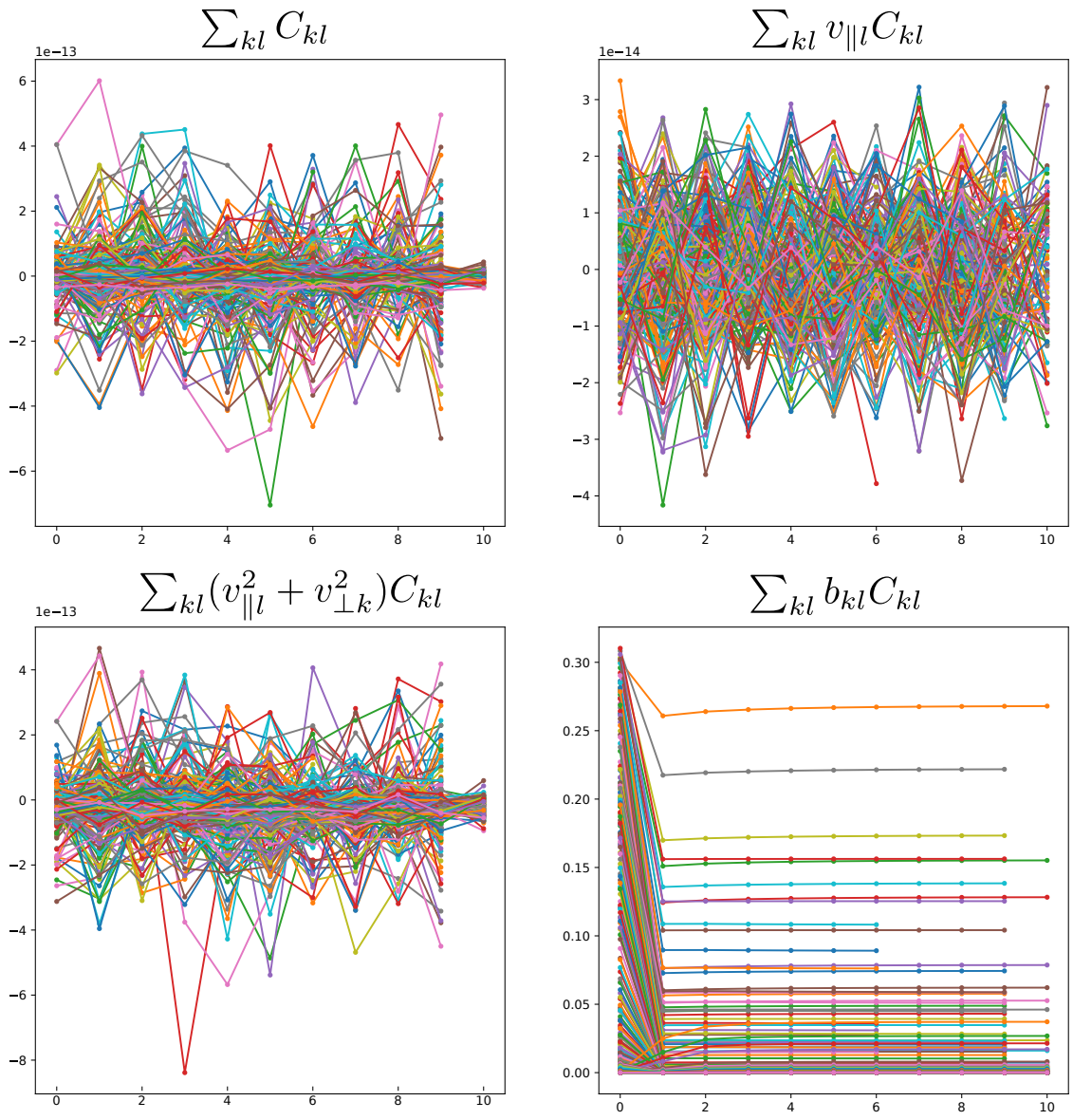

Figure 4.7: Moments of the collision operator showing particle, parallel momentum and energy conservation and entropy as a function of the iteration number of various simulations, with different curves representing different points in x space.

where

$$M_{qkl}(\{a_{pmn}\}) \equiv 2\pi \int dv_{\parallel} dv_{\perp} v_{\perp} \frac{f(x_q, v_{\parallel}, v_{\perp}) - f(\xi, \zeta, v_{\perp})}{\Delta t} \psi_{kl} - C_{kl}. \tag{4.49}$$

The notation $\{a_{pmn}\}$ means that, in general, the function M_{qkl} depends on all the weights in the system. From the right side of (4.49), M_{qkl} can only depend on $q-1 \leq p \leq q+1$ via ξ, ζ and Δt (see equations (4.5), (4.6), (4.9) and (4.13) for the explicit dependence). The collision operator term only depends on the distribution function at x_q, which is the point at which the the derivative df/dt is evaluated.

When solving the equation numerically, we will always have some error in the solution. The value of $M_{qkl}(\{a_{pij}\})$ is proportional to the element size in which the basis function ψ_{kl} is not zero. This means that if the resolution in velocity space is fine enough, and so the element volume is small, $M_{qkl}(\{a_{pij}\})$ may be small in absolute terms, but at the same time be large compared to the two terms of equation (4.49) and therefore a_{pij} may not actually be an accurate solution to the equation. We care about the accuracy in regions where the element size is small because the element size is smallest at small $v_{\parallel}$, where high resolution in velocity space is required as discussed in Section 4.2.2. This is the region where the difference between the distribution function at infinity and the distribution function at the MPE is the largest and it also dominates the evaluation of the Chodura integral in equation (3.5). To account for the volume of the finite elements, we normalise $M_{qkl}(\{a_{pij}\})$ by the volume of the velocity space element where the basis function ψ_{kl} is non zero. The volume element, for quadratic basis functions, is

$$N_{kl} \equiv v_{\perp k'+1}(\Delta v_{\perp k'} + \Delta v_{\perp k'+1})(\Delta v_{\parallel l'} + \Delta v_{\parallel l'+1}), \tag{4.50}$$

where the primed indices indicate the node at the lower edge of the element. In the cases where the basis function lies on the boundary of two elements, we choose the volume to be that of the element associated with the smaller values of $v_{\parallel}$ and $v_{\perp}$. We also normalise by $f_0 \equiv f(x = x_{N_x-1}, v_{\perp} = 0, v_{\parallel} = 0)$, the value of the distribution function at the boundary at infinity at $v_{\perp} = 0, v_{\parallel} = 0$, as this is a good estimate for the largest amount by which the distribution function changes across the domain. To see this, we plot in Figure 4.8 the distribution functions at $x = 0$ and $x = x_{N_x-1}$ as well as their difference, for a simulation with $\Delta_s = 0.1$, $T_e = 0.5$.

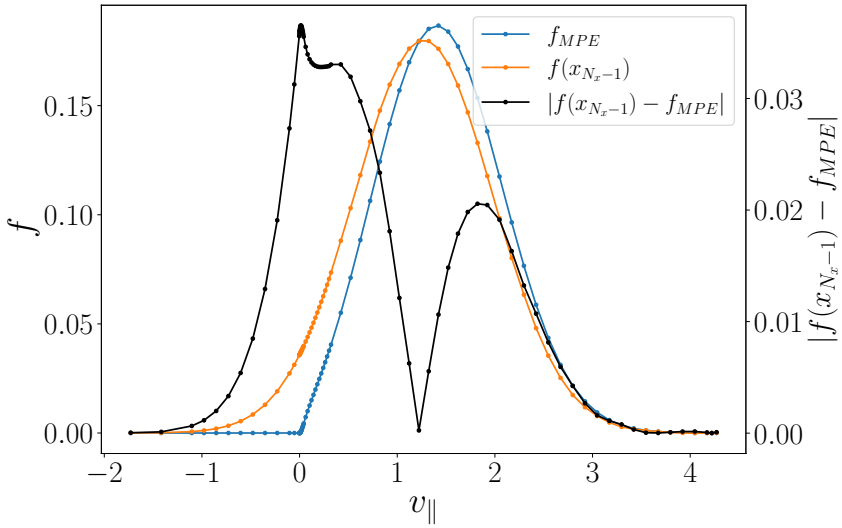

Figure 4.8: The distribution function at the MPE $f_{MPE} = f(x = 0, v_\perp = 0, v_\parallel)$ (blue curve), the distribution function at the boundary at infinity $f(x = x_{N_x-1}, v_\perp = 0, v_\parallel)$ (orange curve) and their difference (black curve) against $v_\parallel$, for $\Delta_s = 0.1$, $T_e = 0.5$.

Taking these normalisations into account, the equation we solve is

$$\bar{M}_{pkl}(\{a_{pmn}\}) = 0, \tag{4.51}$$

where

$$\bar{M}_{pkl}(\{a_{pmn}\}) = \frac{M_{pkl}(\{a_{pmn}\})}{\bar{N}_{kl}}. \tag{4.52}$$

Here we have introduced the normalisation matrix $\bar{N}_{kl} \equiv f_0 N_{kl}$. Note that the normalisation is independent of the distribution function itself and remains constant throughout the iterations.

Given an initial guess to the solution $a^{(0)}_{pij}$, Newton's method gives a better estimate of the solution $a^{(1)}_{pij} = a^{(0)}_{pij} + h^{(1)}_{pij}$, where $h^{(1)}_{pij}$ is found by inverting equation

$$\sum_{pij} \bar{J}^{(0)}_{pijqkl} h^{(1)}_{pij} = -\bar{M}_{qkl}(\{a^{(0)}_{pmn}\}), \tag{4.53}$$

where $\bar{J}$ is the normalised Jacobian tensor defined as $\bar{J}_{pijqkl} = \frac{\partial \bar{M}_{qkl}}{\partial a_{pij}}$. The superscript (n) indicates that the Jacobian is evaluated at $a^{(n)}_{pmn}$.

We can then replace $a^{(0)}_{pij}$ with $a^{(1)}_{pij}$ and find $a^{(2)}_{pij}$, iterating this way we can keep going until we reach a solution that satisfies

$$\sqrt{\sum_{q=0,k=1,l=1}^{N_x-1,N_\perp,N_\parallel} \left|\bar{M}_{qkl}(\{a^{(s)}_{pij}\})\right|^2} \leq \delta_N, \tag{4.54}$$

where δ_N is the desired accuracy and s is the iteration number. In this work, we choose $\delta_N = 10^{-3}$. We also ensure that the solution has converged and is not changing much with every iteration, that is,

$$\sqrt{\sum_{q=1,k=1,l=1}^{N_x,N_\perp,N_\parallel} \left| \frac{h_{pij}^{(n)}}{a_{pij}^{(n)}} \right|^2} \leq \delta_N. \tag{4.55}$$

Due to low values of a_{pij}, condition (4.55) is sometimes difficult to satisfy to the desired precision. The calculation that could be affected most by imprecise values of small a_{pij} is the calculation of the Chodura integral, which is an integral over $f/v_\parallel^2$. Values of a_{pij} smaller than $\Delta v_{\parallel J}^2$, which in our simulations is $10^{-6} - 10^{-10}$, will not contribute much to the integral. We remind the reader that $\Delta v_{\parallel J} = v_{\parallel,J+1}$ is the distance between the first positive velocity grid point and $v_\parallel = 0$ point (see Section 4.2.2 for details). We choose to include in the sum (4.55) only those values for which $|a_{pij}| > \Delta v_{\parallel J}^2$, that is, we allow a_{pij} with $|a_{pij}| > \Delta v_{\parallel J}^2$ to not be fully converged in the sense of (4.55), since the numerical errors make it difficult to satisfy the condition for such small a_{pij}.

To calculate the Jacobian $J_{pijqkl} \equiv \bar{J}_{pijqkl} N_{kl}$ (no summation implied), we differentiate the terms in the definition of M_{qkl}, given in equation (4.49), with respect to a_{pij} to get

$$\begin{aligned} J_{pijqkl} = \int dv_\parallel dv_\perp v_\perp \Bigg(& - \frac{1}{\Delta t(x_q, v_\parallel)^2} \frac{\partial \Delta t(x_q, v_\parallel)}{\partial a_{pij}} \Big[f(x_q, v_\parallel) - f(\xi, \zeta) \Big] \\ & + \frac{1}{\Delta t(x_q)} \Big[\frac{\partial f(x_q, v_\parallel)}{\partial a_{pij}} - \frac{\partial f(\xi, \zeta)}{\partial a_{pij}} \Big] \Bigg) \psi_{kl} - \frac{\partial C_{kl}}{\partial a_{pij}}. \end{aligned} \tag{4.56}$$

The last term in equation (4.56) has already been defined in (4.29).

We proceed to find $\partial \Delta t(x_q, v_\parallel)/\partial a_{pij}$. The travel time of particles $\Delta t(x_q)$ depends on the weights a_{pij} because as the weights change, the distribution function, and so the potential, also changes. We split the derivative into a product of two derivatives using the chain rule,

$$\frac{\partial \Delta t(x_q, v_\parallel)}{\partial a_{pij}} = \frac{\partial \Delta t(x_q, v_\parallel)}{\partial \bar{E}_{q,\sigma}} \frac{\partial \bar{E}_{q,\sigma}}{\partial a_{pij}}, \tag{4.57}$$

where σ is the sign of $v_\parallel$ and $\bar{E}_{q,\sigma}$ was defined in (4.8). The first term on the right hand side of equation (4.57) can be calculated from equations (4.6), (4.13) and (4.9). These equations give

$$\frac{\partial \Delta t(x_q, v_\parallel)}{\partial \bar{E}_{q,\sigma}} = \begin{cases} -2\frac{\Delta t}{\bar{E}_{q,\sigma}} - 2\frac{\partial \zeta}{\partial \bar{E}_{q,\sigma}} \frac{1}{E_{q,\sigma}} & \text{for } q = 0 \text{ and } \sigma = 1, \\ -2\frac{\Delta t}{\bar{E}_{q,\sigma}} + 2\frac{v_\parallel - \zeta}{\bar{E}_{q,\sigma}^2} & \text{for } q = 1 \text{ and } \sigma = -1, \\ -\frac{\Delta t}{\bar{E}_{q,\sigma}} - \frac{\partial \zeta}{\partial \bar{E}_{q,\sigma}} \frac{1}{\bar{E}_{q,\sigma}} & \text{otherwise,} \end{cases} \tag{4.58}$$

where the arguments x_q and $v_\parallel$ have been dropped on the right side of the equations to simplify the expressions. To evaluate the derivative of Δt we used the fact that $v_\parallel$ is independent of $\bar{E}_{i,\sigma}$ since $v_\parallel$ here are the grid point values at which we choose to evaluate the functions. The velocity ζ of the particle at point ξ at time Δt before the particle reaches $(x_q, v_\parallel)$ is given in (4.6). Given these expressions, we get

$$\frac{\partial \zeta}{\partial \bar{E}_{q,\sigma}} = \begin{cases} \frac{\Delta\xi_{q,\sigma}}{\zeta} & \text{for } v_\parallel^2 + 2\bar{E}_{q,\sigma}\Delta\xi_{q,\sigma} > 0, \\ 0 & \text{otherwise.} \end{cases} \tag{4.59}$$

The last derivative in equation (4.57) is found using quasineutrality and adiabatic electrons (equation (3.4) together with the basis expansion of f given by (4.47)),

$$\exp\left(\frac{\phi(x_q)}{T_e}\right) = \int d^3\boldsymbol{v} f(x_q) = \sum_{m=1,n=1}^{N_\perp,N_\parallel} a_{qmn} \int d^3\boldsymbol{v}\psi_{mn}(v_\perp, v_\parallel). \tag{4.60}$$

This gives

$$\frac{\partial \bar{E}_{q,\sigma}}{\partial a_{pij}} = (-\delta_{q+\sigma,p} + \delta_{q,p}) \frac{\int d^3\boldsymbol{v}\psi_{ij}}{n(x_p)\Delta\xi_{q,\sigma}}. \tag{4.61}$$

Equation (4.61), somewhat obviously, states that the potential difference in the region between two grid points only depends on the weights of the distribution at those two points. Equation (4.58) describes how a change in electric field affects the time taken for a particle to travel from ξ to x_q. Just as in Section 4.1, for very low potential differences, we have to implement a zero field solution to avoid inaccuracies due to machine precision. In this case the equations are

$$\frac{\partial \Delta t(x_q, v_\parallel)}{\partial \bar{E}_{q,\sigma}} = \frac{\Delta\xi_{q,\sigma}^2}{v_\parallel^3} \begin{cases} \frac{4}{3} & \text{for } q = 0 \text{ and } \sigma = 1, \\ \frac{2}{3} & \text{for } q = 1 \text{ and } \sigma = -1 \\ 1 & \text{otherwise.} \end{cases} \tag{4.62}$$

The next term in equation (4.56), $\partial f(x_q)/\partial a_{pij}$ can be found from the basis expansion (4.47),

$$\frac{\partial f(x_q)}{\partial a_{pij}} = \psi_{ij}\delta_{q,p}. \tag{4.63}$$

The final term we need to find for equation (4.56) is $\partial f(\xi, \zeta)/\partial a_{pij}$. Recall that ξ and ζ are functions of x, $v_\parallel$, and the potential. The basis expansion of $f(\xi, \zeta)$ is given by

$$f(\xi, \zeta) = \sum_{k,l} a_{rkl}\psi_{kl}(\zeta), \tag{4.64}$$

where location r is the grid point such that $x_r = \xi$, and the $v_\perp$ dependence has been suppressed. Differentiating this expression gives

$$\frac{\partial f(\xi,\zeta)}{\partial a_{pij}} = \delta_{pr}\psi_{ij}(\zeta) + \sum_{k,l} a_{rkl}\frac{\partial \psi_{kl}(\zeta)}{\partial a_{pij}}. \tag{4.65}$$

We use the chain rule to find the derivative in the last term,

$$\frac{\partial \psi_{kl}(\zeta)}{\partial a_{pij}} = \frac{\partial \psi_{kl}(\zeta)}{\partial \zeta}\frac{\partial \zeta}{\partial \bar{E}_{q,\sigma}}\frac{\partial \bar{E}_{q,\sigma}}{\partial a_{pij}}. \tag{4.66}$$

Here q is the grid point from which we follow back the characteristic and where the Jacobian (4.56) is evaluated. The position ξ is affected by the change in the coefficients a_{pij} because these coefficients change the electric field between x_q and x_p, which is given by $\bar{E}_{q,\sigma}$. The derivatives $\partial\zeta/\partial\bar{E}_{q,\sigma}$ and $\partial\bar{E}_{q,\sigma}/\partial a_{pij}$ have already been evaluated in equations (4.59) and (4.61), respectively. The derivatives of the basis functions with respect to ζ depend on the basis functions chosen. In this work we use quadratic Lagrange polynomials.

With (4.57), (4.63), (4.65) and (4.29), we can find the Jacobian given in (4.56). Using the Jacobian, the boundary conditions and an initial guess of a_{pij}, we can use Newton's method to converge to a solution that solves the drift kinetic equation coupled with quasineutrality and adiabatic electrons.

4.4.1 Forcing the function to be quadratic at $x = 0$ and $v_\parallel = 0$

We have to be careful at the $v_\parallel = 0$ boundary at the MPE to avoid large errors. Since the distribution function is $f(x = 0, v_\parallel = 0) = 0$, the coefficient $a_{kJ} = 0$ is fixed. Inside the first element, the distribution function is approximated by $f(x = 0, 0 < v_\parallel < v_{\parallel J+2}) = \sum_m (a_{m,J+1}\psi_{m,J+1} + a_{m,J+2}\psi_{m,J+2})$, where the sum is over the $v_\perp$ indices m. We choose the grid points inside the elements to be evenly spaced ($v_{\parallel J+2} = 2v_{\parallel J+1}$). Then, we can express the basis functions in this region in terms of $v_\parallel$ as

$$\psi_{J+1}(v_\parallel) = -4\frac{v_\parallel(v_\parallel - v_{\parallel J+2})}{v_{\parallel J+2}^2}, \qquad \psi_{J+2}(v_\parallel) = 2\frac{v_\parallel(v_\parallel - v_{\parallel J+1})}{v_{\parallel J+2}^2}. \tag{4.67}$$

As a result,

$$f(x = 0, 0 < v_\parallel < v_{\parallel J+2}) = \sum_m \left(K_m \frac{v_\parallel^2}{v_{\parallel J+2}^2} + W_m \frac{v_\parallel}{v_{\parallel J+2}} \right), \tag{4.68}$$

where

$$K_m = 2a_{m,J+2} - 4a_{m,J+1}, \qquad W_m = -a_{m,J+2} + 4a_{m,J+1}. \tag{4.69}$$

As discussed in Section 4.2.2, the resolution in the element that has $v_\parallel = 0$ is $v_{\parallel J+2} < v_c$, where (still in normalised units) $v_c^2 \equiv 2\Delta\phi_0$ and $\Delta\phi_0 = \phi(x_1) - \phi(0)$. This means that the characteristics in this element come from the MPE, that is, $\xi = 0$ and $\zeta = -v_\parallel$, where the distribution function is zero. Then, from equation (4.13), we have

$$\Delta t = \frac{16x_1}{3v_c^4} v_\parallel^3. \tag{4.70}$$

With this result in the first element, equation (4.20) simplifies to

$$\int_k dv_\perp v_\perp \int_0^{v_{J+2}} dv_\parallel \frac{3v_c^4}{16x_1 v_\parallel^3} f(x, v_\perp, v_\parallel)\psi_{kl} = -\int_k dv_\perp v_\perp \int_0^{v_{J+2}} dv_\parallel \nabla_v \psi_{kl} \cdot \mathbf{\Gamma}[f](x, v_\perp, v_\parallel). \tag{4.71}$$

The k under the integral indicates that the integral is over the volume in which $\psi_k(v_\perp)$ is not zero. The integrals in equation (4.71) have to be computed for $\psi_{k,J+1}(v_\parallel)$ and $\psi_{k,J+2}(v_\parallel)$. Taking $l = J+1$, writing the basis function as a product of the basis function in $v_\parallel$ and a basis function in $v_\perp$ and substituting expansion (4.68), the left hand side of equation (4.71) is proportional to

$$\sum_m \int_k dv_\perp v_\perp \psi_k(v_\perp)\psi_m(v_\perp) \int_0^{v_{\parallel J+2}} \frac{dv_\parallel}{v_{\parallel J+2}^2} \left[K_m \frac{\psi_{J+1}(v_\parallel)}{v_\parallel} + W_m \frac{\psi_{J+1}(v_\parallel) v_{\parallel J+2}}{v_\parallel^2} \right]. \tag{4.72}$$

The integrals in $v_\parallel$ can be done exactly by substituting (4.67), which gives

$$\int_0^{v_{\parallel J+2}} dv_\parallel \frac{\psi_{J+1}(v_\parallel)}{v_\parallel} = 2, \tag{4.73}$$

$$\int_\delta^{v_{\parallel J+2}} dv_\parallel \frac{\psi_{J+1}(v_\parallel) v_{\parallel J+2}}{v_\parallel^2} = 4\left(-1 + \frac{\delta}{v_{\parallel J+2}} + \ln\left(\frac{v_{\parallel J+2}}{\delta}\right)\right). \tag{4.74}$$

Taking $\delta \to 0$, we see that integral (4.74) diverges. Since the right hand side of equation (4.71) is finite, this implies that $W_m = 0$ for all m and thus $a_{m,J+2} = 4a_{m,J+1}$. The distribution function in the first element is then $f(x = 0, 0 < v_\parallel < v_{\parallel J+2}) = \sum_m K_m v_\parallel^2$. This also ensures that the distribution function is positive in this region as long as $a_{m,J+2} > 0$. The lack of linear terms in $v_\parallel$ in this element also allows the kinetic Chodura condition (3.5) to be satisfied, as any linear behaviour would cause a divergence in the $f/v_\parallel^2$ integral.

Unfortunately, due to the Gaussian quadrature method that we are using for integration, the logarithmic divergence in the integral is not well captured. The value of the integral (4.74) for 4 quadrature points is ~ 10 and increases slowly as more points are added. This means that we expect $W_m \sim K_m/5$, which is small, but not zero. We choose to adjust the method by fixing the values of $a_{k,J+1} = a_{k,J+2}/4$ and thus $W_m = 0$. We do this by defining a new basis function

$$\hat{\psi}_{J+2}(v_\parallel) \equiv \begin{cases} \frac{1}{4}\psi_{J+1} + \psi_{J+2}, & \text{for } v_\parallel < v_{\parallel J+2} \\ \psi_{J+2}, & \text{for } v_\parallel > v_{\parallel J+2}. \end{cases} \tag{4.75}$$

At $x = 0$, instead of solving the system of equations for all ψ_j with $j > J$, we solve it for ψ_j for $j > J+2$ and for $\hat{\psi}_{J+2}$. This means that when solving (4.51), we have different values that the indices q, i and j can take. In all cases $i = 1, ..., N_\perp$. For the boundary at infinity $q = N_x - 1$, we solve the equation for $i = 1, ...J-1$, as we do not evolve the distribution function at $v_\parallel \geq 0$. For $q = 1, .., N_x - 2$, we solve in the entire $v_\parallel$ space $j = 1, ..., N_\parallel$. At the MPE, $q = 0$, we solve $j = J+3, ..., N_\parallel$, and for $j = J+2$, we solve a modified equation $\hat{M}_{0,i,J+2} = 0$, where

$$\hat{M}_{0,i,J+2} = \frac{1}{4}\bar{M}_{0,i,J+1} + \bar{M}_{0,i,J+2}. \tag{4.76}$$

This also means that for $q = 0$, the Jacobian (4.56) is solved for $j, l > J+3$. But for $q = 0$ and $j = J+2$ and/or $l = J+2$, the Jacobian has to be modified to the following values

$$\begin{aligned} \hat{J}_{0,i,J+2,0,i,J+2} &= \frac{1}{16}J_{0,i,J+1,0,i,J+1} + \frac{1}{4}J_{0,i,J+1,0,i,J+2} \\ &\quad + \frac{1}{4}J_{0,i,J+2,0,i,J+1} + J_{0,i,J+2,0,i,J+2}, \end{aligned} \tag{4.77}$$

$$\hat{J}_{0,i,J+2,0,i,j>J+2} = \frac{1}{4}J_{0,i,J+1,0,i,j>J+2} + J_{0,i,J+2,0,i,j>J+2}, \tag{4.78}$$

$$\hat{J}_{0,i,j>J+2,0,i,J+2} = \frac{1}{4}J_{0,i,j>J+2,0,i,J+1} + J_{0,i,j>J+2,0,i,J+2}. \tag{4.79}$$

Note that the result $W_m = 0$ relies on using the $\hat{\phi} \sim x^{1/2}$ dependence. For a general $\hat{\phi} \sim x^\beta$ dependence, the travel time (4.70) scales as $\Delta t \sim v_\parallel^{-1+2/\beta}$. Therefore, the integral given by (4.72) has the form

$$\sum_m \int_k dv_\perp v_\perp \psi_k(v_\perp)\psi_m(v_\perp) \int_0^{v_{\parallel J+2}} \frac{dv_\parallel}{v_{\parallel J+2}^2} \left[K_m \frac{\psi_{J+1}(v_\parallel)}{v_\parallel^{-3+2/\beta}} + W_m \frac{\psi_{J+1}(v_\parallel) v_{\parallel J+2}}{v_\parallel^{-2+2/\beta}} \right]. \tag{4.80}$$

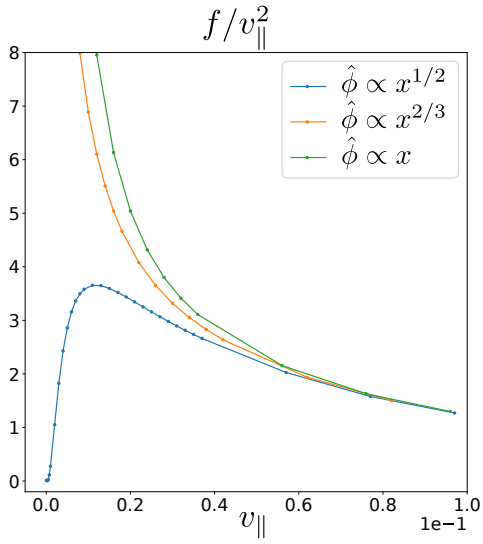

Figure 4.9: The integrand of the Chodura condition $f/v_\parallel^2$ at $v_\perp = 0$ for $\Delta_s = 0.1$ and $T_e = 0.5$, and potential dependences at the MPE $\hat{\phi} \propto x^{1/2}$, $\hat{\phi} \propto x^{2/3}$, $\hat{\phi} \propto x$. The $\hat{\phi} \propto x^{1/2}$ curve is the only one that does not blow up at $v_\parallel = 0$. The $\hat{\phi} \propto x^{1/2}$ plot also has $K_0 \approx 0.01$, which agrees with our expectation that K_0 should approach 0 if the function decays exponentially fast.

The part of the integrand multiplied by W_m diverges for $\beta \leq 1/2$. As discussed, this divergence forces $W_m = 0$ and thus ensures that the distribution function is purely quadratic in this first element. This means that we can only expect the kinetic Chodura condition to be recovered by the simulation if $\beta \leq 1/2$. This is the reason why we interpolated ϕ using $x^{1/2}$ between the MPE at $x = 0$ and the next grid point x_1.

We argued in Section 3.2.1 that the distribution function is exponentially small at low velocities. This means that the constant K_m should approach zero for well resolved simulations. Figure 4.9 shows plots of $f/v_\parallel^2$ for $\Delta_s = 0.1$ and $T_e = 0.5$ for different choices of potential in the region near the MPE, $0 < x < x_1$. We choose to compare the different potential interpolations $\hat{\phi} \propto x^{1/2}$, $\hat{\phi} \propto x^{2/3}$ and $\hat{\phi} \propto x$. These different interpolations result in different values of (4.49) and (4.56) since the trajectories (specifically ζ, ξ and Δt) of the particles in the region $0 < x < x_1$ are affected. We see that the curves diverge at $v_\parallel = 0$ for the $\hat{\phi} \sim x^{2/3}$ and $\hat{\phi} \sim x$ dependencies. Note that if high enough resolution in $v_\parallel$ is chosen, $\hat{\phi} \sim x^{1/2}$ also has a very small constant $K_0 \approx 10^{-2}$ as expected from the fact that the distribution function should be exponentially small near $v_\parallel = 0$.

4.4.2 Position space grid

Since the Jacobian is an array whose size scales as $N_x^2 N_\perp^2 N_\parallel^2$, we can run into computer memory issues when trying to compute it. For some of the velocity grid resolutions used (for more than ~ 95 grid points in $v_\parallel$), we were not able to run the simulation with all the x points coupled for $N_x \gtrsim 50$. For higher resolution runs, we split the x domain into multiple regions of size $n_x < N_x$. The grid points at the edge of the regions overlap over two points. We first apply Newton's method to the region that includes the $x = 0$ boundary by inventing a boundary condition for $v_\parallel > 0$ at the artificial boundary $x = x_{n_x}$. We then move on to the next region so that the boundary conditions are at $x = x_{n_x-1}$ for $v_\parallel < 0$ and $x = x_{2n_x-1}$ for $v_\parallel > 0$. There is an overlap of two points between the two regions. We continue doing so until we solve the equation for the region containing the final boundary point at $x = x_{N_x-1}$, where we apply the real, Maxwellian, boundary condition. A simple division of the grid for $N_x = 7$ and $n_x = 4$, with two points overlapping is shown in Figure 4.10. After solving Newton's method in each region, we go back to $x = 0$ and repeat the process. We use the functions calculated in the first step as the initial guesses and boundary conditions. We will call going through the entire collisional layer once a single "step". We continue this for multiple steps until the distribution function stops changing; that is, equation (4.51) is solved. More steps are required to achieve convergence for smaller n_x. Figure 4.11 shows the differences of the distribution function at the MPE and the densities for different values of n_x for the case where $N_x = 48$. For $n_x = 10$ and 20, we completed 20 steps through the entire domain, whereas for $n_x = 40$ we completed only 4, as the solution converged quickly. Even though some accuracy is lost by dividing the grid up in the described way, the differences are of size 10^{-3} at most and do not affect the potential profile much. The effects could become important when considering the kinetic Chodura condition, since a small error at small $v_\parallel$ is increased by the small denominator. This is also plotted in Figure 4.11. The errors in $f/v_\parallel^2$ at the smallest $v_\parallel$ are $\sim 10^{-5}$, while the absolute value of $f/v_\parallel^2$ there is $\sim 10^{-1}$. Note that in the simulation shown the distribution function is negative near $v_\parallel = 0$. This is one of the very few simulations with such behaviour, but, as we argue next, this slight negativity does not seem to have a measurable effect. The actual value of f is only $\sim -10^{-8}$ and is a result of numerical errors and the finite precision of the Newton's method solver. However, when

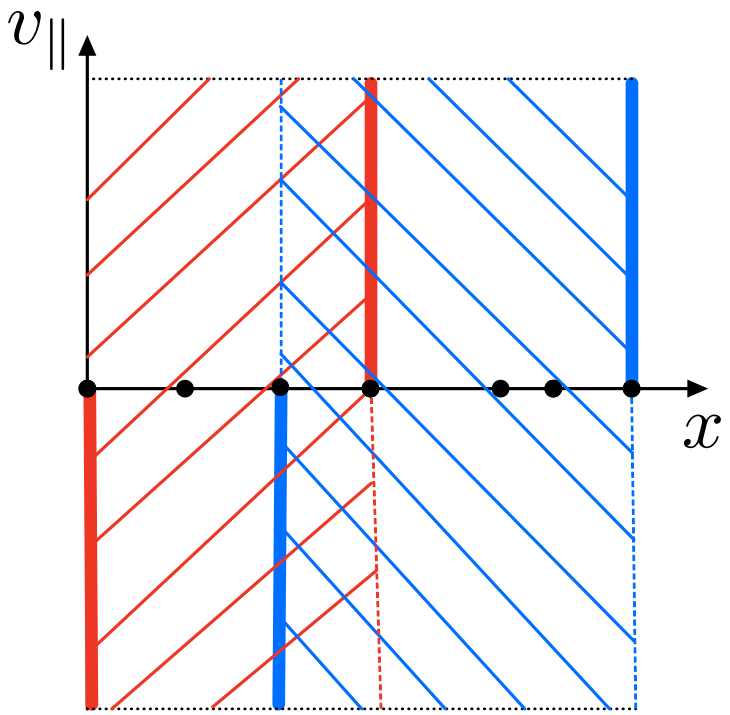

Figure 4.10: A sketch of the phase space grids illustrating the division of x space into smaller subsets. The thin horizontal dotted black lines indicate boundaries of $v_\parallel$ space. In this example there are $N_x = 7$ grid points in position space. The region is divided into two subregions of $n_x = 4$, The diagonal red and blue dashes indicate the two subregions. The vertical dashed lines indicate the boundaries in x of each region. In each region we solve equation (4.51). The boundary conditions are given by the values of the distribution function at the velocities highlighted by the thick vertical lines. We first solve the region that includes $x = 0$ (the red region). After solving the red region and updating the grid point values at all $x_0 \leq x \leq x_4$, we solve the blue region. This is one "step" in the simulation. Boundary conditions for one region are not boundary conditions for the other region and thus change from step to step. The only fixed boundary conditions are at $x = 0$ and $v_\parallel < 0$, and at $x = x_6$ and $v_\parallel > 0$. Since the blue region updates values of the distribution function at $x = x_3$ and $x = x_4$, after this update the red region might no longer satisfy the equation (4.51) and thus we solve it again. We keep stepping through the region in such a way until the distribution function stops changing and equation (4.51) is satisfied in each region.

divided by a small value of $v_\parallel$, this becomes $\sim 10^{-1}$. This has no effect when taking moments, though, since the region over which the distribution function is negative is small in $v_\parallel$ space. The difference between the distribution function with $n_x = 10$ and $n_x = N_x = 48$ at different steps is shown in the top right plot of Figure 4.11.

The choice of total number of points N_x depends on the highest resolution Δx_0 and the size of the x grid x_{N_x-1}. We expect the gradients in x to be largest near $x = 0$ and so the resolution is highest near the MPE. We also expect the potential here to scale as $\sim x^{1/2}$ (we show this in Section 3.2.3). Therefore, for the first few points near $x = 0$, we set the resolution to be

$$\Delta x_i = \Delta x_0((i+1)^2 - i^2). \tag{4.81}$$

On a grid spaced like this, a function $y = x^{1/2}$ would change by an equal amount as we moved from grid point x_i to x_{i+1}, that is, $y_{i+1} - y_i =$ constant. We keep this spacing for five points and then instead of continuing to increase Δx_i every grid point, we keep the resolution at $\Delta x_i = 10\Delta x_0$ for a few points and then we increase the resolution in steps until the resolution becomes $\Delta x = 20$. In Figure 4.12 the total potential drop across the layer normalised to the converged value of the potential drop, $(\phi_{N_x-1} - \phi_0)/\Delta\phi_{ref}$, is plotted against the resolution at the MPE Δx_0 for $\Delta_s = 0.01, 0.1$ and $T_e = 0.5$. We see that the effect of resolution is small. In Section 5.4, we show that for small Δ_s (or high T_e), the resolutions used ($10^{-7} \leq \Delta x_0 \leq 10^{-3}$) give the kinetic Chodura condition at the MPE with small errors (a few percentage points). However, for large Δ_s (or small T_e), the errors in the kinetic Chodura condition are large even at $\Delta x_0 = 10^{-7}$ and recovering the condition to high accuracy might not be possible with this code.

The maximum value of x, x_{N_x-1}, determines how far the "infinity" region (the CLE) is from the MPE ($x = 0$). We want it to be large enough that any effects from the wall are negligible. We expect that simulations with a large mean flow at infinity will not need a large x_{N_x-1} as the effect of the wall boundary becomes negligible quickly as we move away from the wall (see equation (2.52)). Plots of the potential as a function of x for $\Delta_s = 0.01, 0.1, 1.0$ and $T_e = 0.5$ are shown in Figure 4.13. Figure 4.13 shows that if a large enough x_{N_x-1} is chosen, the wall has a negligible effect on the region at infinity. The total potential drop throughout the full simulation region is not affected much by this parameter. Comparing the potential drop for $x_{N_x-1} = 880$ to the potential drop for

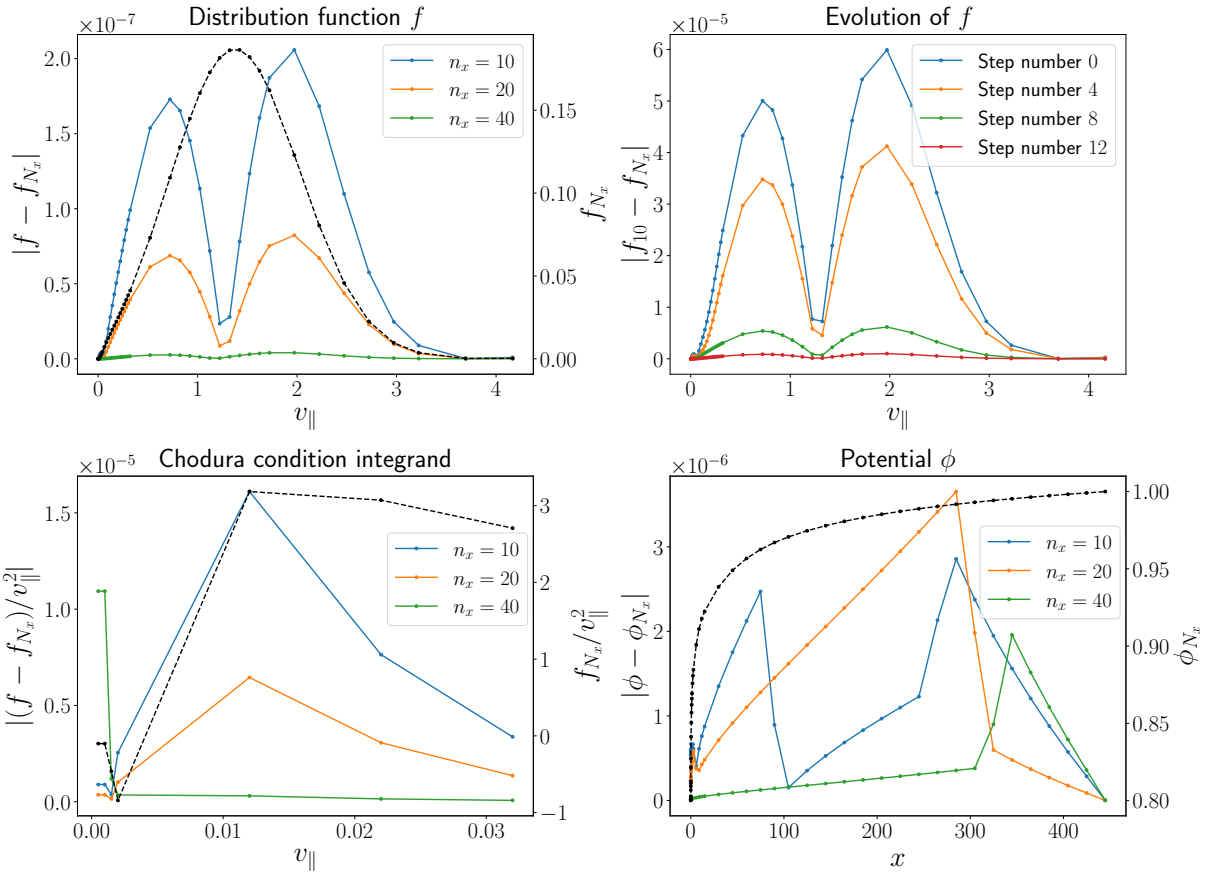

Figure 4.11: The y axes on the right of the subplots correspond to the black dashed line and indicate the value of the variable when $n_x = N_x$, where $N_x = 48$; that is, equation (4.51) is solved for all the x points together. The left hand axis corresponds to the differences between the plotted variables obtained using $n_x < N_x$ and $n_x = N_x$. The values at the final time step are compared. The number of time steps taken for each simulation to converge depends on n_x. **Top left**: Distribution function differences at $x = 0$, $v_\perp = 0$. **Top right**: The difference between f obtained with $n_x = 10$ (labelled f_{10}) and $n_x = N_x$ (labelled f_{N_x}). Each line represents a step in the evolution of the $n_x = 10$ simulation (recall that for $n_x = N_x$ the equations are solved in a single step). We see that the $n_x = 10$ curve approaches the fully coupled solution as we evolve it. **Bottom left**: Integrand for the kinetic Chodura condition $f/v_\parallel^2$ at $x = 0$, $v_\perp = 0$. **Bottom right**: Potential as a function of x.

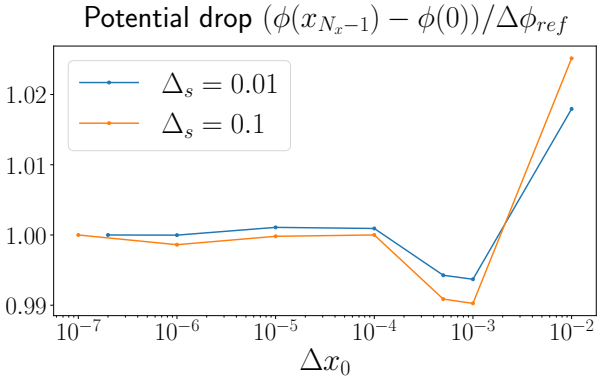

Figure 4.12: Drop in potential across the layer as a function of Δx_0 for $\Delta_s = 0.01, 0.1$, normalised to $\Delta\phi_{ref}$, which is the drop in potential for the simulation with the smallest Δx_0. The effect of Δx_0 on the potential drop is small, note the log scale on the x axis.

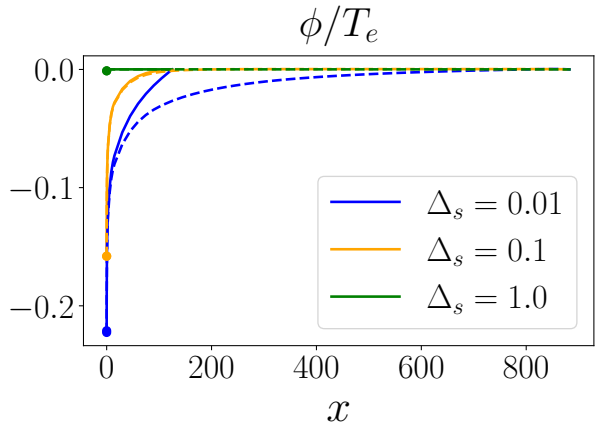

Figure 4.13: Potential ϕ/T_e for $T_e = 0.5$ as a function of x. Different colours indicate different Δ_s. Solid lines have $x_{N_x-1} = 110$ and dashed lines have $x_{N_x-1} = 880$. The values at $x = 0$ are marked by a dot, and show that the total potential drop is not affected much by x_{N_x-1}. The perturbation extends further from the wall for small Δ_s and the exact profile at large x can be difficult to resolve for small values of Δ_s (see Section 2.3).

$x_{N_x-1} = 110$, the difference is only $\sim 0.5\%$ for $\Delta_s = 0.01$ and $\sim 0.005\%$ for $\Delta_s = 1$. This means that if x_{N_x-1} is chosen too small, the potential profile might not be accurate, but the total potential drop will still be captured well.

Capturing the profile with very high accuracy is important when determining the length scale of perturbations of the distribution function at large x, as discussed in Section 2.3. In that case, for small values of Δ_s, it becomes difficult to capture the appropriate behaviour at large x without making x_{N_x-1} very large. For $\Delta_s = 0.01$, the largest box size we used was $x_{N_x-1} = 3000$, an even larger value would be needed for smaller Δ_s.

Chapter 5

Results

In this chapter we overview the results of our simulations. In Section 5.1 we see how well the potential scaling $\hat{\phi} \sim x^{1/2}$, derived in Section 3.2.3, is captured by the numerical simulations. In Section 5.2 we describe how the total potential drop depends on Δ_s and T_e. In Section 5.3 we show the distribution functions obtained at the MPE for different boundary conditions at $x \to \infty$ and use these results to find the distribution function at the wall using a magnetic presheath and Debye sheath solver `GYRAZE` [1]. In Section 5.4, we show how well the functions at the MPE satisfy the kinetic Chodura condition. We continue using normalised quantities throughout this chapter.

5.1 Potential scaling near $x = 0$

In this section we use the code described in Chapter 4 to check how well the potential scaling $\hat{\phi} \sim x^{1/2}$, derived in Section 3.2.3, is captured by the simulations. In Figure 5.1 we plot $\hat{\phi}/T_e$ against x on a log-log scale for $\Delta_s = 0.01, 1.0$ and $T_e = 0.5$. Here we use $\hat{\phi} \propto x^{1/2}$ to interpolate the potential between the MPE at $x = 0$ and $x = x_1$, the grid point next to the MPE. The scaling $\sim x^{1/2}$ fits both curves well for small x. The scaling is not true at large x where the field is weak, but holds up to $x \sim 1$. There is a slight deviation at the smallest x. We believe this is due to numerical imprecision at very small x and $\hat{\phi}$.

Figure 5.2 shows $\hat{\phi}$ as a function of x for three different simulations, all with $\Delta_s = 0.1$ and $T_e = 0.5$, but with different interpolation for ϕ between $x = 0$ and x_1. We use $\hat{\phi} \propto x^{\beta}$. As a reminder, $\beta = 1/2$ has to be enforced in the code to capture the expected behaviour of the ion distribution function at the MPE (see Section 4.4.1). The chosen

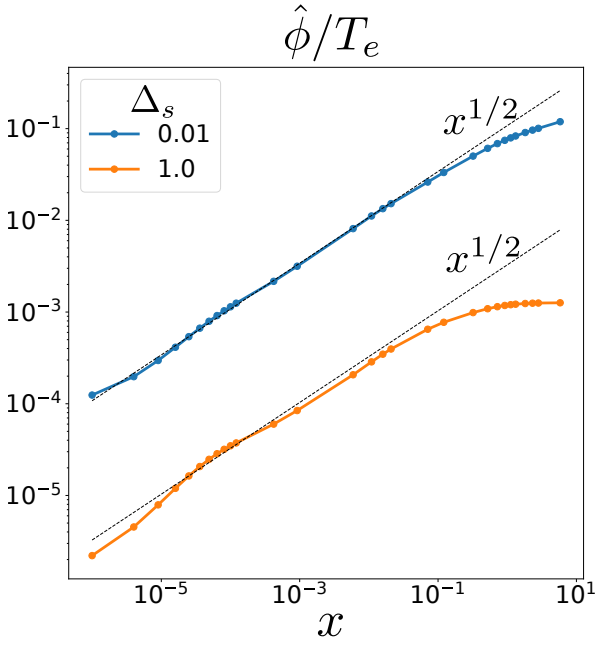

Figure 5.1: Normalised potential difference $\hat{\phi}/T_e$ between the MPE ($x = 0$) and x against x on a log-log scale for $\Delta_s = 0.01, 1.0$ and $T_e = 0.5$. The black dashed lines are the expected $x^{1/2}$ scaling derived in Section 3.2.2. The predicted scaling fits both curves well until very close to the wall, where the solution deviates from the predicted scaling slightly. We believe that this is due to numerical errors.

potential scaling affects the characteristic equations via the ξ and ζ terms defined in (4.5) and (4.6), respectively. In Figure 5.2 we choose to compare three different interpolations: $\hat{\phi} \propto x^{1/2}$, $\hat{\phi} \propto x^{2/3}$ (this is the scaling for which all the terms in the drift kinetic equation (3.3) are of the same order) and $\hat{\phi} \propto x$. We find that the potential profile is not affected much by the choice of β. However, as discussed in Section 4.4.1 and shown in Figure 4.9, for $\beta = 2/3$ and $\beta = 1$ the kinetic Chodura condition is not satisfied and thus $\beta = 1/2$ is the appropriate choice. The curves seem to follow the expected $x^{1/2}$ scaling well in the $x \lesssim 0.1$ region. At the boundary point next to the wall, $x_1 = 10^{-6}$, the curves have slightly different values, which is to be expected due to different potential scalings imposed in the region next to it.

5.2 Potential drop across the collisional layer

The numerical solution to the collisional layer allows us to find the relationship between the potential drop across the layer and the parameters of the incoming distribution function at the $x = x_{N_x-1}$ boundary – specifically, the mean flow $u_{\parallel\infty}$ and the temperature ratio T_e. The relationship between these quantities is discussed in this section.

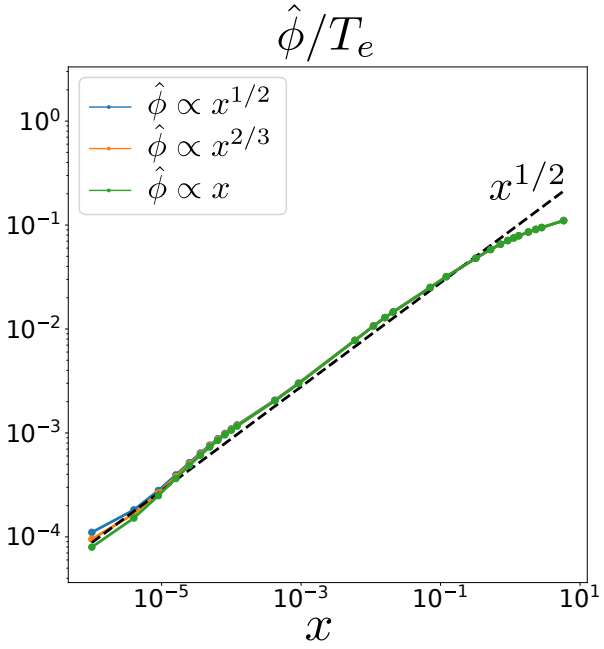

Figure 5.2: Normalised potential difference $\hat{\phi}/T_e$ between the MPE ($x = 0$) and x against x, for $x_1 \leq x < 1$, on a log-log scale for $\Delta_s = 0.1$ and $T_e = 0.5$. The three different curves represent the different interpolations for the potential in $0 < x < x_1$. The black dashed line is $\hat{\phi} \propto x^{1/2}$ for all x. We see that the potential scaling is independent of the interpolation in the $0 < x < x_1$ region.

The right plot in Figure 5.3 shows the total potential drop across the layer $-\phi(x = 0)$ for a range of Δ_s and T_e. For a fixed temperature ratio T_e, the potential drop decreases with increasing Δ_s. A larger Δ_s means that the incoming Maxwellian has fewer particles near $v_\parallel = 0$. These are the particles that need to be accelerated through the collisional layer to ensure that the kinetic Chodura condition is satisfied. As a result the potential drop is smaller for larger Δ_s.

The dependence on T_e is less straightforward. From the left plot of Figure 5.3, we see that the density drop, or $-\phi(x = 0)/T_e$, is largest and finite for $T_e \to 0$, indicating $-\phi(x = 0) \sim T_e$ in this limit. We also note that $-\phi(x = 0)/T_e$ decreases monotonically as T_e increases. We will now argue that this is to be expected.

The distribution function at the boundary at $x = x_{N_x-1}$ integrated over the $v_\perp$ coordinate is a Maxwellian, given by $\pi^{-1/2} \exp\big(-(v_\parallel - u_{\parallel\infty})^2\big)$, where we have integrated over the $v_\perp$ coordinate. All the particles with $v_\parallel < 0$ at $x = x_{N_x-1}$ leave the system, as there is no electric field here that could turn them around back towards the wall. This means

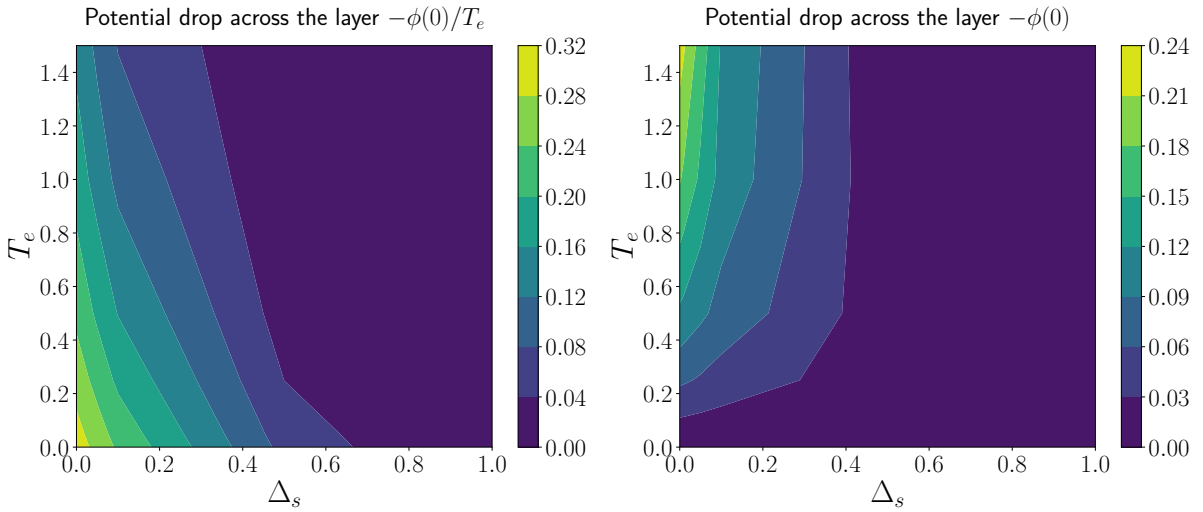

Figure 5.3: The potential drop across the layer for a range of values of Δ_s and T_e. The left plot shows the ratio of potential drop to electron temperature $-\phi(x=0)/T_e$. The right one shows $-\phi(x=0)$ (remember the variables are normalised to ion temperature T_∞).

that the largest number of particles that could reach the wall is

$$n_+ = \int_0^\infty f_M dv_\parallel = \frac{1}{2}(1+\mathrm{erf}(u_{\parallel\infty})). \tag{5.1}$$

This is a monotonically increasing function in $u_{\parallel\infty}$. At all x, the collisions diffuse the particles with $v_\parallel > 0$ into the $v_\parallel < 0$ region, this refills the distribution function at negative velocities at $x = x_{N_x-1}$, thus reducing the particle density reaching the wall. Therefore, n_+ gives the maximum number of particles that could reach the wall, and thus the minimum potential drop. Using quasineutrality, we find

$$-\frac{\phi(x=0)}{T_e} \lesssim \ln(n_+). \tag{5.2}$$

To see how good this estimate is we take the limit $T_e \to 0$ and $\Delta_s \to 0$. Then, $u_\parallel = \sqrt{5/6}$ and equation (5.2) gives

$$-\frac{\phi(x=0)}{T_e} \sim -\ln(n_+) \approx 0.1. \tag{5.3}$$

The value found numerically is $-\phi(x=0)/T_e \approx 0.3$. The result is of the expected order of magnitude, but clearly, the collisions have an effect, which our estimate does not take into account.

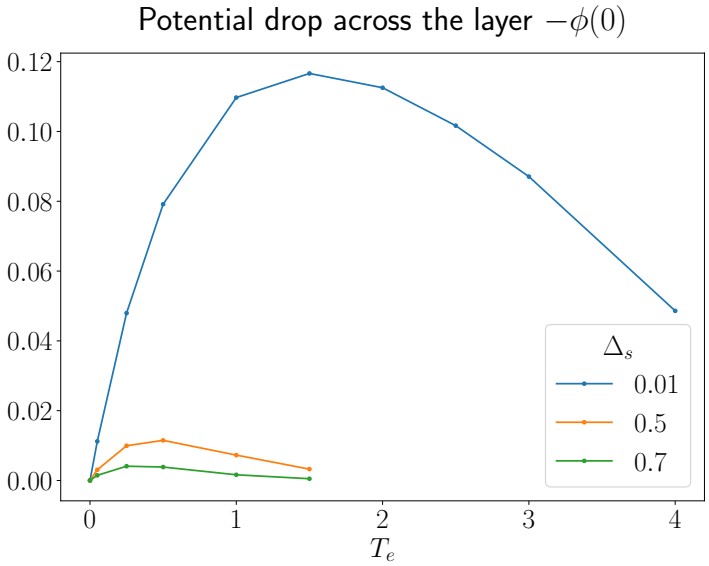

Figure 5.4: The total potential drop across the layer $-\phi(x = 0)$ (normalised to ion temperature T_∞) as a function of T_e for $\Delta_s = 0.1, 0.5, 0.7$. The total potential drop is zero at $T_e = 0$ and approaches zero as $T_e \to \infty$. It has a maximum at $T_e \sim 1$. The maximum occurs earlier for larger Δ_s.

As $T_e \to \infty$, the mean flow $u_{\parallel\infty}$ must also be large because $u_{\parallel\infty} \geq \sqrt{5/6 + T_e}$. Thus, equation (5.1), to lowest order in $1/T$, gives

$$n_+ \simeq 1 - \frac{1}{2\sqrt{\pi}} \frac{\exp(-(1+\Delta_s)^2(5/6+T_e))}{(1+\Delta_s)\sqrt{T_e}}. \tag{5.4}$$

Plugging the expansion (5.4) into (5.2) gives

$$-\phi(x=0)/T_e \sim \exp\big(-(1+\Delta_s)^2(5/6+T_e)\big)/\sqrt{T_e}, \tag{5.5}$$

and thus $-\phi(x = 0) \to 0$. This is to be expected at large T_e. Similarly to the case of large Δ_s, there are very few particles near $v_\parallel = 0$ that need to be accelerated to satisfy the kinetic Chodura condition at $x = 0$ and thus only a small potential drop is required. Thus there must be a maximum of potential drop somewhere between $T_e = 0$ and $T_e \to \infty$ as the potential drop at these values is zero. This agrees with numerical results. Figure 5.4 shows that the potential drop has a maximum at $T_e \sim 1$, and decreases for larger T_e.

5.3 Distribution function at $x = 0$

For numerical solutions that satisfy the kinetic Chodura condition at the MPE (see Section 5.4 for why this is not always true) the model can be coupled to a magnetic presheath and Debye sheath solver to determine the potential drop across the magnetic presheath

and the Debye sheath, and the ion distribution function at the wall. This is useful for calculating the sputtering yield, which depends on the kinetic energies of the ions hitting the wall E and the angles θ they make with the wall [47].

The ion distribution functions at the MPE as well as the integrand of the kinetic Chodura integral, $f_{MPE}/v_\parallel^2$, for $T_e = 0.5$ and a range of $0.01 \leq \Delta_s \leq 0.5$, and for $\Delta_s = 0.1$ and a range of $0.5 \leq T_e \leq 2.0$, are shown in Figure 5.5. The plots in Figure 5.5 show that $f_{MPE}/v_\parallel^2$ develops a peak. The peak is highest at large values of Δ_s and small values of T_e. We proceed to argue that these scalings can be expected from the kinetic Chodura condition (3.5).

We can divide the integration region in the kinetic Chodura condition into two regions by introducing the characteristic velocity scale $v_w \ll u_\parallel$, which represents the width of the peak in $f_{MPE}/v_\parallel^2$

$$\int_0^{v_w} \frac{f_{MPE}}{v_\parallel^2} d^3\boldsymbol{v} + \int_{v_w}^{\infty} \frac{f_{MPE}}{v_\parallel^2} d^3\boldsymbol{v} = \frac{n_0}{T_e}. \tag{5.6}$$

The density at the MPE, n_0, ranges from $\sim 0.8-1$ for all the values of T_e and Δ_s and does not contribute significantly to the scaling. The scaling of the second integral in equation (5.6) can be found by noticing that the maximum of f_{MPE} is approximately at $u_\parallel \gg v_w$ giving

$$\int_{v_w}^{\infty} \frac{f_{MPE}}{v_\parallel^2} d^3\boldsymbol{v} \sim \frac{1}{u_\parallel^2} = \frac{1}{(T_e + 5/6)(1+\Delta_s)^2}. \tag{5.7}$$

At small T_e, the bulk integral (5.7) is finite and independent of T_e. Therefore, the first integral in (5.6) (and so the height of the peak in $f_{MPE}/v_\parallel^2$) becomes large to balance the right hand side of the kinetic Chodura condition, which is $\sim 1/T_e$.

For fixed T_e, the right hand side of (5.6) is a constant (up to a small variation in n_0). A large Δ_s corresponds to the distribution function f_{MPE} having a peak at large $v_\parallel$, as can be seen from the top left plot in Figure 5.5 and equation (5.7). Thus the bulk integral contributes little to the total integral. To maintain the overall value of the full integral constant, the size of the peak near $v_\parallel = 0$ must increase with increasing Δ_s.

From our simulations we obtain distribution functions at the MPE, which can then be used as an input to a magnetic presheath and Debye sheath solver `GYRAZE`, described in [1], to find the distribution functions at the wall as a function of particle's energy and angle

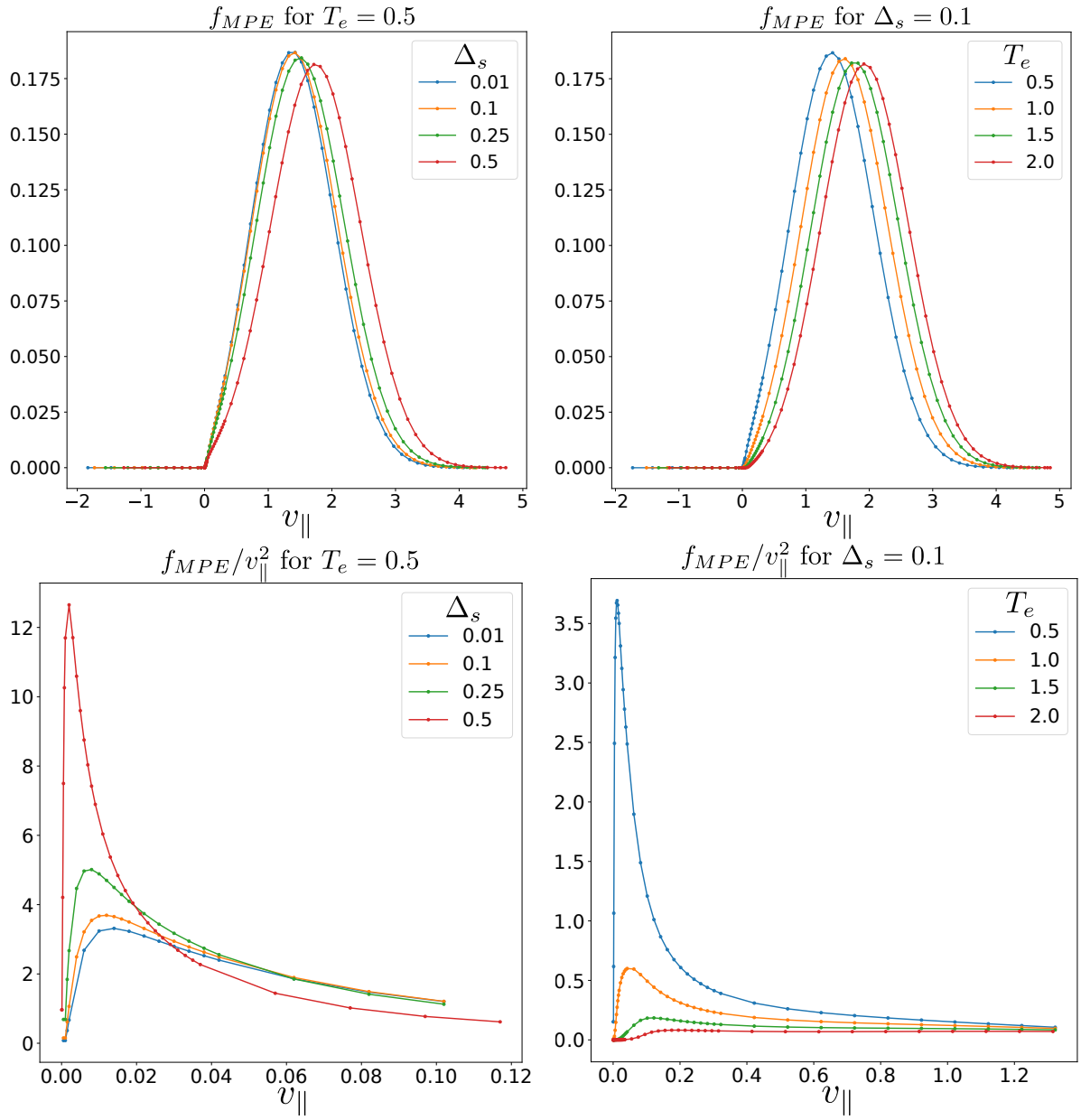

Figure 5.5: **Top left:** The ion distribution functions at the MPE at $v_\perp = 0$ for a range of Δ_s and $T_e = 0.5$. **Bottom left:** The same ion distribution function divided by $v_\parallel^2$ for fixed $T_e = 0.25$. At larger Δ_s the peak is larger and occurs at smaller $v_\parallel$. **Top right:** The ion distribution functions at the MPE for a range of T_e and $\Delta_s = 0.1$. **Bottom right:** The same distribution function divided by $v_\parallel^2$ at fixed $\Delta_s = 0.1$. At smaller T_e the peak is larger and occurs at smaller $v_\parallel$

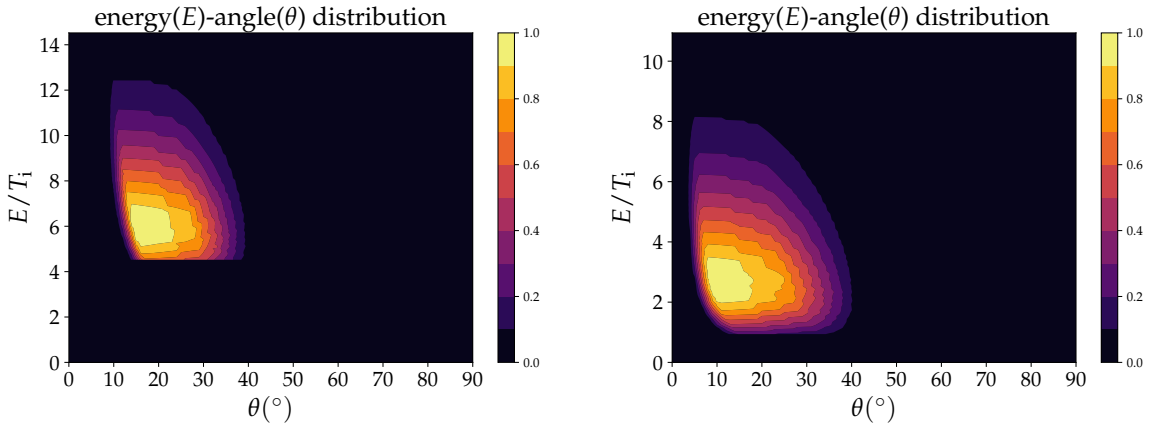

Figure 5.6: The ion distribution function at the wall as a function of kinetic energy E and the angle θ between the ion velocity and the wall for $\alpha = 3°$, $\Delta_s = 0.01$ and $T_e/T_\infty = 2$ on the left, $T_e/T_\infty = 0.5$ on the right. Figure provided courtesy of the author of the code [1].

of incidence. Example plots are given in Figure 5.6. However, the magnetic presheath code does not converge if the kinetic Chodura condition is not satisfied to appropriate accuracy. For this solver the condition needs to be satisfied to within $\approx 10\%$. In the next section we discuss the difficulties with satisfying the kinetic Chodura condition in our simulations.

5.4 Numerical Chodura condition

As argued in Section 3.2.3, we expect the distribution function at $x = 0$ to satisfy the kinetic Chodura condition, equation (3.5). The accuracy to which this condition will be satisfied numerically will depend on the resolution in velocity space, on how well the diverging electric field is captured near the MPE (which depends on the resolution in x space), on how well the exponentially small distribution function at small $v_\parallel$ is approximated by our discretisation, and on the size of our Newton's method error.

We use the code described in Chapter 4 to compute the following results. Firstly, we find how well the kinetic Chodura condition is satisfied for $\Delta_s = 0, 0.01,\ 0.05,\ 0.1,\ 0.5,\ 0.7,\ 1.0$ and $T_e = 0, 0.05, 0.25, 0.5, 1.0, 1.5$. This is shown in Figure 5.7. The condition is not satisfied well for flows with large Δ_s and small T_e, when the potential drop across the layer is small. This, we argue shortly, is a numerical issue, which comes from the resolution in x not being large enough to capture large electric fields near $x = 0$.

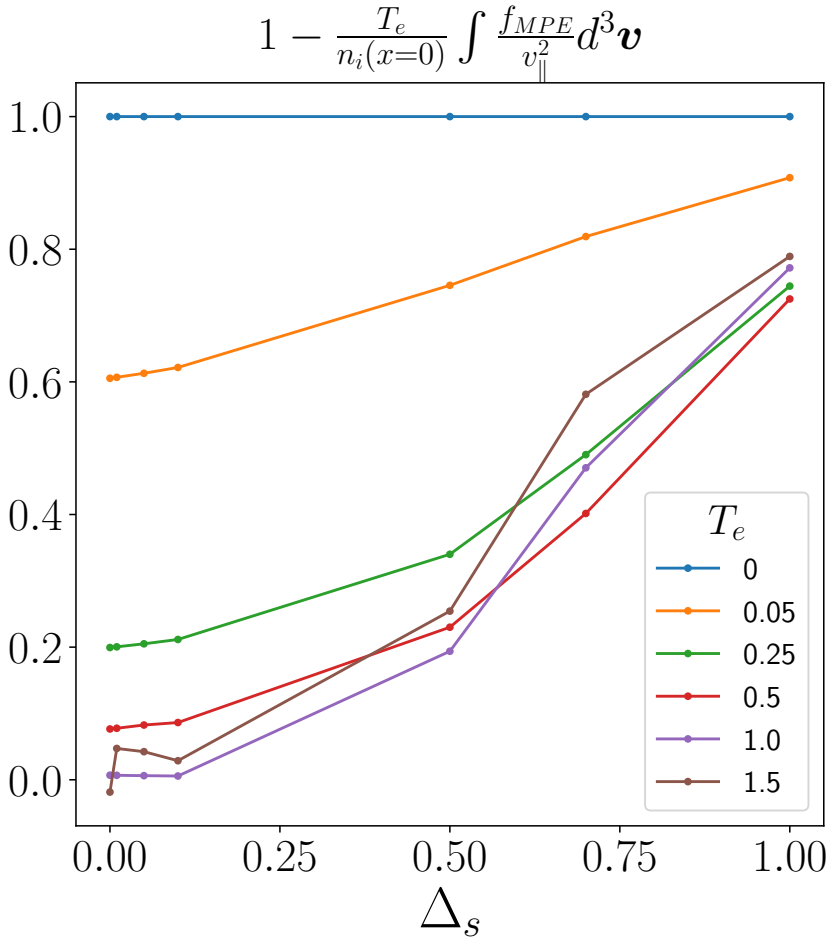

Figure 5.7: The value of $1-(T_e/n(x=0))\big(\int d^3\boldsymbol{v} f_{MPE}/v_\parallel^2\big)$ as a function of Δ_s for a range of T_e. The temperature ratio $T_e = 0$ corresponds to there being no field in the system in which case we cannot expect the kinetic Chodura condition to be satisfied. It, however, shows that capturing the diverging fields at low T_e can be difficult.

We can show why the kinetic Chodura condition is difficult to satisfy by assuming that the resolution in velocity space is very high, especially at low velocities, where the integrand in the kinetic Chodura integral is the largest. Then equation (4.20) is approximately

$$\frac{f(x_p, v_{\perp k}, v_{\parallel l}) - f(\xi, \zeta)}{\Delta t(x_p, v_{\parallel l})} - C[f(x_p)](v_{\perp k}, v_{\parallel l}) = \delta_N f_0 + \mathcal{E}_v, \tag{5.8}$$

where we remind the reader of the fact that δ_N is the error allowed by our Newton's method iteration and f_0 is the distribution function far away from the wall at $v_\parallel = v_\perp = 0$. The correction associated with the discretisation of velocity space, $\mathcal{E}_v$, becomes negligible for small $\Delta v_\perp$ and $\Delta v_\parallel$.

The derivation of the numerical Chodura condition starts with evaluating the quasineutrality numerically

$$n(x = x_1) - n(x = 0) = n(0)(\exp(\Delta\phi_0/T_e) - 1), \tag{5.9}$$

where $\Delta\phi_0 = \phi(x_1) - \phi(0) > 0$. To express the densities in terms of the distribution functions, we use (5.8) and extract terms that appear in the analytic kinetic Chodura condition. In Appendix G we show that (5.9) can be expressed as

$$\begin{aligned}\frac{\Delta\phi_0}{x_1}\left[1 - \frac{T_e}{n(0)}\int_{0\le v_\parallel\le V_{max}} d^3\boldsymbol{v}\frac{f_{MPE}}{v_\parallel^2}\right] \simeq & -\frac{T_e}{n(0)}\frac{\Delta\phi_0}{x_1}\int_{0\le v_\parallel\le v_c} d^3\boldsymbol{v}\frac{f_{MPE}}{v_\parallel^2} \\ & - \frac{T_e}{n(0)}\int_{v_c\le v_\parallel\le V_{max}} d^3\boldsymbol{v} C[f_{MPE}(v_\parallel)]\frac{\Delta t(0, v_\parallel > v_c)}{x_1}\left(1 - \frac{v_c^2}{v_\parallel^2}\right)^{-1/2} \\ & - \frac{T_e}{n(0)}\frac{1}{x_1}\int_{0\le v_\parallel\le v_c} d^3\boldsymbol{v} f_{MPE} + \frac{T_e}{n(0)}\frac{1}{x_1}\int_{v_\parallel<0} d^3\boldsymbol{v} f(x_1, v_\parallel) + \frac{T_e}{n(0)}\frac{\mathcal{E}_A}{x_1} + \frac{T_e}{n(0)}\frac{\mathcal{E}_B}{x_1},\end{aligned} \tag{5.10}$$

where f_{MPE} is the distribution function at $x = 0$, $v_c \equiv \sqrt{2\Delta\phi_0}$ and V_{max} is the largest value of $v_\parallel$ in the grid. The error $\mathcal{E}_A$ includes $\mathcal{E}_v$ and any numerical error in the evaluation of the integrals. The error $\mathcal{E}_B$ is defined as

$$\begin{aligned}\mathcal{E}_B \equiv & \int_{v_c\le v_\parallel\le V_{max}} d^3\boldsymbol{v} f_{MPE}(v_\parallel)\left(1 - \frac{v_c^2}{v_\parallel^2}\right)^{-1/2} - \int_{v_c\le v_\parallel\le V_{max}} d^3\boldsymbol{v} f_{MPE}(v_\parallel) \\ & - \int_{v_c\le v_\parallel\le V_{max}} d^3\boldsymbol{v} f_{MPE}(v_\parallel)\frac{v_c^2}{2v_\parallel^2}.\end{aligned} \tag{5.11}$$

This error is sue to the Taylor expansion of $(1 - v_c/v_\parallel)^{-1/2}$ for small $v_c/v_\parallel$ and is needed to recover the terms that appear in the analytic form of the kinetic Chodura condition (specifically the integral on the left hand side of (5.10)).

In (5.10) we have dropped some small terms (such as second order correction to quasineutrality and the error associated with Newton's method). This equation is still satisfied in our simulations to within 2% for most of the resolutions.

The kinetic Chodura condition (3.5) can be satisfied if $\Delta\phi_0/x_1$ is much larger than the terms on the right hand side, this way forcing the terms in the brackets on the left side to cancel. This relies on the terms on the right hand side of equation (5.10) not increasing faster than $\Delta\phi_0/x_1$ as $x_1 \to 0$. This trend is observed in most of the simulations. In theory, $\Delta\phi_0 \sim \sqrt{x_1}$, thus giving a large electric field as x_1 is decreased. Even so, in most of the simulations we have run, the resultant electric field is not large enough to make the right side terms completely negligible. Also note that some of the error terms have a $1/x_1$ scaling and thus can only be small relative to the electric field if the integrals multiplying them go to zero faster than $\Delta\phi_0$.

The errors on the right hand side of equation (5.10) divided by $\Delta\phi_0/x_1$, for a simulation with $\Delta_s = 0.1$ and $T_e = 0.5$, are shown in the top left of Figure 5.8. The definitions of the errors are

$$\text{Error 1} \equiv -\frac{T_e}{n(0)} \int_{0\le v_\parallel \le v_c} d^3\boldsymbol{v} \frac{f_{MPE}}{v_\parallel^2}, \tag{5.12}$$

$$\text{Error 2} \equiv -\frac{T_e}{\Delta\phi_0 n(0)} \int_{v_c\le v_\parallel \le V_{max}} d^3\boldsymbol{v} C[f_{MPE}(v_\parallel)]\Delta t(0, v_\parallel > v_c)\left(1 - \frac{v_c^2}{v_\parallel^2}\right)^{-1/2}, \tag{5.13}$$

$$\text{Error 3} \equiv -\frac{T_e}{n(0)}\frac{1}{\Delta\phi_0} \int_{0\le v_\parallel \le v_c} d^3\boldsymbol{v} f_{MPE}, \tag{5.14}$$

$$\text{Error 4} \equiv \frac{T_e}{n(0)}\frac{1}{\Delta\phi_0} \int_{v_\parallel<0} d^3\boldsymbol{v} f(x_1, v_\parallel), \tag{5.15}$$

$$\text{Error 5} \equiv \frac{T_e}{n(0)}\frac{\mathcal{E}_A}{\Delta\phi_0}, \tag{5.16}$$

$$\text{Error 6} \equiv \frac{T_e}{n(0)}\frac{\mathcal{E}_B}{\Delta\phi_0}. \tag{5.17}$$

Most of them are either small or decrease as resolution is improved, although the decrease is slow. The bottom left plot shows $\Delta\phi_0/x_1$ and the kinetic Chodura condition (term in the brackets on the left hand side of equation (5.10)) for the $\Delta_s = 0.1$ and $T_e = 0.5$ simulation. The electric field becomes large as resolution is increased and the kinetic Chodura condition is satisfied to a high accuracy. We see that, as we increase resolution, the accuracy increases up until $\Delta x_0 \approx 10^{-6}$. At an even higher resolution the error increases again. However, here we are approaching the limits of the code capabilities and

it is unclear if the numerical error is becoming larger here or if we have converged and are oscillating around a converged value. The kinetic Chodura condition in these simulations is satisfied sufficiently well to allow us to couple the code to a magnetic presheath solver `GYRAZE` [48], which requires the input distribution function to satisfy the condition. The left plot in Figure 5.9 shows $f_{MPE}/v_\parallel^2$ for the $\Delta_s = 0.1$ and $T_e = 0.5$ simulation, we see that the peak is well resolved and is converging.

The right plots in Figure 5.8 show the errors (5.12)–(5.17), $\Delta\phi_0/x_1$ and how well the kinetic Chodura condition is satisfied for a simulation with parameters $\Delta_s = 1.0$ and $T_e = 0.5$, where the kinetic Chodura condition is far from being satisfied. The errors are slightly increasing with higher resolution. This is due to the fact that the electric field near the MPE is small even at the highest resolutions (see the bottom right plot in Figure 5.8) – the divergence in electric field is not well captured. This is because at large Δ_s the total potential drop in the layer is small (see Figure 5.3), necessitating a very small x_1 to give a large $\Delta\phi_0/x_1$.

The dominant error is error 4. It is proportional to an integral over $v_\parallel < 0$ of $f(x_1)$, the distribution function one grid point away from $x = 0$. We expect this to be exponentially small as it is very close to the $f(x = 0, v_\parallel < 0) = 0$ region. The exponentially small behaviour is difficult to capture numerically. It is unclear, whether improving the resolution in x would result in the error eventually decreasing because the numerical errors in the code make the convergence of results at very high resolutions difficult.

From the right plot of Figure 5.9, we can see that the distribution function for $\Delta_s = 1.0$ and $T_e = 0.5$ at small velocities is not well resolved. The height of the peaks varies by a factor of 10^3 and it does not seem to be converging, so higher resolution is needed to capture the true size of the peak. The kinetic Chodura condition is far from being satisfied since the integral of the numerically found $f_{MPE}/v_\parallel^2$ is too small, indicating that the real peak occurs at even higher values. Also note that, compared to the left side plot of Figure 5.9 ($\Delta_s = 0.1$ simulation), the peak for the $\Delta_s = 1.0$ simulation occurs at much smaller $v_\parallel$, which means that a much higher resolution in velocity space is required, adding to the computational cost.

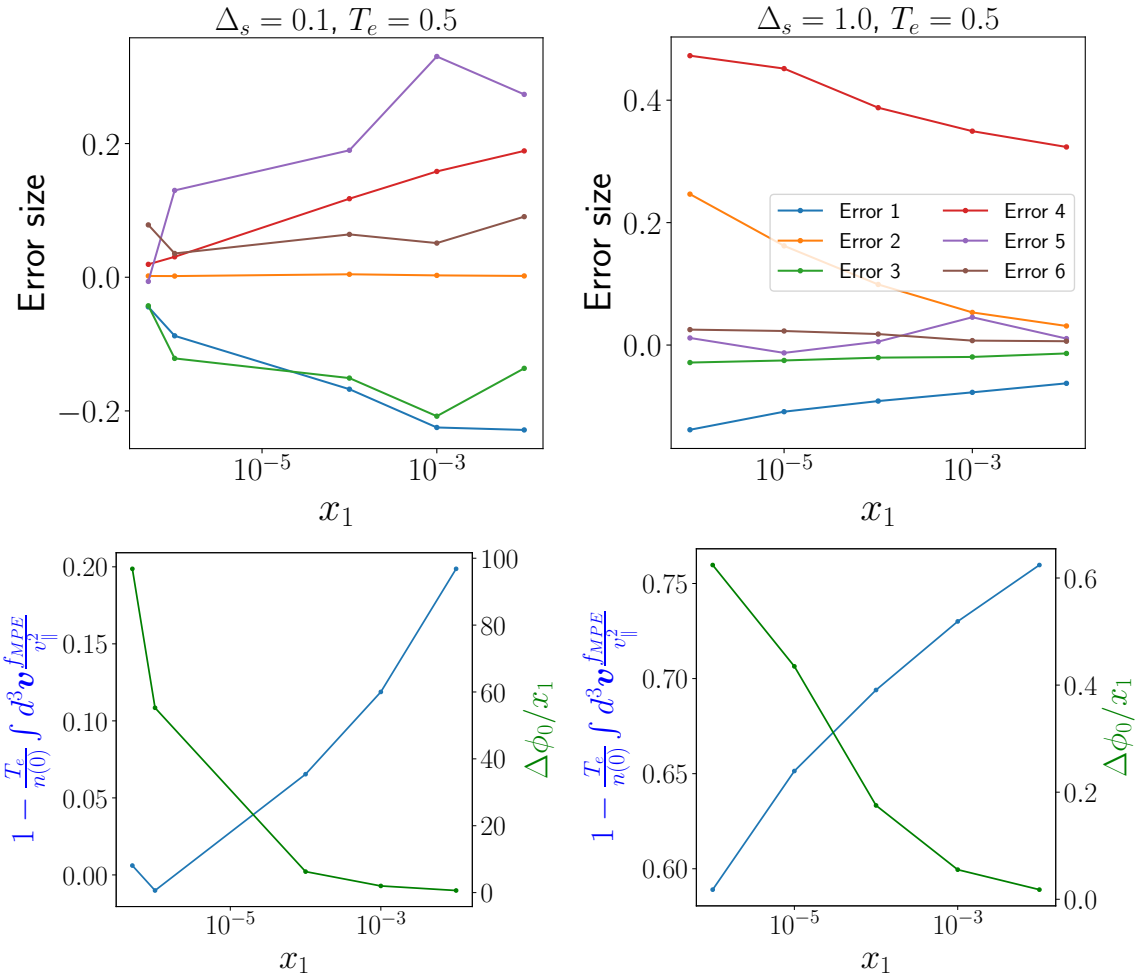

Figure 5.8: Plots for simulations with $T_e = 0.5$. **Left:** $\Delta_s = 0.1$ and **right:** $\Delta_s = 1.0$. The quantity x_1 is the distance between the $x = 0$ (the MPE) and the first grid point in position space. **Top row:** the errors defined in (5.12)–(5.17). The legend for both plots is shown in the top-right plot. For the left plot total error decreases with increasing resolution. The reduction of errors with decreasing x_1 is not observed in the plots on the right. **Bottom row:** the kinetic Chodura condition (the term in the brackets on the left hand side of equation (5.10), which is also approximately equal to the sum of all the errors) and $\Delta\phi_0/x_1$. The kinetic Chodura condition is closer to being satisfied at higher resolutions. This is explained by an increasing electric field reducing the errors. The electric field $\Delta\phi_0/x_1$ is small for the right plots even at highest resolutions, and the kinetic Chodura condition is far from being satisfied in this case.

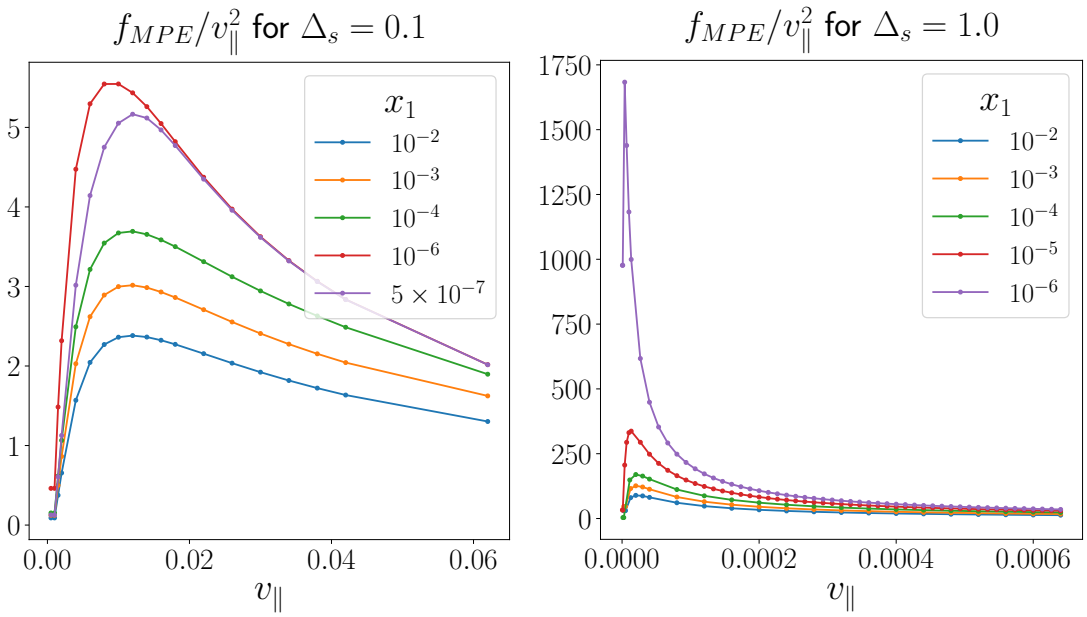

Figure 5.9: Plots of $f_{MPE}/v_\parallel^2$ at $v_\perp = 0$ for simulations with $T_e = 0.5$. **Left:** $\Delta_s = 0.1$ and **right:** $\Delta_s = 1.0$. Different curves have different x_1, which is the distance between $x = 0$ (the MPE) and the first grid point in position space. For the left plot, the peaks are not far from each other in absolute terms, with the function converging at a peak of ~ 5. All the peaks are resolved and the value of $f_{MPE}/v_\parallel^2$ at the first non-zero $v_\parallel$ point is small (as expected from the discussion in Section 4.4.1). For the right plot, the peaks are far from converged, with differences of $\sim 10^3$ as the resolution is changed. For the highest resolution simulation with $x_1 = 10^{-6}$ in the right plot, the velocity resolution near $v_\parallel = 0$ is $\sim 10^{-6}$.

Chapter 6

Discussion

In Section 6.1 we summarise the key results of the thesis and their significance. In Section 6.2 we discuss an extension of our model to include ion-neutral interactions. In Section 6.3 we describe future steps that should be taken to fully solve the collisional layer problem and how it could then be used to provide boundary conditions for fluid codes, which we also discussed in the introduction. We use dimensional variables in this chapter and reintroduce a subscript i for ion quantities.

6.1 Summary

The main result of this thesis is the ion distribution function and potential in the collisional layer given an incoming ion Maxwellian. Crucially, we found that at the MPE the ion distribution function satisfies the kinetic Chodura condition, as long as the simulation is well resolved. We know that this condition is satisfied by the exact solution from the theoretical analysis done in Chapter 3. This allows us to couple the magnetic presheath and Debye sheath solver `GYRAZE` [1] to a fluid simulation, which provides an incoming Maxwellian as a boundary condition for the collisional layer. Thus we can find the exact ion distribution function at the wall, which can be used to calculate sputtering, without having to solve a fully kinetic model in the wall region. In addition, the work has showed that satisfying the kinetic Chodura condition exactly is very difficult as one needs to capture the effect of a diverging electric field and resolve the ion distribution function at very small velocities. We showed in Section 3.2.1 that the distribution function is exponentially small at small velocities. This result was recovered in some simulations as the values of $f_{MPE}/v_{\parallel}^2$ were indeed small at the smallest $v_{\parallel}$, but for cases with less resolution it was not

possible to resolve the region of velocity space where f_i is exponentially small, and the kinetic Chodura condition was not satisfied (see Section 5.4). In addition, we showed that enforcing the potential between the MPE at $x = 0$ and the next position grid point x_1 to be $\sqrt{x}$ was essential in capturing the kinetic Chodura condition numerically (Section 4.4.1). However, the electric potential values in the rest of the collisional layer were not affected much by this choice of the potential next to $x = 0$ (Section 5.1).

Another takeaway from this work is that the collisional layer does not have a major effect on the distribution function overall. It does have a large effect on the ion distribution function at small $v_\parallel$, as it ensures that the kinetic Chodura condition is satisfied, but the function changes little from the incoming Maxwellian at $v_\parallel \sim v_{ti\infty}$. This suggests that it might be more efficient to numerically solve the collisional layer by expanding $f_i - f_{i\infty}$ in terms of the finite element basis functions. We attempted this, but we could not finish the implementation due to various numerical difficulties. However, the code has evolved since then and trying this approach again could be useful in speeding up the simulations.

Any drift kinetic code simulating the SOL up to the magnetic presheath should check how well the ion distribution function at the MPE satisfies the kinetic Chodura condition. In addition, it should be checked that a diverging electric field is recovered. The scaling of the potential could also be a valid bench mark. In our model the field scaled as $\phi \sim \sqrt{x}$ since we had ion-ion collisions only (the result also holds if the full Fokker-Planck collision operator is replaced by a diffusive model operator). As discussed below, even with neutrals, we expect diverging electric fields to be produced at the MPE and thus the ion distribution to satisfy kinetic Chodura condition.

6.2 Effect of neutrals

Adding neutrals would be a natural extension to our numerical and analytical model. We would solve it together with the kinetic equation for neutrals, where appropriate boundary conditions would have to be imposed for the neutral distribution function. The charge exchange collision operator for the ion (f_i) and neutral (f_n) distribution functions would need to be added to the right hand side of the ion drift kinetic equation (1.19). It is given

by

$$C_{cx}[f_i, f_n] = -\int d^3\boldsymbol{v}'\sigma_{cx}|\boldsymbol{v}-\boldsymbol{v}'|(f_i(\boldsymbol{v})f_n(\boldsymbol{v}')-f_i(\boldsymbol{v}')f_n(\boldsymbol{v})), \tag{6.1}$$

where σ_x is the charge exchange cross section. A good approximation is to assume $\sigma_x|\mathbf{v}-\mathbf{v}'| = K_x$, where K_x is a constant [28, 49]. Thus the operator simplifies to $-K_x(n_n f_i - n_i f_n)$, where n_i is the ion density and n_n is the neutral density. This would give us a system of equations that could be solved by our code, given appropriate boundary conditions for neutrals. As we see, both of the terms in $C_{cx}[f_i, f_n]$ are finite at $v_\parallel \ll v_{ti\infty}$. Therefore, our analysis from Section 3.1 would not change as the ion-ion operator, which is of the form $\sim \partial^2 f_i/\partial v_\parallel^2$, would dominate to lowest order for small $v_\parallel$ and thus the electric field at the wall would still diverge. The diverging electric field then implies that the Chodura condition is satisfied as long as integrals in (3.52) are well defined. However, proving this is not obvious. Our proof of an exponentially small distribution function in Section 3.2.1 would not be applicable. This is because $K_x n_i f_n$ would appear on the right side of equation (3.49), even if f_i was zero to lowest order, giving a non-zero f_1.

Ion interactions with neutrals are very likely to affect the ion distribution function at the MPE and thus the ion distribution function at the wall. With regards to boundary conditions for fluid codes, adding neutrals to our model would only be useful if it could then be coupled to a fluid model that takes the effect of neutrals on ion transport coefficients into account [28, 50].

6.3 Importance of kinetic electrons

The numerical code developed in this thesis allows us to find the potential drop in the collisional layer for a given ion mean flow Δ_s and electron ion temperature ratio $ZT_e/2T_{i\infty}$ at the boundary at $x \to \infty$ (CLE). We mentioned in the introduction that at this stage this code cannot be used to obtain boundary conditions for fluid codes because it does not take kinetic electron effects into account. To make the code useful for fluid models, it must provide the electron mean flow at infinity $u_{e\parallel\infty}$ given the incoming ion and electron temperatures ($T_{i\infty}$ and $T_{e\infty}$, respectively), ion mean flow $u_{i\parallel\infty}$, and the potential drop $\Delta\phi_{Tot}$ across the collisional layer, the magnetic presheath and Debye sheath; that is, we

need to calculate a function F that gives

$$u_{e\parallel\infty}/c_s = F(e\Delta\phi_{Tot}/T_{e\infty}, u_{i\parallel\infty}/c_s, T_{e\infty}/T_{i\infty}). \tag{6.2}$$

For this we need to add the steady state drift kinetic equation for the electron distribution function f_e to the model, instead of assuming an adiabatic electron response. The drift kinetic electron equation would have both electron self-collisions ($C_{ee}[f_e, f_e]$) and electron-ion collisions ($C_{ei}[f_e, f_i]$) and explicitly be given by

$$-v_\parallel \sin\alpha \frac{\partial f_e}{\partial x} - \frac{e}{m_e}\sin\alpha \frac{\partial \phi}{\partial x}\frac{\partial f_e}{\partial v_\parallel} = C_{ei}[f_e, f_i] + C_{ee}[f_e, f_e]. \tag{6.3}$$

This addition of electrons is not a trivial step. The adiabatic electron response allowed us to relate the ion distribution function to the potential directly. Without it the ion and electron equations would have to be solved together with quasineutrality until appropriate values of the potential $\phi(x_j)$ were determined. This, together with the additional electron distribution function and another collision operator for electron-ion collisions would make it a computationally more expensive task. However, in principle, it could be done.

We would need boundary conditions for the electron distribution function $f_e(x, v_\perp, v_\parallel)$ at CLE, just like we did for the ions. The condition $f_e(x = x_{N_x-1}, v_\perp, v_\parallel > 0)$ would be a Maxwellian with the electron temperature $T_{e\infty}$ and the mean flow $u_{e\parallel\infty}$. However, unlike for the ions, the electron mean flow is an output of the model (see equation (6.3)). Adding the electrons to our model requires solving the magnetic presheath and Debye sheaths simultaneously with the collisional layer. We could do this as follows.

We would guess how much of the total potential drop ($\Delta\phi_{Tot}$ is given) occurs in the collisional layer $\Delta\phi_{CL}^{(0)}$ and set the potential drop in the magnetic presheath and Debye sheath to be $\Delta\phi_{Tot} - \Delta\phi_{CL}^{(0)}$, where the superscript (0) indicates that this is our initial step. This drop, together with an initial guess of the ion and electron distribution functions at the MPE (denoted by $x = 0$ in this thesis) could be given to the magnetic presheath and Debye sheath solver `GYRAZE` [1] and would provide the reflected electron distribution function $f_e(x = 0, v_\perp, v_\parallel < 0)$. This is a boundary condition for the electron distribution function in our collisional layer solver. From the electron distribution function $f_e(x = 0, v_\perp, v_\parallel)$, we would also have the first guess of the electron particle flux $n_e^{(0)}(x = 0)u_{e\parallel}^{(0)}(x = 0)$. Since electron particle flux is constant in the collisional layer, this allows us to determine the new mean flow at infinity $u_{e\parallel\infty}^{(0)}$. Then, the electron boundary condition

at infinity is a Maxwellian with this new mean flow. Now we can solve our collisional layer model to obtain a new $f_e^{(1)}(x=0, v_\perp, v_\parallel > 0)$ and $\Delta\phi_{CL}^{(1)}$. Since $\Delta\phi_{Tot}$ is unchanged, the drop across the magnetic presheath also has to be changed to $\Delta\phi_{Tot} - \Delta\phi_{CL}^{(1)}$. We can solve the magnetic presheath and repeat to obtain $f_e^{(2)}(x=0, v_\perp, v_\parallel < 0)$. We would continue the iteration until the potential drops across each layer stop changing. This procedure gives $u_{e\parallel\infty}$ as well as $f_{e,CLE}$, the electron distribution function at CLE. To find the electron heat flux $q_{e\parallel\infty}$ we need to add the corrections to the Maxwellian that give $q_{e\parallel\infty}$ in Braginskii's model to the incoming distribution function $f_{e,CLE}(v_\parallel > 0)$. From our collisional layer solution we would obtain the outgoing part $f_{e,CLE}(v_\parallel < 0)$ and hence $q_{e\parallel\infty}$. In addition, this method would provide us with the split of $\Delta\phi_{Tot}$ among the collisional layer, the magnetic presheath and Debye sheath.

Theoretical analysis of the kinetic electron effects could be looked at in future work. Specifically, predicting the constraints and properties of the electron distribution function at the CLE or MPE for given boundary conditions (similar to what we did for ions in chapters 2 and 3), would be useful. It could be used for checking the results of the code, or making the numerical calculations more efficient by providing them the analytical constraints.

Appendix A

Fluid equations used in edge modelling

We give an example of electrostatic drift-reduced Braginskii equations, which are often used in the edge modelling. Here we show the equations used in GBS [30]. These are, in the order listed, the continuity equation, vorticity equation (current conservation), electron and ion parallel momentum equations, electron and ion energy equations, and the Poisson equation:

$$\frac{\partial n}{\partial t} = -\frac{1}{B}[\phi, n] + \frac{2}{eB}\left[C(p_e) - enC(\phi)\right] - \nabla_\parallel(nu_{e\parallel}) + D_n\nabla_\perp^2 n + s_n, \tag{A.1}$$

$$\frac{\partial \Omega}{\partial t} = -\frac{1}{B}\nabla\cdot[\phi, \boldsymbol{\omega}] - \nabla\cdot(u_{i\parallel}\nabla_\parallel\boldsymbol{\omega}) + \frac{B\Omega_i}{e}\nabla_\parallel j_\parallel + \frac{2\Omega_i}{e}C(p_e + p_i) + \frac{\Omega_i}{3e}C(G_i) + D_\Omega\nabla_\perp^2\Omega, \tag{A.2}$$

$$\frac{\partial u_{e\parallel}}{\partial t} = -\frac{1}{B}[\phi, u_{e\parallel}] - u_{e\parallel}\nabla_\parallel u_{e\parallel} + \frac{e}{m_e}\left(\frac{j_\parallel}{\sigma_\parallel} + \nabla_\parallel\phi - \frac{1}{en}\nabla_\parallel p_e - 0.71e\nabla_\parallel T_e - \frac{2}{3en}\nabla_\parallel G_e\right) + D_{u_{e\parallel}}\nabla_\perp^2 u_{e\parallel}, \tag{A.3}$$

$$\frac{\partial u_{i\parallel}}{\partial t} = -\frac{1}{B}[\phi, u_{i\parallel}] - u_{i\parallel}\nabla_\parallel u_{i\parallel} - \frac{1}{m_i n}\nabla_\parallel(p_e + p_i) - \frac{2}{3m_i n}\nabla_\parallel G_i + D_{u_{i\parallel}}\nabla_\perp^2 u_{i\parallel}, \tag{A.4}$$

$$\frac{\partial T_e}{\partial t} = -\frac{1}{B}[\phi, T_e] - u_{e\parallel}\nabla_\parallel T_e + \frac{2}{3}T_e\left[\frac{0.71\nabla_\parallel j_\parallel}{en} - \nabla_\parallel u_{e\parallel}\right] + \frac{4}{3}\frac{T_e}{eB}\left[\frac{7}{2}C(T_e) + \frac{T_e}{n}C(n) - eC(\phi)\right] + \nabla_\parallel(\chi_{\parallel e}\nabla_\parallel T_e) + D_{T_e}\nabla_\perp^2 T_e + s_{T_e} - \frac{4}{3}\frac{m_e}{m_i}\frac{1}{\tau_e}(T_e - T_i), \tag{A.5}$$

$$\frac{\partial T_i}{\partial t} = -\frac{1}{B}[\phi, T_i] - u_{i\parallel}\nabla_\parallel T_i + \frac{4}{3}\frac{T_i}{eB}\left[C(T_e) + \frac{T_e}{n}C(n) - eC(\phi)\right] - \frac{10}{3}\frac{T_i}{eB}C(T_i) + \frac{2}{3}T_i\left[(u_{i\parallel} - u_{e\parallel})\frac{\nabla_\parallel n}{n} - \nabla_\parallel u_{e\parallel}\right] + \nabla_\parallel(\chi_{\parallel i}\nabla_\parallel T_i) + D_{T_i}\nabla_\perp^2 T_i + s_{T_i} + \frac{4}{3}\frac{m_e}{m_i}\frac{1}{\tau_e}(T_e - T_i), \tag{A.6}$$

$$\nabla\cdot(n\nabla_\perp\phi) = \Omega - \frac{\nabla_\perp^2 p_i}{e}, \tag{A.7}$$

where $\Omega = \nabla\cdot\boldsymbol{\omega} = \nabla\cdot(n\nabla_\perp\phi + \nabla_\perp p_i/e)$ is the scalar vorticity, n is the density of ions (equal to density of electrons due to quasineutrality), $m_r, u_{\parallel r}, T_r$ and $p_r = n_r T_r$ are the mass, mean flow parallel to the field, temperature and pressure of species r, and $r = i, e$ stands for ions and electrons, $\Omega_i = eB/m_i$ and $\Omega_e = eB/m_e$ are the gyrofrequencies of ions and electrons, respectively, B is the magnetic field strength, ϕ is the electric potential, $j_\parallel = en(u_{i\parallel} - u_{e\parallel})$ is the parallel current, $D_\Omega, D_{u_{e\parallel}}, D_{u_{i\parallel}}, D_{T_e}$ and D_{T_i} are numerical diffusion terms, s_n and s_T are source terms, G_i and G_e are the ion and electron gyroviscous terms given by

$$G_r = -\eta_{0r}\left[2\nabla_\parallel v_{\parallel i} + \frac{C(\phi)}{B}\frac{C(p_r)}{Z_r nB}\right], \tag{A.8}$$

where $Z_i = 1$, $Z_e = -1$, $\eta_{0i} = 0.96nT_i\tau_i$ and $\eta_{0e} = 0.73nT_e\tau_e$. The collisional times τ_r are the inverse of collisional frequencies ν_r and are given by

$$\frac{1}{\tau_e} = \nu_e = \frac{4\sqrt{2\pi}}{3}\frac{e^4 n\ln\Lambda_{ee}}{(4\pi\epsilon_0)^2 m_e^{1/2}T_e^{3/2}}, \tag{A.9}$$

$$\frac{1}{\tau_i} = \nu_i = \frac{2\sqrt{2\pi}}{3}\frac{e^4 n\ln\Lambda_{ii}}{(4\pi\epsilon_0)^2 m_i^{1/2}T_i^{3/2}}, \tag{A.10}$$

where $\ln\Lambda_{rr}$ is the Coulomb logarithm for species r. The coefficients $\chi_{\parallel i}$ and $\chi_{\parallel e}$ are the ion and electron thermal conductivities, and $\sigma_\parallel$ is the Spitzer conductivity. For the definitions of the latter terms as well as the normalisations used, see [30]. The Poisson bracket and the curvature operators are defined in equations (1.42) and (1.43), respectively.

Appendix B

Derivation of the kinetic Bohm condition

In the Debye sheath the plasma can be described by the steady state collisionless kinetic equation. For a species r, with a distribution function f_r, it is given by

$$\mathbf{v} \cdot \nabla f_r + \frac{Z_r e}{m_r}(\mathbf{E} + \mathbf{v} \times B) \cdot \frac{\partial f}{\partial \mathbf{v}} = 0. \tag{B.1}$$

Taking the first moment of this equation we get the momentum equation

$$\nabla \cdot \int d^3\mathbf{v}\, f_r(x, \mathbf{v}) m_r \mathbf{v}\mathbf{v} = Z_r e n_r (\mathbf{E} + \mathbf{u}_r \times \mathbf{B}), \tag{B.2}$$

where

$$n_r = \int d^3\mathbf{v}\, f_r, \qquad \mathbf{u}_r = \frac{1}{n_r} \int d^3\mathbf{v}\, f_r \mathbf{v} \tag{B.3}$$

are the density and average velocity.

The gradients in the x direction (perpendicular to the wall) dominate in this region as $L_x \sim \lambda_D \ll \lambda_{SOL} \sim L_y \lesssim L_z$, where $\lambda_{SOL} \sim 1$cm is the width of the SOL. In the Debye sheath the electric field is ordered as $E_x = -\partial\phi/\partial x \sim T_e/e\lambda_D$, and the mean flow of ions and electrons is $u_{i,x} \sim u_{e,x} \sim v_{ti} \ll v_{te}$. Therefore, $u_{s,x}B/E_x \sim \lambda_D/\rho_i \ll 1$ and the magnetic field can be neglected to lowest order in λ_D/ρ_i. This gives lowest order momentum equation

$$\frac{\partial}{\partial x} \int d^3\mathbf{v}\, f_r m_r v_x^2 = Z_r e n_r E_x, \tag{B.4}$$

where the integral on the left hand side is the momentum flux in the x direction of species r. Adding the ion and electron momentum equations, using Gauss's law

$$-\epsilon_0 \frac{\partial^2 \phi}{\partial x^2} = e(Z n_i - n_e), \tag{B.5}$$

and integrating in x gives

$$\epsilon_0\left(\frac{\partial\phi}{\partial x}\right)^2 = \int d^3\mathbf{v}\, f_i(x,\mathbf{v})m_i v_x^2 - \int d^3\mathbf{v}\, f_i(x_{DSE},\mathbf{v})m_i v_x^2 + \int d^3\mathbf{v}\, f_e(x,\mathbf{v})m_e v_x^2 - \int d^3\mathbf{v}\, f_e(x_{DSE},\mathbf{v})m_e v_x^2, \tag{B.6}$$

where we have set $\partial\phi/\partial x = 0$ at the DSE to lowest order in λ_D/ρ_i.

The electrons are assumed to be adiabatic and thus

$$\int d^3\mathbf{v}\, f_e(x,\mathbf{v})m_e v_x^2 = n_e T_e = n_{e,DSE} T_e \exp(e\phi/T_e), \tag{B.7}$$

where we have set $\phi_{DSE} = 0$. The potential decreases as we approach the negatively charged wall and thus the electron pressure defined above will decrease. The left hand side of (B.6) is always greater than or equal to zero. This means that as ions are accelerated towards the wall their momentum flux towards the wall has to increase faster than the electron energy is decreasing. This will lead to the Bohm condition, which says that there are few slow ions at the DSE, as slow ions at the DSE cannot increase the ion momentum flux fast enough.

To prove this, consider the region of space just inside the Debye sheath, where $e\phi/T_e \ll 1$. Then to second order in $e\phi/T_e \ll 1$ the electron pressure is

$$\int d^3\mathbf{v}\, f_e(x,\mathbf{v})m_e v_x^2 = n_{e,DSE} T_e\left(1 + \frac{e\phi}{T_e} + \frac{1}{2}\left(\frac{e\phi}{T_e}\right)^2 + O\left(\left(\frac{e\phi}{T_e}\right)^3\right)\right). \tag{B.8}$$

Since the electric field dominates over the magnetic field, the ion kinetic equation in the Debye sheath simplifies to

$$\frac{\partial f_i}{\partial x} - \frac{Ze}{m_i}\frac{\partial\phi}{\partial x}\frac{\partial f}{\partial v_x} = 0. \tag{B.9}$$

We see that the ion trajectories have a conserved quantity $\mathcal{E}_x = v_x^2/2 + Ze\phi/m_i$, which is the energy per unit mass. The solution to (B.9) is then $f(x,\mathcal{E}_x) = f(\mathcal{E}_x)$. In the region of interest, near the DSE, $e\phi/\mathcal{E}_x \ll 1$. Changing the integration variables from v_x to $\mathcal{E}_x$

(the Jacobian is $dv_x = d\mathcal{E}_x/|v_x|$) and expanding in $e\phi/\mathcal{E}_x \ll 1$ we get

$$\begin{aligned}\int d^3\mathbf{v}\, f_i(x,\mathbf{v}) m_e v_x^2 &= \int dv_y dv_z d\mathcal{E}_x\, f_i(\mathcal{E}_x, v_y, v_z) m_i \sqrt{2\Big(\mathcal{E}_x - Ze\phi/m_i\Big)} \\ &= \int dv_y dv_z d\mathcal{E}_x\, f_i(\mathcal{E}_x, v_y, v_z) m_i \sqrt{2\mathcal{E}_x} \\ &- Ze\phi \int dv_y dv_z \frac{d\mathcal{E}_x}{\sqrt{2\mathcal{E}_x}}\, f_i(\mathcal{E}_x, v_y, v_z) \\ &- \frac{(Ze\phi)^2}{2m} \int dv_y dv_z \frac{d\mathcal{E}_x}{\sqrt{2\mathcal{E}_x}} \frac{f_i(\mathcal{E}_x, v_y, v_z)}{2\mathcal{E}_x} + O\left(\left(\frac{e\phi}{\mathcal{E}_x}\right)^3\right). \end{aligned} \tag{B.10}$$

Since the distribution function written as a function of the $\mathcal{E}_x$ variable is independent of x, the expression simplifies to

$$\begin{aligned}\int d^3\mathbf{v}\, f_i(x,\mathbf{v}) m_i v_x^2 = p_{i,DSE} - Ze\phi n_{i,DSE} - \frac{(Ze\phi)^2}{2m} \int d^3\mathbf{v} \frac{f_i(x_{DSE},\mathbf{v})}{v_x^2} \\ + O\left(\left(\frac{e\phi}{\mathcal{E}_x}\right)^3\right), \end{aligned} \tag{B.11}$$

where we changed back to velocity variable v_x. Note that the distribution function is evaluated at the DSE.

Putting the expressions (B.8) and (B.11) into (B.6) and only keeping terms to second order in $e\phi/T_e$ gives

$$\epsilon_0 \left(\frac{\partial \phi}{\partial x}\right)^2 = \frac{(Ze\phi)^2}{2m} \left(- \int d^3\mathbf{v} \frac{f_i(x_{DSE},\mathbf{v})}{v_x^2} + \frac{m_i n_{e,DSE}}{Z^2 T_e} \right), \tag{B.12}$$

where we used quasineutrality at the DSE, $Z n_{i,DSE} = n_{e,DSE}$. Noting that the left hand side is always greater than or equal to zero gives the Bohm condition (1.1).

Appendix C

Collision operator for the gyroaveraged ion distribution function f

In this section we find the explicit form of $\mathbf{\Gamma}$, defined in equation (1.21), for the case of a gyrophase independent distribution function $f(v_\perp, v_\parallel)$. The fact that $f(v'_\perp, v'_\parallel)$ is independent of φ' allows us to find an analytic expression for the integral over the gyrophase. To simplify the notation we introduce $f' \equiv f(v'_\perp, v'_\parallel)$.

Firstly we write out the integrand explicitly in its components. We use the same cylindrical coordinate system for velocity space as in the rest of the thesis. Using equations (1.22) and (1.23) in equation (1.21) gives

$$\begin{aligned}\mathbf{\Gamma} = \int d^3\mathbf{v}' f f' \frac{1}{g^3}\Bigg\{ g^2 \Bigg[\left(\frac{\partial \ln f}{\partial v_\parallel} - \frac{\partial \ln f'}{\partial v'_\parallel} \right) \hat{\mathbf{b}} + \frac{\partial \ln f}{\partial v_\perp} \hat{\mathbf{v}}_\perp - \frac{\partial \ln f'}{\partial v'_\perp} \hat{\mathbf{v}'}_\perp \Bigg] \\ - \mathbf{g} \Bigg[(v_\parallel - v'_\parallel) \left(\frac{\partial \ln f}{\partial v_\parallel} - \frac{\partial \ln f'}{\partial v'_\parallel} \right) + \frac{\partial \ln f}{\partial v_\perp} v_\perp + \frac{\partial \ln f'}{\partial v'_\perp} v'_\perp \\ - \hat{\mathbf{v}}_\perp \cdot \hat{\mathbf{v}'}_\perp \left(\frac{\partial \ln f}{\partial v_\perp} v'_\perp + \frac{\partial \ln f'}{\partial v'_\perp} v_\perp \right) \Bigg] \Bigg\}. \end{aligned} \tag{C.1}$$

The dot product $\hat{\mathbf{v}}_\perp \cdot \hat{\mathbf{v}'}_\perp$ is $\hat{\mathbf{v}}_\perp \cdot \hat{\mathbf{v}'}_\perp = \cos(\varphi - \varphi')$.

To simplify the calculations, it is convenient to change the integration variable from φ' to γ, where $\gamma = \pi + \varphi - \varphi'$. Then $\hat{\mathbf{v}}_\perp \cdot \hat{\mathbf{v}'}_\perp = -\cos\gamma$ and $g^2 = (v_\parallel - v'_\parallel)^2 + v_\perp^2 + v_\perp'^2 + 2v_\perp v'_\perp \cos\gamma$. Writing out $\mathbf{g}$, g and $d^3\mathbf{v}'$ explicitly and using the change of variables

$\varphi' \to \gamma$, equation (C.1) becomes

$$\begin{aligned}
\mathbf{\Gamma} = \int dv'_\perp dv'_\parallel d\gamma\ v'_\perp f f' & \frac{1}{((v_\parallel - v'_\parallel)^2 + v_\perp^2 + v_\perp'^2)^{3/2}(1 + k\cos\gamma)^{3/2}} \\
\times \Bigg\{ \Bigg[& (v_\perp^2 + v_\perp'^2)\left(\frac{\partial \ln f}{\partial v_\parallel} - \frac{\partial \ln f'}{\partial v'_\parallel}\right) - (v_\parallel - v'_\parallel)\left(\frac{\partial \ln f}{\partial v_\perp} v_\perp + \frac{\partial \ln f'}{\partial v'_\perp} v'_\perp\right) \\
& + \cos\gamma\left(2 v_\perp v'_\perp \left(\frac{\partial \ln f}{\partial v_\parallel} - \frac{\partial \ln f'}{\partial v'_\parallel}\right) - (v_\parallel - v'_\parallel)\left(\frac{\partial \ln f}{\partial v_\perp} v'_\perp + \frac{\partial \ln f'}{\partial v'_\perp} v_\perp\right)\right)\Bigg] \hat{\mathbf{b}} \\
& + \Bigg[((v_\parallel - v'_\parallel)^2 + v_\perp^2 + v_\perp'^2)\frac{\partial \ln f}{\partial v_\perp} - v_\perp (v_\parallel - v'_\parallel)\left(\frac{\partial \ln f}{\partial v_\parallel} - \frac{\partial \ln f'}{\partial v'_\parallel}\right) \\
& - v_\perp \left(\frac{\partial \ln f}{\partial v_\perp} v_\perp + \frac{\partial \ln f'}{\partial v'_\perp} v'_\perp\right) + v_\perp \cos\gamma \left(\frac{\partial \ln f}{\partial v_\perp} v'_\perp - \frac{\partial \ln f'}{\partial v'_\perp} v_\perp\right)\Bigg] \hat{\mathbf{v}}_\perp \\
& - \Bigg[((v_\parallel - v'_\parallel)^2 + v_\perp^2 + v_\perp'^2)\frac{\partial \ln f'}{\partial v'_\perp} - v'_\perp (v_\parallel - v'_\parallel)\left(\frac{\partial \ln f}{\partial v_\parallel} - \frac{\partial \ln f'}{\partial v'_\parallel}\right) \\
& - v'_\perp \left(\frac{\partial \ln f}{\partial v_\perp} v_\perp + \frac{\partial \ln f'}{\partial v'_\perp} v'_\perp\right) - v'_\perp \cos\gamma \left(\frac{\partial \ln f}{\partial v_\perp} v'_\perp - \frac{\partial \ln f'}{\partial v'_\perp} v_\perp\right)\Bigg] \hat{\mathbf{v}}'_\perp \Bigg\},
\end{aligned} \tag{C.2}$$

where we have defined

$$k = \frac{2 v_\perp v'_\perp}{(v_\parallel - v'_\parallel)^2 + v_\perp^2 + v_\perp'^2}. \tag{C.3}$$

Using the elliptic integrals, defined in equation (1.26) and the trigonometric identity

$$1 + k\cos\gamma = (1+k)\left(1 - \frac{2k}{1+k}\sin^2\left(\frac{\gamma}{2}\right)\right), \tag{C.4}$$

we evaluate the following integrals

$$\int_0^{2\pi} d\gamma \frac{1}{(1+k\cos\gamma)^{3/2}} = \frac{4}{(1+k)^{1/2}(1-k)} E\left(\frac{2k}{1+k}\right), \tag{C.5}$$

$$\int_0^{2\pi} d\gamma \frac{\cos(\pi+\varphi-\gamma)}{(1+k\cos\gamma)^{3/2}} = \frac{4\cos\varphi}{k(1+k)^{1/2}} \left\{ \frac{1}{1-k} E\left(\frac{2k}{1+k}\right) - K\left(\frac{2k}{1+k}\right)\right\}, \tag{C.6}$$

$$\int_0^{2\pi} d\gamma \frac{\cos\gamma\cos(\pi+\varphi-\gamma)}{(1+k\cos\gamma)^{3/2}} = \frac{4\cos\varphi}{k^2(1+k)^{1/2}} \left\{ \frac{2-k^2}{1-k} E\left(\frac{2k}{1+k}\right) - 2K\left(\frac{2k}{1+k}\right)\right\}, \tag{C.7}$$

$$\int_0^{2\pi} d\gamma \frac{\sin(\pi+\varphi-\gamma)}{(1+k\cos\gamma)^{3/2}} = \frac{4\sin\varphi}{k(1+k)^{1/2}} \left\{ \frac{1}{1-k} E\left(\frac{2k}{1+k}\right) - K\left(\frac{2k}{1+k}\right)\right\}, \tag{C.8}$$

$$\int_0^{2\pi} d\gamma \frac{\cos\gamma\sin(\pi+\varphi-\gamma)}{(1+k\cos\gamma)^{3/2}} = \frac{4\sin\varphi}{k^2(1+k)^{1/2}} \left\{ \frac{2-k^2}{1-k} E\left(\frac{2k}{1+k}\right) - 2K\left(\frac{2k}{1+k}\right)\right\}. \tag{C.9}$$

From here on we will write K and E instead of $K(\frac{2k}{1+k})$ and $E(\frac{2k}{1+k})$ to make equations easier to read. Substituting the integral expressions (C.5)–(C.9) into equation (C.2) gives equation (1.24), where the coefficients $X_{\parallel\parallel}, X_{\parallel\perp}, X_{\parallel\perp'}, X_{\perp\parallel}, X_{\perp\perp}$ and $X_{\perp\perp'}$ are defined in equation (1.25).

Appendix D

Moments for H_{1A} and H_{1B}

Here we list useful integrals that we use to evaluate the moments of equation (2.49). The integrals of H_{1B} involve the following moments of f_{Ms}

$$\int d^3\mathbf{w} f_{Ms} = n_{i\infty}, \tag{D.1}$$

$$\int d^3\mathbf{w} w^2 f_{Ms} = \frac{3}{2} n_{i\infty} v_{t\infty}^2, \tag{D.2}$$

$$\int d^3\mathbf{w} w_\parallel^2 f_{Ms} = \frac{1}{2} n_{i\infty} v_{t\infty}^2, \tag{D.3}$$

$$\int d^3\mathbf{w} w_\parallel^2 w^2 f_{Ms} = \frac{5}{4} n_{i\infty} v_{t\infty}^4, \tag{D.4}$$

$$\int d^3\mathbf{w} w^4 f_{Ms} = \frac{15}{4} n_{i\infty} v_{t\infty}^4, \tag{D.5}$$

$$\int d^3\mathbf{w} w_\parallel^4 f_{Ms} = \frac{3}{4} n_{i\infty} v_{t\infty}^4, \tag{D.6}$$

$$\int d^3\mathbf{w} w_\parallel^2 w^4 f_{Ms} = \frac{35}{8} n_{i\infty} v_{t\infty}^6. \tag{D.7}$$

In addition we use

$$\int d^3\mathbf{w} w_\parallel^p \mathcal{T}(w) f_{Ms} = 0, \tag{D.8}$$

where p is an odd power and $\mathcal{T}(w)$ is an arbitrary function of w. Putting these together we find

$$\int d^3\mathbf{w} H_{1B} = n_1, \tag{D.9}$$

$$\int d^3\mathbf{w} w_\parallel H_{1B} = n_{i\infty} c_s \left(\frac{3\Delta}{2\epsilon} \frac{T_0}{T_{i\infty}} + \frac{u_1}{c_s} \right), \tag{D.10}$$

$$\int d^3\mathbf{w} w^2 H_{1B} = \frac{3}{2} n_{i\infty} v_{t\infty}^2 \left(-2 \frac{\Delta}{\epsilon} \frac{T_0}{T_{i\infty}} \frac{c_s^2}{v_{t\infty}^2} + \frac{T_1}{T_{i\infty}} + \frac{n_1}{n_{i\infty}} \right), \tag{D.11}$$

$$\int d^3\mathbf{w} w_\parallel^2 H_{1B} = \frac{3}{2} n_{i\infty} v_{t\infty}^2 \left(-2 \frac{\Delta}{\epsilon} \frac{T_0}{T_{i\infty}} \frac{c_s^2}{v_{t\infty}^2} + \frac{T_1}{3T_{i\infty}} + \frac{n_1}{3n_{i\infty}} \right), \tag{D.12}$$

$$\int d^3\mathbf{w} w_\parallel w^2 H_{1B} = \frac{5}{2} n_{i\infty} v_{t\infty}^2 c_s \left(\frac{5\Delta}{2\epsilon} \frac{T_0}{T_{i\infty}} + \frac{u_1}{c_s} \right) \tag{D.13}$$

For integrals over H_{1A} it is convenient to change variables from $w_\parallel, w_\perp$ to x, ξ, which are defined in 2. In terms of these variables

$$\frac{w_\parallel^2}{v_{t\infty}^2} = x\xi^2 = \frac{2}{3} x L_0^{(5/2)} P_2(\xi) + (\frac{1}{2} L_0^{(1/2)}(x) - \frac{1}{3} L_1^{(1/2)}(x)) P_0(\xi), \tag{D.14}$$

$$\frac{w^2 w_\parallel}{v_{t\infty}^3} = x^{3/2}\xi = x^{1/2} (\frac{5}{2} L_0^{(3/2)}(x) + L_1^{(3/2)}(x)) P_1(\xi). \tag{D.15}$$

Since we choose the first three moments of H_{1A} to be zero, the only non zero moments of H_{1A} are

$$\int d^3\mathbf{w} w_\parallel^2 H_{1A} = \frac{n_{i\infty} v_{t\infty}^2}{2} a_{0,2}, \tag{D.16}$$

$$\int d^3\mathbf{w} w^2 w_\parallel H_{1A} = -n_{i\infty} v_{t\infty}^3 \frac{5}{4} a_{1,1}. \tag{D.17}$$

Appendix E

Self-similar solutions for the distribution function near $x = 0$

E.1 Form of the collision operator at $v_\parallel \ll v_{ti}$

We can expand the Fokker-Planck collision operator given by (1.20) and (1.21) to get

$$C[f] = \frac{\gamma_{ii}}{m_i^2}\Big\{\nabla_v f \cdot \int d^3\mathbf{v}' f(\mathbf{v}')\nabla_v \cdot \big[\nabla_g \nabla_g g\big] + \int d^3\mathbf{v}' \nabla_g \nabla_g g f(\mathbf{v}') : \nabla_v \nabla_v f$$
$$-f\nabla_v \cdot \Big[\int d^3\mathbf{v}' \nabla_g \nabla_g g \cdot \nabla_{v'} f(\mathbf{v}')\Big] - \nabla_v f \cdot \int d^3\mathbf{v}' \nabla_g \nabla_g g \cdot \nabla_{v'} f(\mathbf{v}')\Big\}. \tag{E.1}$$

We can integrate the last term by parts in $\mathbf{v}'$ and then add it to the first term to get

$$\nabla_v f \cdot \int d^3\mathbf{v}' f(\mathbf{v}')\big(\nabla_v \cdot \big[\nabla_g \nabla_g g\big] + \nabla_{v'} \cdot \big[\nabla_g \nabla_g g\big]\big) = 0, \tag{E.2}$$

where we used the fact that the term in the parenthesis is zero identically by definition of $\mathbf{g} = \mathbf{v} - \mathbf{v}'$. The third term in equation (E.1), after integration by parts, gives an integral proportional to

$$\nabla_{v'} \cdot (\nabla_v \cdot \nabla_g \nabla_g g) = -\nabla_{v'} \cdot \frac{2\mathbf{g}}{g^3} = \nabla_g \cdot \frac{2\mathbf{g}}{g^3} = 8\pi\delta(\mathbf{g}). \tag{E.3}$$

Therefore the collision operator simplifies to

$$C[f] = \frac{\gamma_{ii}}{m_i^2}\int d^3\mathbf{v}' \nabla_g \nabla_g g f(\mathbf{v}') : \nabla_v \nabla_v f + 8\pi \frac{\gamma_{ii}}{m_i^2} f^2(\mathbf{v}). \tag{E.4}$$

For $v_\parallel \ll v_{ti} \sim v_\perp$ the dominant terms are those containing $\partial^2 f/\partial v_\parallel^2$. Therefore, to lowest order, we have

$$C[f] \simeq \frac{\gamma_{ii}}{m_i^2}\int d^3\mathbf{v}' \frac{g_\perp^2}{g^3} f(\mathbf{v}') \frac{\partial^2 f}{\partial {v_\parallel}^2} \equiv D_0(\mathbf{v}) \frac{\partial^2 f}{\partial {v_\parallel}^2}, \tag{E.5}$$

where we have implicitly defined the effective diffusion coefficient D_0, and $g_\perp^2 = g^2 - (\mathbf{g}\cdot\mathbf{b})^2$.

In normalised variables, defined in (2.54), the collision operator is $\bar{C}[\bar{f}, \bar{f}] = \bar{D}_0 \frac{\partial^2 \bar{f}}{\partial \bar{v}_\parallel^2}$, where $\bar{D}_0 \equiv D_0 m_i^2 v_{t\infty}/n_{i\infty}\gamma_{ii}$.

E.2 Solution for $\beta > 2/3$

Rewriting equation (3.12) in terms of $z \equiv \eta^3/9$ gives

$$zF'' + \left(\frac{2}{3} - z\right)F' + \Omega F = 0, \tag{E.6}$$

where the derivatives are now with respect to z.

Solutions to equation (E.6) are known as confluent hypergeometric functions $M(a, b, c)$, giving the general solution to the equation

$$F(z) = \bar{Q} z^{1/3} M(1/3 - \Omega; 4/3; z) + \bar{R} M(-\Omega; 2/3; z). \tag{E.7}$$

We determine the relationship between constants $\bar{Q}$ and $\bar{R}$, as well as the value of Ω using the boundary conditions.

First we require $F(z \to \infty)$ to not diverge exponentially. To lowest order, expansion of $M(a, b, c)$ for large $z > 0$ is given in [51] to be

$$M(a, b, z) \approx \frac{\Gamma[b]}{\Gamma[a]} e^z z^{a-b}. \tag{E.8}$$

This is an exponentially growing solution, which does not satisfy the boundary condition. Plugging this expansion into our solution (E.7) and requiring for the exponential term e^z to be zero gives

$$\bar{Q} = -\frac{\Gamma[2/3]\Gamma[1/3 - \Omega]}{\Gamma[-\Omega]\Gamma[4/3]} \bar{R}. \tag{E.9}$$

Then we use the boundary condition at $z \to -\infty$, which requires the function to decay to zero exponentially fast. Expansion in $z \to -\infty$ for the function M to lowest order ([51]) is

$$M(a, b, z) = \frac{\Gamma[b]}{\Gamma[b - a]} (-z)^{-a}. \tag{E.10}$$

We want the function to decay to zero exponentially fast, therefore this term has to disappear as $z \to -\infty$, which fixes the constant to be

$$\bar{Q} = \frac{\Gamma[2/3]\Gamma[1 + \Omega]}{\Gamma[2/3 + \Omega]\Gamma[4/3]} \bar{R} \tag{E.11}$$

Instead of being a set of equations to determine $\bar{Q}$ and $\bar{R}$, equations (E.9) and (E.11) allow us to determine Ω. Comparing solutions (E.9) and (E.11), we find that they can only be satisfied simultaneously if

$$\frac{\Gamma[-\Omega]\Gamma[1+\Omega]}{\Gamma[2/3+\Omega]\Gamma[1/3-\Omega]}+1=0. \tag{E.12}$$

We then choose $\Omega = 1/6+N$, where $N > -1/6$ and N is, in principle, real. Using Euler's reflection formula $\Gamma[x]\Gamma[1-x] = \pi/\sin(\pi x)$, the equation simplifies to

$$\frac{\sin(\pi/6-\pi N)}{\sin(-\pi/6-\pi N)}=-1. \tag{E.13}$$

From trigonometric relationships, it follows that this equation is only satisfied for an integer N.

Putting the terms together and reintroducing η we now have

$$\begin{aligned} F(\eta) = \bar{R}\Big(&K\eta M(1/6-N;4/3;\eta^3/9) \\ &+ M(-1/6-N;2/3;\eta^3/9)\Big), \end{aligned} \tag{E.14}$$

where $K \equiv -3^{-1/6}\frac{2\pi}{\Gamma[1/3]^2}\frac{\Gamma[-N+1/6]}{\Gamma[-N-1/6]}$ and we used $\frac{\Gamma[2/3]}{\Gamma[4/3]} = \frac{2\sqrt{3}\pi}{\Gamma[1/3]^2}$.

To prove that $N = 0$ is the only solution we use the condition $F > 0$. First, $F(\eta = 0) = \bar{R}$, thus $\bar{R} > 0$. The solution (E.14) can be written as $F = \bar{R}KF_A + \bar{R}F_B$, where $F_A \equiv \eta M(1/6-N;2/3,\eta^3/3)$ and $F_B \equiv M(-1/6-N;4/3,\eta^3/3)$. At small $\eta > 0$ they are both positive since $F_A \approx \eta + O(\eta^4)$ and $F_B \approx 1 + O(\eta^3)$.

We now prove that for $N > 0$ there exists a region where both $F_A < 0$ and $F_B < 0$ implying $F < 0$, which does not satisfy the positivity constraint $F > 0$. From [51], if the root exists, the approximate values of the r^{th} root of the confluent hypergeometric function $M(a;b;z)$ is

$$\eta_r \approx \pi^2\frac{(r+b/2-3/4)^2}{2b-4a}+O((2b-4a)(b/2-a)^{-2}) \tag{E.15}$$

This means that F_A and F_B have zeros at

$$\eta_r^A \approx \pi^2\frac{(r-1/12)^2}{2+4N}+O((2+4N)(N+1/2)^{-2}) \tag{E.16}$$

$$\eta_r^B \approx \pi^2\frac{(r-5/12)^2}{2+4N}+O((2+4N)(N+1/2)^{-2}). \tag{E.17}$$

Since the functions F_A and F_B are both positive at small η, they will be negative at $\eta_1 < \eta < \eta_2$, where η_r is the r^{th} root of the function. F_A has its first root at $\eta_1^A \approx 0.42/(1+2N)$,

the first two roots of F_B are at $\eta_1^B \approx 0.17/(1+2N) < \eta_1^A$ and $\eta_2^B \approx 1.25/(1+2N) > \eta_1^A$. Therefore, there always exists a region at $\eta > \eta_1^A$, where both functions are negative, if these roots exist. The plots of the functions for $N = 0, 1, 2, 3$ are shown in Figure E.1. Note that the accuracy of the approximations (E.16) and (E.17) improve with larger N. However, even for $N = 1$ the roots are separated enough for the argument to hold using the approximate values.

The approximations in (E.16) and (E.17) are only true if the roots exists. For the case of $N = 0$, F_A has no roots (as we can see from the Figure E.1) and therefore we cannot use the argument above to argue that $F < 0$ at $N = 0$. In this case $KF_A > -F_B$, as can be seen from using expansion (E.8) for F_A and F_B (or from the Figure E.1). This ensures positivity of the full function F. Therefore we have shown that the only solution that satisfies the boundary conditions has $N = 0$ and so $\Omega = 1/6$. The final solution is

$$F(\eta) = \bar{R}\Big(- 12^{1/3}\sqrt{\pi}\frac{1}{\Gamma[-1/6]}\eta M(1/6; 4/3; \eta^3/9) + M(-1/6; 2/3; \eta^3/9)\Big). \tag{E.18}$$

Taking the limit $\eta \to \infty$, and using expansion from [51]

$$M(a, b, z)/\Gamma[b] \simeq \frac{e^{i\pi a} z^{-a}}{\Gamma[b-a]}\Big(1 + a(1+a-b)(-z)^{-1} + O(z^{-2})\Big) \tag{E.19}$$

we get, to lowest order,

$$F(\eta \to \infty) \simeq -2 \times 3^{7/6}\frac{\Gamma[2/3]}{\Gamma[-1/6]}\bar{R}\sqrt{\eta} \approx 1.44\bar{R}\sqrt{\eta}. \tag{E.20}$$

We can expand the function to next order to show that

$$F(\eta) - F(\eta \to \infty) \simeq 0.36\bar{R}\eta^{-5/2} > 0. \tag{E.21}$$

This result is used in Section 3.1.2 to prove that the integrand of $F(\eta) - F(\eta \to \infty)$ is always positive.

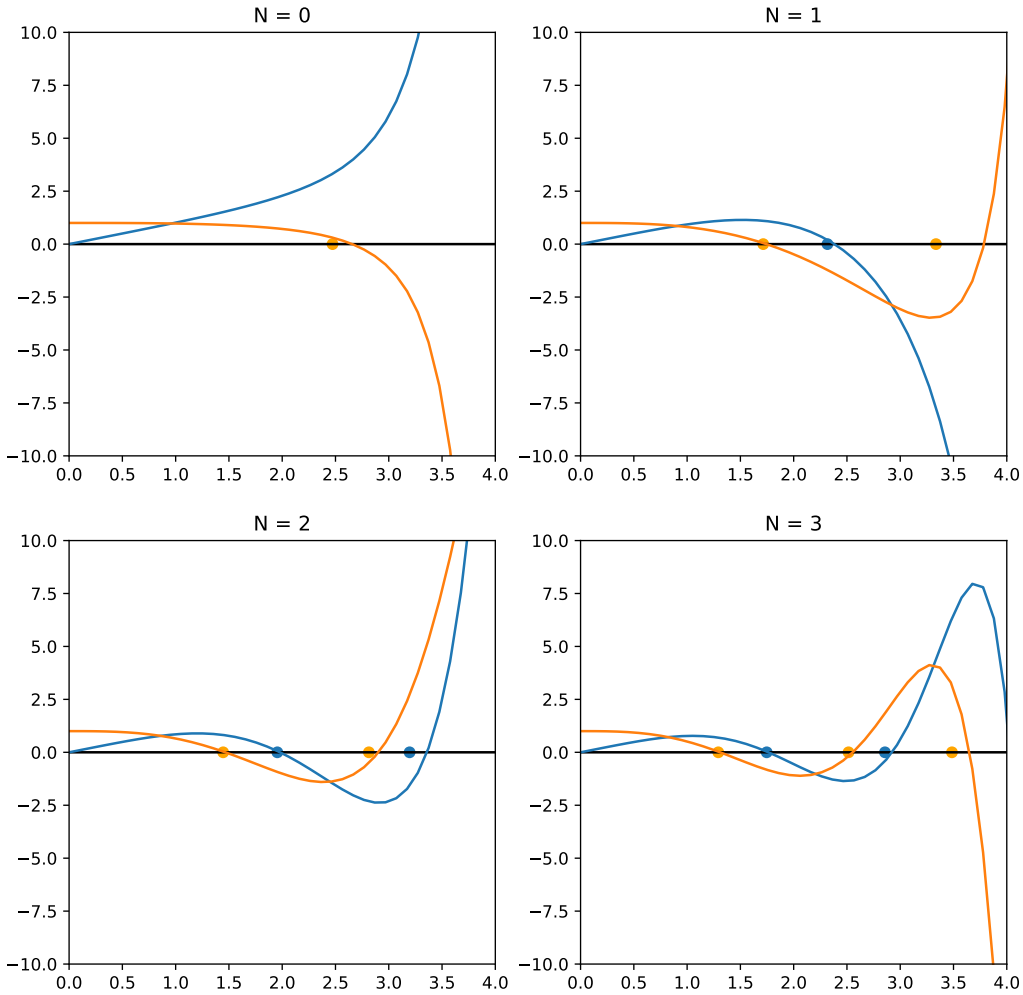

Figure E.1: Functions KF_A (blue line) and F_B (orange line), with η on the horizontal axis. For $N \geq 1$ there exists a region between the first root of F_A and the second root of F_B where both functions, and thus F, are negative. The points are the approximations of the roots using (E.16) and (E.17). Crucially, F_A does not have a root for $N = 0$.

Appendix F

Finding the Maxwellian for the numerical collisional operator

We are looking for $f_{Num} = \sum_{ij} a_{ij}\psi_{ij}$ such that the numerical collision operator defined in (4.26) is zero and that the moments of f_{Num} evaluate to the boundary condition values of particle density n_∞, mean flow $u_{\parallel\infty}$ and thermal velocity $v_{t\infty}$. This gives $N_\perp N_\parallel + 3$ equations and only $N_\perp N_\parallel$ unknowns. We introduce three additional variables λ_p, where $p = 1, 2, 3$, and solve the system of equations given by

$$\frac{F_{kl}[f_{Num}]}{N_{kl}} \equiv \frac{C_{kl}[f_{Num}] - \sum_p \lambda_p T_{pkl}}{N_{kl}} = 0, \tag{F.1}$$

$$M_1 \equiv \int d^3\mathbf{v} f_{Num} - n_\infty = 0, \tag{F.2}$$

$$M_2 \equiv \int d^3\mathbf{v} v_\parallel f_{Num} - n_\infty u_{\parallel\infty} = 0, \tag{F.3}$$

$$M_3 \equiv \int d^3\mathbf{v}((v_\parallel - u_{\parallel\infty})^2 + v_\perp^2) f_{Num} - \frac{3}{2} n_\infty v_{t\infty}^2 = 0. \tag{F.4}$$

The factor N_{kl} is the normalisation defined in (4.50). The normalisation is included because numerically, we will be solving equation (F.1) up to some finite precision ϵ only.

In theory, we can choose the three tensors T_{pkl} to be projections of any independent functions of velocity on the ψ_{ij} basis. We choose to use such T_{pkl} that the non-exact particle, momentum and energy flux conservation is countered by the introduction of these terms as sources in the equation. Galerkin's finite element method with quadratic basis ensures the conservation of these moments to numerical precision and therefore, for this implementation of the operator, we expect λ_p to be small (for perfect conservation

they would be zero). The tensors T_{pkl} are defined to be

$$T_{1kl} = \int d^3\mathbf{v}\psi_{kl} f_{Num}, \tag{F.5}$$

$$T_{2kl} = \int d^3\mathbf{v}\psi_{kl} \frac{\partial f_{Num}}{\partial v_\parallel}, \tag{F.6}$$

$$T_{3kl} = \int d^3\mathbf{v}\psi_{kl} \left(\frac{\partial}{\partial v_\parallel}\big(v_\parallel f_{Num}\big) + \frac{1}{v_\perp}\frac{\partial}{\partial v_\perp}\big(v_\perp^2 f_{Num}\big) \right). \tag{F.7}$$

We also introduce tensors D_{iklmn}, which are defined by replacing f_{Num} by ψ_{mn} in the expressions (F.5)–(F.6). They will be useful later when deriving the Jacobian because $\partial T_{ikl}/\partial a_{mn} = D_{ijklmn}$.

To define derivatives of equations M_i, it is also useful to introduce the tensors

$$A_{klmn} \equiv \int d^3\mathbf{v}\psi_{kl}\psi_{mn}, \tag{F.8}$$

$$A_{kl} \equiv \sum_{mn} A_{klmn} = \int d^3\mathbf{v}\psi_{kl}. \tag{F.9}$$

Then we can rewrite (F.2)–(F.4) as

$$M_1 = \sum_{kl} a_{kl}A_{kl} - n_\infty, \tag{F.10}$$

$$M_2 = \sum_{kl} a_{kl}v_{\parallel l}A_{kl} - n_\infty u_{\parallel\infty}, \tag{F.11}$$

$$M_3 = \sum_{kl} a_{kl}((v_{\parallel l} - u_{\parallel\infty})^2 + v_{\perp k}^2)A_{kl} - \frac{3}{2}n_\infty v_{t\infty}^2. \tag{F.12}$$

and $\partial M_i/\partial a_{mn}$ are equal to

$$\frac{\partial M_1}{\partial a_{ij}} = A_{ij}, \tag{F.13}$$

$$\frac{\partial M_2}{\partial a_{ij}} = v_{\parallel j}A_{ij}, \tag{F.14}$$

$$\frac{\partial M_3}{\partial a_{ij}} = ((v_{\parallel j} - u_{\parallel\infty})^2 + v_{\perp i}^2)A_{ij}. \tag{F.15}$$

To solve the equations numerically, we make an initial guess of $a_{ij}^{(0)}$, for $i = 1, ..., N_\perp$ and $j = 1, ..., N_\parallel$ and $\lambda_p^{(0)}$, for $p = 1, 2, 3$. We choose $a_{ij}^{(0)} = \frac{1}{\pi^{3/2}}\exp\big(-(v_{\parallel i} - u_{\infty\parallel})^2 - v_{\perp j}^2\big)$ and $\lambda_p^{(0)} = 0$. To simplify notation we turn 2 dimensional arrays into 1 dimensional ones and denote the reshaped arrays with a tilde. We introduce a variable $\tilde{a}_\mu$ where $\mu = 1, 2, ..., N_\perp N_\parallel + 3$ and

$$\tilde{a}_\mu = \begin{cases} a_{ij}, & \text{for } \mu = N_\parallel i + j \le N_\perp N_\parallel, \\ \lambda_{\mu+1-N_\perp N_\parallel}, & \text{for } \mu > N_\perp N_\parallel. \end{cases} \tag{F.16}$$

We also combine equations (F.1) and (F.2)–(F.4) into $\tilde{F}_\mu = 0$

$$\tilde{F}_\mu = \begin{cases} F_{ij}, & \text{for } \mu = N_\parallel i + j \leq N_\perp N_\parallel, \\ M_{\mu+1-N_\perp N_\parallel}, & \text{for } \mu > N_\perp N_\parallel. \end{cases} \tag{F.17}$$

The same way we change C_{kl} to $\tilde{C}_\mu$, T_{ikl} to $\tilde{T}_{i\mu}$ and D_{iklmn} to $\tilde{D}_{i\mu\nu}$. To use Newton's method, we find the Jacobian

$$\frac{\partial \tilde{F}_\mu}{\partial \tilde{a}_\nu} = \left(\begin{array}{c|c} \frac{\partial \tilde{C}_\mu}{\partial \tilde{a}_\nu} - \sum_i \lambda_i \tilde{D}_{i\mu\nu} & -\tilde{T}_{\nu+1-N_\perp N_\parallel,\mu} \\ \hline \frac{\partial \tilde{M}_{\mu+1-N_\perp N_\parallel}}{\partial \tilde{a}_\nu} & \mathbf{0} \end{array} \right). \tag{F.18}$$

The last block is zero because the moments M_i are independent of λ_i.

Given an iteration n in our Newton's method $\tilde{a}_\mu^{(n)}$, we evaluate $\tilde{F}_\mu\big(\tilde{a}_\mu^{(n)}\big)$ and the derivative $\partial \tilde{F}_\mu / \partial \tilde{a}_\nu \big(\tilde{a}_\mu^{(n)}\big)$ and then we use them to find a better approximation by solving the equation

$$\sum_\nu \frac{\partial \tilde{F}_\mu^{(n)}}{\partial \tilde{a}_\nu} \big(\tilde{a}_\nu^{(n+1)} - \tilde{a}_\nu^{(n)}\big) = \tilde{F}_\mu^{(n)}, \tag{F.19}$$

where superscript n indicates that the functions are evaluated with $\tilde{a}_\mu^{(n)}$.

We iterate until we reach our desired precision ϵ by satisfying

$$\sqrt{\sum_\mu \big(\tilde{F}_\mu^{(n)}\big)^2} \leq \epsilon, \tag{F.20}$$

$$\sqrt{\sum_\mu \left|(a_\mu^{(n+1)} - a_\mu^{(n)})/a_\mu^{(n)}\right|^2} \leq \epsilon, \tag{F.21}$$

where in the second condition we only include the terms of the summation that satisfy $\left|a_\mu^{(n)}\right| > 10^{-14}$ to avoid lack of convergence due to machine precision errors. We choose $\epsilon = 10^{-8}$. We recover values of λ_i to be zero almost to machine precision, $\lambda_i \sim 10^{-14}$. This indicates that our collision operator is satisfying the conservation laws to machine precision, as expected.

Appendix G

Calculating the errors in the numerical Chodura condition

We expand (5.9) to second order in $\Delta\phi_0/T_e$

$$n(x = x_1) - n(x = 0) = n(0)\frac{\Delta\phi_0}{T_e}\left(1 + \frac{\Delta\phi_0}{2T_e} + ...\right). \tag{G.1}$$

We write density in terms of the distribution function and introduce the velocity $v_c \equiv \sqrt{2\Delta\phi_0}$ to split the integral into two regions

$$n(x = 0) = \int_{0\leq v_\parallel \leq v_c} d^3\boldsymbol{v} f_{MPE} + \int_{v_c \leq v_\parallel \leq V_{max}} d^3\boldsymbol{v} f_{MPE}, \tag{G.2}$$

where V_{max} is the largest value of $v_\parallel$ in the grid. In equations (4.5) and (4.6), we defined ξ, the position in x space associated with the characteristic at the previous time step, and ζ, the parallel velocity at the previous time step and location ξ. Using these variables, the characteristics that reach the MPE with $v_\parallel < v_c$ come from the MPE and have $\zeta = -v_\parallel$, where $f = 0$ due to the boundary condition, whereas the characteristics that reach the MPE with $v_\parallel > v_c$ come from $\xi = x_1$ and $\zeta = v_\parallel\sqrt{1 - v_c^2/v_\parallel^2}$. Using equation (5.8) for position $x = x_0$ and $v_\parallel > v_c$ gives

$$f_{MPE}(v_\parallel > v_c) - f(x_1, \zeta) = C[f_{MPE}]\Delta t(0, v_\parallel > v_c) + \delta_N f_0 \Delta t(0, v_\parallel > v_c). \tag{G.3}$$

The time step is given by (4.13) and for these trajectories is

$$\Delta t(0, v_\parallel > v_c) = \frac{x_1}{\Delta\phi_0^2}\frac{v_\parallel^3}{3}\left[2 + \left(1 - \frac{v_c^2}{v_\parallel^2}\right)^{3/2} - 3\left(1 - \frac{v_c^2}{v_\parallel^2}\right)^{1/2}\right]. \tag{G.4}$$

The density at x_1 is split into regions of negative and positive $v_\parallel$

$$n(x_1) = \int_{v_\parallel < 0} d^3\boldsymbol{v} f(x_1, v_\parallel) + \int_{0\leq v_\parallel \leq V_{max}} d^3\boldsymbol{v} f(x_1, v_\parallel). \tag{G.5}$$

From (5.8) we find that the distribution function at x_1 and $v_\parallel < 0$ is given by

$$f(x_1, v_\parallel < 0) = C[f(x_1)]\Delta t(x_1, v_\parallel < 0) + \delta_N f_0 \Delta t(x_1, v_\parallel < 0), \tag{G.6}$$

where we have used the boundary condition $f_{MPE}(v_\parallel < 0) = 0$ again. From (4.13) the time step is

$$\Delta t(x_1, v_\parallel < 0) = \frac{x_1}{\Delta\phi_0^2}\frac{v_\parallel^3}{3}\left(2 + \left(1 + \frac{v_c^2}{v_\parallel^2}\right)^{3/2} - 3\left(1 + \frac{v_c^2}{v_\parallel^2}\right)^{1/2} + 3\left[1 - \left(1 + \frac{v_c^2}{v_\parallel^2}\right)^{1/2}\right]\frac{v_c^2}{v_\parallel^2}\right). \tag{G.7}$$

Focusing on the second integral in (G.5), we split the integration region into intervals $0 \le v_\parallel \le \sqrt{V_{max}^2 - v_c^2}$ and $\sqrt{V_{max}^2 - v_c^2} < v_\parallel < V_{max}$ and change integration variable in the interval $0 \le v_\parallel \le \sqrt{V_{max}^2 - v_c^2}$ to $\hat{v}_\parallel$, where $v_\parallel = \hat{v}_\parallel\sqrt{1 - v_c^2/\hat{v}_\parallel^2}$. We find

$$\int_{0\le v_\parallel \le V_{max}} d^3\boldsymbol{v} f(x_1, v_\parallel) = \int_{v_c \le \hat{v}_\parallel \le V_{max}} f\left(x_1, \hat{v}_\parallel\sqrt{1 - v_c^2/\hat{v}_\parallel^2}\right)\left(1 - \frac{v_c^2}{\hat{v}_\parallel^2}\right)^{-1/2} d\hat{v}_\parallel + \int_{\sqrt{V_{max}^2 - v_c^2} < v_\parallel < V_{max}} d^3\boldsymbol{v} f(x_1, v_\parallel). \tag{G.8}$$

If $V_{max} \gg v_c$, the second integral is approximately $f(x_1, V_{max}){v_c}^2/(2V_{max}) \ll 1$. Since the distribution function is small at large $v_\parallel$, this contribution to the density at x_1 can be neglected. These terms contribute only a $\sim 0.01\%$ discrepancy in the kinetic Chodura condition. Equation (G.3) then allows us to express the first integral in terms of f_{MPE}. We relabel the variables $\hat{v}_\parallel \to v_\parallel$ to get

$$n(x_1) = \int_{v_\parallel < 0} d^3\boldsymbol{v} f(x_1, v_\parallel) + \int_{v_c \le v_\parallel \le V_{max}} d^3\boldsymbol{v} f_{MPE}(v_\parallel)\left(1 - \frac{v_c^2}{v_\parallel^2}\right)^{-1/2} - \int_{v_c \le v_\parallel \le V_{max}} d^3\boldsymbol{v}(C[f_{MPE}(v_\parallel)] + \delta_N f_0)\Delta t(0, v_\parallel > v_c)\left(1 - \frac{v_c^2}{v_\parallel^2}\right)^{-1/2} + \mathcal{E}_A, \tag{G.9}$$

where $\mathcal{E}_A$ includes the error $\mathcal{E}_v$ associated with the velocity space discretisation as well as any errors due to numerical integration of velocity integrals in (G.9). The error $\mathcal{E}_A$ can be calculated by finding the density of ions at x_1 by integrating the distribution function as in (G.5) and subtracting from it all the numerically integrated right hand side terms of (G.9).

Putting equations (G.1), (G.2), (G.3) and (G.9) together gives

$$n(0)\frac{\Delta\phi_0}{T_e}\left(1+\frac{\Delta\phi_0}{2T_e}\right)=\int_{v_\parallel<0}d^3\boldsymbol{v}f(x_1,v_\parallel)+\int_{v_c\le v_\parallel\le V_{max}}d^3\boldsymbol{v}f_{MPE}(v_\parallel)\left(1-\frac{v_c^2}{v_\parallel^2}\right)^{-1/2}$$
$$-\int_{v_c\le v_\parallel\le V_{max}}d^3\boldsymbol{v}(C[f_{MPE}(v_\parallel)]+\delta_N f_0)\Delta t(0,v_\parallel>v_c)\left(1-\frac{v_c^2}{v_\parallel^2}\right)^{-1/2}$$
$$-\int_{0\le v_\parallel\le V_{max}}d^3\boldsymbol{v}f_{MPE}+\mathcal{E}_A. \tag{G.10}$$

The integral that contains $\delta_N f_0$ has a logarithmic divergence for $V_{max}\to\infty$. To see this, we expand $\Delta t(0,v_\parallel>v_c)\big(1-\frac{v_c^2}{v_\parallel^2}\big)^{-1/2}$ to lowest order in $v_\parallel/v_c\gg 1$ to get that

$$\Delta t(0,v_\parallel>v_c)\left(1-\frac{v_c^2}{v_\parallel^2}\right)^{-1/2}\simeq\frac{x_1}{v_\parallel}. \tag{G.11}$$

Integrating it gives a term that goes as $\sim\ln(V_{max}/v_c)$. The contribution from this error is $\sim 1\%$ in our runs and we will neglect it for the rest of the analysis.

Since the distribution function at the MPE is close to zero at $v_\parallel\sim v_c$ and v_c is smaller than V_{max}, we can expand the first integral on the right hand side of (G.10) and get

$$\int_{v_c\le v_\parallel\le V_{max}}d^3\boldsymbol{v}f_{MPE}(v_\parallel)\left(1-\frac{v_c^2}{v_\parallel^2}\right)^{-1/2}\simeq\int_{v_c\le v_\parallel\le V_{max}}d^3\boldsymbol{v}f_{MPE}(v_\parallel)$$
$$+\int_{v_c\le v_\parallel\le V_{max}}d^3\boldsymbol{v}f_{MPE}(v_\parallel)\frac{v_c^2}{2v_\parallel^2}+\int_{v_c\le v_\parallel\le V_{max}}d^3\boldsymbol{v}f_{MPE}(v_\parallel)\frac{3v_c^4}{8v_\parallel^4}+..., \tag{G.12}$$

where we have not written higher order terms explicitly. However, the higher order terms decay very slowly. As a result, we keep all of them by computing the integral on the left hand side of (G.12) numerically and introducing $\mathcal{E}_B$, which is defined in (5.11).

Plugging (G.12) into (G.10), expressing v_c in terms of $\Delta\phi_0$ and only keeping the largest errors gives (5.10).

References

[1] Alessandro Geraldini, Robert J. Ewart, Stephan Brunner, and Felix I. Parra. Characteristics of monotonic sheaths near a wall with grazing magnetic incidence, 2025.

[2] J D Lawson. Some criteria for a power producing thermonuclear reactor. *Proceedings of the Physical Society. Section B*, 70(1):6, 1957.

[3] Samuel E. Wurzel and Scott C. Hsu. Progress toward fusion energy breakeven and gain as measured against the Lawson criterion. *Physics of Plasmas*, 29(6):062103, 2022.

[4] V.S. Mukhovatov and V.D. Shafranov. Plasma equilibrium in a tokamak. *Nuclear Fusion*, 11(6):605, 1971.

[5] Jr. Spitzer, Lyman. The Stellarator Concept. *Physics of Fluids*, 1(4):253–264, July 1958.

[6] H.A.B. Bodin. The reversed field pinch. *Nuclear Fusion*, 30(9):1717, 1990.

[7] R.F. Post. The magnetic mirror approach to fusion. *Nuclear Fusion*, 27(10):1579, 1987.

[8] ITER Physics Expert Group on Disruptions, Plasma Control, MHD, and ITER Physics Basis Editors. Chapter 3: Mhd stability, operational limits and disruptions. *Nuclear Fusion*, 39(12):2251, 1999.

[9] C S Pitcher and P C Stangeby. Experimental divertor physics. *Plasma Physics and Controlled Fusion*, 39(6):779, 1997.

[10] H Bolt, V Barabash, G Federici, J Linke, A Loarte, J Roth, and K Sato. Plasma facing and high heat flux materials – needs for iter and beyond. *Journal of Nuclear Materials*, 307-311:43–52, 2002.

[11] J. Bohdansky. Important sputtering yield data for tokamaks: A comparison of measurements and estimates. *Journal of Nuclear Materials*, 93-94:44–60, 1980.

[12] F Militello and W Fundamenski. Multi-machine comparison of drift fluid dimensionless parameters. *Plasma Physics and Controlled Fusion*, 53(9):095002, 2011.

[13] R D Hazeltine. Recursive derivation of drift-kinetic equation. *Plasma Physics*, 15(1):77, 1973.

[14] P J Catto. Linearized gyro-kinetics. *Plasma Physics*, 20(7):719, 1978.

[15] E. A. Frieman and Liu Chen. Nonlinear gyrokinetic equations for low-frequency electromagnetic waves in general plasma equilibria. *The Physics of Fluids*, 25(3):502–508, 03 1982.

[16] Felix I Parra and Peter J Catto. Limitations of gyrokinetics on transport time scales. *Plasma Physics and Controlled Fusion*, 50(6):065014, 2008.

[17] E. L. Shi, G. W. Hammett, T. Stoltzfus-Dueck, and A. Hakim. Gyrokinetic continuum simulation of turbulence in a straight open-field-line plasma. *Journal of Plasma Physics*, 83(3):905830304, 2017.

[18] M. A. Dorf, R. H. Cohen, M. Dorr, T. Rognlien, J. Hittinger, J. Compton, P. Colella, D. Martin, and P. McCorquodale. Simulation of neoclassical transport with the continuum gyrokinetic code COGENT. *Physics of Plasmas*, 20(1):012513, 2013.

[19] Dominik Michels, Andreas Stegmeir, Philipp Ulbl, Denis Jarema, and Frank Jenko. Gene-x: A full-f gyrokinetic turbulence code based on the flux-coordinate independent approach. *Computer Physics Communications*, 264:107986, 2021.

[20] C. S. Chang and S. Ku. Spontaneous rotation sources in a quiescent tokamak edge plasma. *Physics of Plasmas*, 15(6):062510, 2008.

[21] X.Q. Xu, Z. Xiong, M.R. Dorr, J.A. Hittinger, K. Bodi, J. Candy, B.I. Cohen, R.H. Cohen, P. Colella, G.D. Kerbel, S. Krasheninnikov, W.M. Nevins, H. Qin, T.D. Rognlien, P.B. Snyder, and M.V. Umansky. Edge gyrokinetic theory and continuum simulations. *Nuclear Fusion*, 47(8):809, 2007.

[22] S. I. Braginskii. Transport Processes in a Plasma. *Reviews of Plasma Physics*, 1:205, 1965.

[23] P Ricci, F D Halpern, S Jolliet, J Loizu, A Mosetto, A Fasoli, I Furno, and C Theiler. Simulation of plasma turbulence in scrape-off layer conditions: the gbs code, simulation results and code validation. *Plasma Physics and Controlled Fusion*, 54(12):124047, 2012.

[24] Patrick Tamain, Hugo Bufferand, Guido Ciraolo, Clothilde Colin, Davide Galassi, Ph Ghendrih, Frédéric Schwander, and Eric Serre. The tokam3x code for edge turbulence fluid simulations of tokamak plasmas in versatile magnetic geometries. *Journal of Computational Physics*, 321:606–623, 2016.

[25] B D Dudson and J Leddy. Hermes: global plasma edge fluid turbulence simulations. *Plasma Physics and Controlled Fusion*, 59(5):054010, 2017.

[26] Andreas Stegmeir, David Coster, Alexander Ross, Omar Maj, Karl Lackner, and Emanuele Poli. Grillix: a 3d turbulence code based on the flux-coordinate independent approach. *Plasma Physics and Controlled Fusion*, 60(3):035005, 2018.

[27] Peter C Stangeby et al. *The plasma boundary of magnetic fusion devices*, volume 224. Institute of Physics Pub. Philadelphia, Pennsylvania, 2000.

[28] P. Helander, S. I. Krasheninnikov, and P. J. Catto. Fluid equations for a partially ionized plasma. *Physics of Plasmas*, 1(10):3174–3180, 1994.

[29] A. Zeiler, J. F. Drake, and B. Rogers. Nonlinear reduced Braginskii equations with ion thermal dynamics in toroidal plasma. *Physics of Plasmas*, 4(6):2134–2138, 1997.

[30] M. Giacomin, P. Ricci, A. Coroado, G. Fourestey, D. Galassi, E. Lanti, D. Mancini, N. Richart, L.N. Stenger, and N. Varini. The gbs code for the self-consistent simulation of plasma turbulence and kinetic neutral dynamics in the tokamak boundary. *Journal of Computational Physics*, 463:111294, 2022.

[31] D.S. Oliveira, T. Body, D. Galassi, C. Theiler, E. Laribi, P. Tamain, A. Stegmeir, M. Giacomin, W. Zholobenko, P. Ricci, H. Bufferand, J.A. Boedo, G. Ciraolo, C. Colandrea, D. Coster, H. de Oliveira, G. Fourestey, S. Gorno, F. Imbeaux,

F. Jenko, V. Naulin, N. Offeddu, H. Reimerdes, E. Serre, C.K. Tsui, N. Varini, N. Vianello, M. Wiesenberger, C. Wüthrich, and the TCV Team. Validation of edge turbulence codes against the tcv-x21 diverted l-mode reference case. *Nuclear Fusion*, 62(9):096001, 2022.

[32] Robert J Ewart, Felix I Parra, and Alessandro Geraldini. Sheath collapse at critical shallow angle due to kinetic effects. *Plasma Physics and Controlled Fusion*, 64(1):015010, 2021.

[33] A Geraldini, F I Parra, and F Militello. Solution to a collisionless shallow-angle magnetic presheath with kinetic ions. *Plasma Physics and Controlled Fusion*, 60(12):125002, 2018.

[34] D Tskhakaya. One-dimensional plasma sheath model in front of the divertor plates. *Plasma Physics and Controlled Fusion*, 59(11):114001, 2017.

[35] Lewi Tonks and Irving Langmuir. Oscillations in ionized gases. *Phys. Rev.*, 33:195–210, 1929.

[36] David Bohm. The characteristics of electrical discharges in magnetic fields. *Qualitative Description of the Arc Plasma in a Magnetic Field*, 1949.

[37] A Geraldini, S Brunner, and F I Parra. Sheath constraints on turbulent magnetised plasmas. *Plasma Physics and Controlled Fusion*, 66(10):105021, sep 2024.

[38] R Chodura. Plasma–wall transition in an oblique magnetic field. *The Physics of Fluids*, 25(9):1628–1633, 1982.

[39] H. A. Claaßen and H. Gerhauser. Generalized bohm's criterion for thermal ions in oblique magnetic and electric fields. *Contributions to Plasma Physics*, 36(2-3):361–365, 1996.

[40] K U Riemann. The bohm criterion and sheath formation. *Journal of Physics D: Applied Physics*, 24(4):493, 1991.

[41] K.-U. Riemann. Kinetic theory of the plasma sheath transition in a weakly ionized plasma. *The Physics of Fluids*, 24(12):2163–2172, 1981.

[42] E R Harrison and W B Thompson. The low pressure plane symmetric discharge. *Proceedings of the Physical Society*, 74(2):145, 1959.

[43] D. Carralero, P. Manz, L. Aho-Mantila, G. Birkenmeier, M. Brix, M. Groth, H. W. Müller, U. Stroth, N. Vianello, and E. Wolfrum. Experimental validation of a filament transport model in turbulent magnetized plasmas. *Phys. Rev. Lett.*, 115:215002, 2015.

[44] David Kahaner, Cleve B. Moler, and Stephen Nash. *Numerical Methods and Software*. Prentice-Hall series in computational mathematics. Prentice Hall, illustrated edition, 1988.

[45] E. Hirvijoki and M. F. Adams. Conservative discretization of the Landau collision integral. *Physics of Plasmas*, 24(3):032121, 2017.

[46] Eero Hirvijoki. Conservative finite-element method for the relativistic coulomb collision operator, 2019.

[47] W. Eckstein, C. Garciá-Rosales, J. Roth, and J. László. Threshold energy for sputtering and its dependence on angle of incidence. *Nuclear Instruments and Methods in Physics Research Section B: Beam Interactions with Materials and Atoms*, 83(1):95–109, 1993.

[48] A. Geraldini, R. J. Ewart, F. I. Parra, and S. Brunner. Can a monotonic electrostatic potential exist in a debye sheath at a sufficiently shallow magnetic field angle? In *Proceedings of the 48th European Physical Society Conference on Plasma Physics, EPS 2022*, 2022. 48th European Physical Society Conference on Plasma Physics, EPS 2022 ; Conference date: 27-06-2022 Through 01-07-2022.

[49] R.D. Hazeltine, M.D. Calvin, P.M. Valanju, and E.R. Solano. Analytical calculation of neutral transport and its effect on ions. *Nuclear Fusion*, 32(1):3, 1992.

[50] T. Fülöp, Peter J. Catto, and P. Helander. Effect of neutral atoms on tokamak edge plasmas. *Physics of Plasmas*, 8(12):5214–5220, 2001.

[51] Milton Abramowitz and Irene A. Stegun. *Handbook of Mathematical Functions with Formulas, Graphs, and Mathematical Tables*. Dover, New York, ninth dover printing, tenth gpo printing edition, 1964.